Johannes Gutenberg-Universität Mainz

Thermomechanical Modeling of Magmatic Systems

Dissertation
zur Erlangung des Grades
Doktor der Naturwissenschaften
im Promotionsfach Geologie/Paläonthologie

am Fachbereich Chemie, Pharmazie, Geographie und Geowissenschaften
der Johannes Gutenberg-Universität Mainz

Arne Spang
geboren in Kirchheimbolanden

Mainz, 2022

1. Berichterstatter: Prof. Dr. Boris J. P. Kaus

Tag der mündlichen Prüfung: 28.07.2022

Abstract

Magmatic systems and their volcanoes shape the lives of hundreds of millions of people around the globe. As these transcrustal systems cannot be directly observed, their structure and internal processes can only be inferred by modeling them and comparing the results to surface observations. Limited by computational cost, traditional models had to neglect structural complexity, magma buoyancy and realistic rheologies. This results in an inability to enhance the understanding of the large scale dynamics and evolution of magmatic systems. Estimating the onset, duration, magnitude or type of volcanic eruptions remains unfeasible.

This thesis introduces new numerical modeling approaches to magmatic system research to tackle the existing challenges and utilize the growing number of surface observations more effectively. That includes a new parameterization for complex three-dimensional (3D) shapes which facilitates treating the initial model geometry as a flexible input parameter. With this approach, uncertainties of constraints on the initial geometry of the geological setting can be taken into account and the sensitivity of different observations to the initial geometry can be tested.

By combining the new parameterization with a massively parallel thermomechanical model, gravity forward modeling, petrological modeling and a set of different surface observations, the large scale geodynamics of the Altiplano-Puna magma system in the central Andes are investigated. The study includes a complex-shaped partially molten zone (magma body), magma buoyancy and visco-elasto-plastic rheology as it is observed in real rocks. Average density, melt content and geometry of the magma body are constrained alongside the key material parameters that govern the dynamics of the system. While traditional models attribute surface uplift to intrusion, this model demonstrates that it can also be caused by buoyancy-driven material transport within the magma body.

The last part of the thesis investigates the effect of the presence of pre-exsolved volatiles on syn-eruptive subsidence. A scaling law is derived that predicts subsidence as a function of volatile density, volume and depth as well as crustal rigidity. Applying the derived scaling law to the 2015 eruption of the Chilean stratovolcano Calbuco shows that about 20% of the observed syn-eruptive subsidence can be attributed to the release of pre-exsolved volatiles.

This thesis tackles several of the existing challenges that are associated with numerical modeling of magmatic systems. Structural complexity is addressed by utilizing a new parameterization for 3D shapes and high resolution models. Considering realistic, nonlinear rheologies and using high resolution, 3D models is facilitated by high-performance computing and a massively parallel thermomechanical software. The often neglected buoyancy of magma and volatiles in particular is incorporated as a driving mechanisms for magma dynamics. Finally, a joint interpretation of different surface observables provides much improved constraints on non-unique, sub-surface structures and processes.

Kurzfassung

Magmatische Systeme und ihre Vulkane formen das Leben von hunderten Millionen Menschen auf dem gesamten Planeten. Da diese transkrustalen Systeme nicht direkt beobachtet werden können, müssen ihr Aufbau und ihre internen Prozesse durch den Vergleich von Modellresultaten und Oberflächenbeobachtungen abgeleitet werden. Aufgrund begrenzter Rechenleistung mussten traditionelle Modelle strukturelle Komplexität, Magmaauftrieb und realistische Rheologien vernachlässigen. Deswegen können diese Modelle nicht genutzt werden, um die großräumige Dynamik und Entwicklung magmatischer Systeme zu verstehen. Beginn, Dauer, Stärke und Art von Eruptionen lassen sich im Vorhinein nicht abschätzen.

Diese Dissertation wendet neue numerische Methoden auf magmatische Systeme an, um bestehende Herausforderungen anzugehen und die wachsende Menge an Oberflächenbeobachtungen effektiver nutzen zu können. Das beinhaltet eine neue Parametrisierung für komplexe drei-dimensionale (3D) Formen, was es ermöglicht die initiale Modellgeometrie als flexiblen Parameter zu behandeln. Mit diesem Ansatz können Unsicherheiten von Daten über die Geometrie des geologischen Rahmens in Betracht gezogen und die Sensitivität unterschiedlicher Beobachtungen gegenüber der Geometrie getestet werden.

Durch die Kombination der neuen Parametrisierung mit einem parallelisierbaren thermo-mechanischen Modell, Gravitationsmodellen, petrologischen Modellen und einer Reihe verschiedener Oberflächenbeobachtungen, wird die großräumige Dynamik des Altiplano-Puna Magmasystem in den zentralen Anden untersucht. Die Studie beinhaltet einen geometrisch komplexen Magmakörper, Magmaauftrieb und viskoelasto-plastische Rheologie. Mittlere Dichte, mittlerer Schmelzanteil und Geometrie des Magmakörpers, sowie entscheidende Materialparameter, welche das System lenken, werden bestimmt. Während traditionelle Modelle Oberflächenhebungen Intrusionen zuordnen, zeigt dieses Modell, dass sie auch Ergebnis von, durch Auftrieb versursachtem, Materialtransport im inneren des Magmakörpers sein können.

Der letzte Teil der Dissertation untersucht die Auswirkungen von entmischten Volatilen auf syn-eruptive Subsidenz. Aus den Resultaten wird eine Skalierung abgeleitet welche die Subsidenz als Funktion der Steifigkeit der Kruste sowie Dichte, Volumen und Tiefe der Volatile voraussagt. Anwendung der Skalierung auf die Eruption des chilenischen Stratovulkans Calbuco im Jahre 2015 zeigt, dass etwa 20% der beobachteten syn-eruptiven Subsidenz dem Entweichen der bereits entmischten Volatile zugeschrieben werden kann.

Diese Dissertation beschäftigt sich mit einigen der bestehenden Herausforderungen numerischer Modellierung magmatischer Systeme. Strukturelle Komplexität wird durch eine neue Parametrisierung für 3D Formen und hochaufgelöste Modelle abgedeckt. Realistische Rheologien und hochaufgelöste Modelle werden durch die Nutzung von Hochleistungscomputern und einer parallelen thermo-mechanischen Software ermöglicht. Der oft vernachlässigte Auftrieb von Magma und Volatilen ist als Triebkraft für Magmadynamik miteinbezogen. Eine gemeinsame Interpretation von verschiedenen Oberflächenbeobachtungen ermöglicht ein deutlich verbessertes Verständnis von Untergrundstrukturen und -prozessen.

Contents

List of Figures

List of Tables

List of Abbreviations

yr	years
Myr	million years (10^6 yr)
MPa	megapascal (10^6 Pa)
GPa	gigapascal (10^9 Pa)
2D	two-dimensional
3D	three-dimensional
mGal	milligal ($10^{-5}\,\mathrm{m\,s^{-2}}$)
InSAR	Interferometric Synthetic Aperture Radar

Chapter 1

Introduction

1.1 Motivation

More than 600 million people live within 100 km of a volcano that has had at least one documented significant eruption (Figure 1.1). This number almost doubles when all Holocene volcanoes are included (Freire et al., 2019). The 2010 eruption of Eyjafjallajökull demonstrated that even moderate eruptions can affect entire continents (Gíslason et al., 2011) with air traffic disrupting ash clouds. In January 2022, the eruption of Hunga Tonga–Hunga Ha'apai showed how eruptions can cause hazards across the entire Pacific ocean through tsunamis.

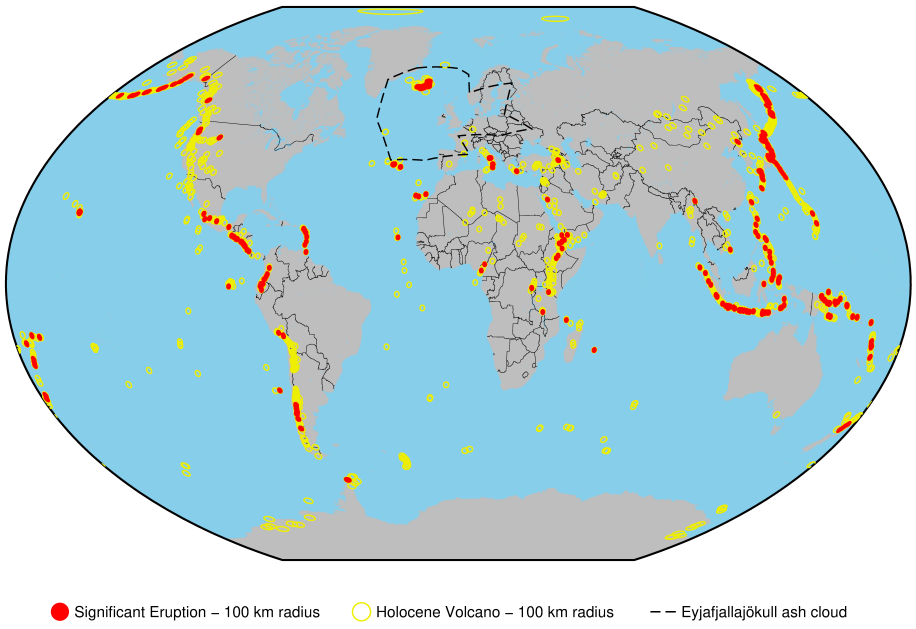

FIGURE 1.1: Global map of volcanoes and eruption locations. Red circles have 100 km radius and are centered on volcanoes that have had at least one documented significant eruption (NOAA, 2001). Empty yellow circles are centered on Holocene volcanoes without documented significant eruptions (NOAA, 2002). Note that circles along the edges of the map are distorted by the projection. Dashed black line shows the distribution of airborne ash caused by the 2010 Eyjafjallajökull eruption after Gudmundsson et al. (2012).

During the last decades, a combination of monitoring, pattern recognition and

experience from previous eruptions has provided the ability to forecast eruptions minutes or hours ahead of time (Segall, 2013) which is crucial for evacuation. But as this method is not based on an understanding of the mechanisms at work, its reliability and predictive power are limited. The duration, magnitude and type of activity cannot be estimated even after the eruption has started as demonstrated by the 2010 eruption of Eyjafjallajökull (e.g., Gudmundsson et al., 2012). Furthermore, as eruption frequency decreases with increasing eruption magnitude (Mason et al., 2004), there is a lack of experience in interpreting the precursory signals of large eruptions.

While a lot of individual processes that occur in magmatic systems before, during and after eruptions are relatively well understood, their precise interplay and the evolution of a magmatic system that can produce an eruption in the first place still elude our understanding. This is mainly due to the fact that we cannot directly observe the system that extends from the surface down into the lower crust or upper mantle during its evolution and eruption.

What we can observe, are the actual eruption, its products in gas, ash, lapilli, bombs and lava, the earthquakes that precede, accompany and follow it and the behavior of the volcano in its non-eruptive state. Expanding networks of ground-based measurements and a surge in satellite observations have facilitated extensive monitoring of active but non-eruptive volcanoes within the last few decades and provide time series of gas emissions and surface deformation. Seismic imaging, magnetotellurics and gravity anomalies are additional observations that can help constrain the distribution of anomalous bodies like fluids, melts and plutonic rocks below the surface.

It is therefore critical to develop methods that can relate observations made at the surface to processes at depth to gain a better understanding of how magmatic systems are distributed in the crust, how they evolve and how eruptions are initiated. One way to accomplish this is the development of numerical models that follow the laws of physics and include relevant mechanisms that occur in real systems. With their help, we can assume a set of initial conditions, model the evolution of the system and compare the modeling results to observations. If they agree, the assumed conditions may be a correct simplification of reality, if they disagree the assumed initial conditions are wrong and need to be modified. Finding the correct initial conditions through this process is known as inversion and allows us to infer something about processes that we cannot observe.

The better our models are, the more we can use them to test how different features of a magmatic system manifest themselves in surface observations, increasing our ability to monitor sub-surface processes and take a step towards a better understanding of magmatic systems.

It is the aim of this thesis to introduce new numerical modeling approaches into magmatic system research to improve the value of monitoring data. This includes developing a new parameterization for complex three-dimensional (3D) geometries and utilizing the 3D thermomechanical finite differences code LaMEM (Kaus et al., 2016). The main focus is on surface deformation patterns but seismic imaging, magnetotellurics, gravity anomalies, eruption products and gas emissions are also integrated as constraints on the initial conditions.

1.2 Structure of the thesis

This thesis is a cumulative project including three separate papers (chapters 2-4) accepted by and/or published in peer reviewed journals. As these chapters deal with

similar topics but are stand-alone papers, there is some overlap between the introductory and methodology sections. Section 1.7 outlines the author contributions to chapters 2-4.

Chapter 1: This chapter introduces the issues associated with monitoring and understanding trans-crustal magmatic systems and the aim of the thesis. It also provides an overview over existing approaches in the field of modeling magmatic systems and challenges that need to be overcome for a successful study. Furthermore the numerical code that is used throughout the thesis and the crucial material parameters are introduced.

Chapter 2: An early set of models showed that the geometry of the magma body has a big influence on the modeled surface velocities. So this chapter presents a new method to parameterize complex 3D volumes which facilitates treating the initial geometry of the model as a flexible input parameter. The method is applied to a salt daipir and a subduction zone to show its versatility and demonstrate that the initial geometry is an important factor in any mechanical model of geological settings. The study also includes examples of how the parameterization enables inverting for uncertain initial geometries with the help of geophysical observations.

Chapter 3: This study focuses on the Altiplano-Puna magma body (APMB) in the central Andes and its associated volcano Uturuncu which has been continuously uplifting for several decades. A joint interpretation of seismic imaging data, magnetotellurics surveys and gravity anomalies is used to constrain size, location, density and melt content of the APMB through gravity forward modeling. Thermomechanical modeling in combination with the geometry parameterization presented in chapter 2 and surface deformation data further constrains the geometry of the upper part of the magma body and identifies the key parameters that contribute to the observed uplift pattern. The chapter demonstrates how joining different modeling techniques creates several links between surface observations and sub-surface processes.

Chapter 4: Many magma bodies are expected to contain a reservoir of exsolved volatile components such as CO_2, H_2O and SO_2 in their roof zone which exerts a buoyancy force on the overlying crust. In case of an eruption, all volatiles can escape the system, instantly removing the buoyancy force and leading to syn-eruptive subsidence. This study utilizes thermomechanical modeling to estimate the surface deformation caused by the growth and removal of such a volatile reservoir. A scaling law is derived which describes the vertical surface deformation as a function of volatile volume, density and depth as well as crustal rigidity. The law is then applied to the 2015 eruption of the Chilean stratovolcano Calbuco to estimate the contribution of the buoyant reservoir to the observed syn-eruptive subsidence.

Chapter 5: This chapter summarizes the findings of chapters 2-4, provides concluding remarks and discusses the implications of the findings for geodynamic modeling of magmatic systems. It also includes an outlook on future improvements that can build upon the findings to further improve numerical studies.

1.3 Volcano deformation modeling

The most commonly used observation in numerical studies of magmatic systems is surface deformation. Data is usually provided by global positioning system (GPS) or interferometric synthetic aperture radar (InSAR) surveys. Less frequently used tools include tilt- and strainmeters. The following two sections will introduce two commonly used techniques to model the observed deformation.

1.3.1 Analytical solutions

Volcano deformation is usually interpreted to be the result of pressure changes at depth which cause the host rock to deform. The pressure changes are modeled as idealized geometric shapes that inflate in response to new magma supply from deeper sources or deflate in response to magma moving to other crustal locations or the surface.

The most commonly used model is the "MOGI source", a pressure point source embedded in an elastic half-space (Mogi, 1958) which is based on earlier work from Sezawa (1931), Anderson (1937), and Yamakawa (1955). With this assumption, surface displacement is given by:

$$u_z = \frac{(1-\nu)a^3\Delta P}{G}\frac{d}{(r^2+d^2)^{3/2}}, \tag{1.1}$$

$$u_r = \frac{(1-\nu)a^3\Delta P}{G}\frac{r}{(r^2+d^2)^{3/2}}, \tag{1.2}$$

where u_z and u_r are the vertical and radial displacement components at the surface respectively. ν is the Poisson's ratio of the host rock, a the radius of a spherical cavity, ΔP the pressure change in the cavity, G the shear modulus of the host rock, d the depth of the center of the point source and r the radial distance to the center of the point source projected to the surface. An alternative form of equations 1.1 and 1.2 involves the volume change ΔV in place of cavity size, pressure change and host rock shear modulus (Segall, 2010):

$$u_z = \frac{(1-\nu)\Delta V}{\pi}\frac{d}{(r^2+d^2)^{3/2}}, \tag{1.3}$$

$$u_r = \frac{(1-\nu)\Delta V}{\pi}\frac{r}{(r^2+d^2)^{3/2}}. \tag{1.4}$$

The model was later extended by McTigue (1987) to account for the finite size of a spherical magma body. Yang et al. (1988) provided another improvement of the equation to work for arbitrary spheroids.

Around the same time, Okada (1985) presented solutions for rectangular boxes to cover dikes and sills. Fialko et al. (2001a) approximates sills and dikes with the "penny-shaped crack", a more natural disc like feature that has thin tips and is thicker in the center.

Most of these analytical solutions have been validated with finite element modeling (e.g., Yang et al., 1988; Taylor et al., 2021) for the case that the depth of the deformation source is at least twice its radius (Taylor et al., 2021) and are computationally so cheap that observed surface deformation can be almost instantly inverted. But they are also associated with a number limiting simplifications. The assumption of the crust as a purely elastic half-space was improved by Del Negro et al. (2009). Williams and Wadge (2000) present multiple methods with varying degrees of complexity to correct for the effect of topography which is usually significant at volcanoes. Remaining issues include the assumptions of a homogeneous crust and simplified cavity geometry. Equations 1.1-1.4 also do not allow for any estimations on the total magma volume (only volume change) or its rheology. Finally, all the above-mentioned studies neglect that magma is usually buoyant at crustal storage levels (Vigneresse and Clemens, 2000).

1.3.2 Continuum mechanics models

With increasing computational power, the number of studies that utilize continuum mechanics like finite element (FE) or finite difference (FD) models has also increased. They support topography, complex model geometries and different rheologies. Some studies still use the approach of the extending cavities in this more advanced frame work (e.g., Dieterich and Decker, 1975; Charco and Sastre, 2014). The host rock is usually layered or entirely heterogeneous in these studies (e.g., Hickey et al., 2013; Henderson and Pritchard, 2017) and temperature-dependent-visco-elastic rheologies are common (e.g., Pearse and Fialko, 2010; Hickey et al., 2016). Some studies use more complex geometries that are based on geophysical constraints (e.g., Gottsmann et al., 2017).

But all of the above-mentioned studies still use the approach of the internal boundary condition (i.e. expanding/contracting pressure source). Consequently, the magma or magmatic mush is not modeled and none of its properties like rheology or density can be investigated. All processes that are expecting to take place inside the magma reservoir are neglected apart from their influence on pressure/volume. The most notable neglect is that of buoyancy with few exceptions (e.g., Fialko and Pearse, 2012; Sigmundsson et al., 2020). That is despite the fact that magmas rarely intrude at levels of neutral buoyancy (Vigneresse and Clemens, 2000) as shown by the commonly negative Bouguer anomaly detected above large magma bodies (e.g., Götze and Kirchner, 1997; DeNosaquo et al., 2009).

An exception is the study of Reuber et al. (2018) which includes partially molten areas of the crust as low-linear-viscous material of lower density. It is also one of few studies that utilizes a non-symmetric 3D initial setup and plastic rheology (i.e. allowing the brittle failure of rocks and the formation of shear zones).

1.4 Magmatic processes modeling

While most magmatic system modeling studies aim at linking surface deformation at a specific volcano to the emplacement (in case of uplift) or drainage (in case of syn-eruptive subsidence) of magma, other projects focus on specific processes that could be applicable to many different magmatic systems. To reduce the numerical cost, these studies often limit equations to the vertical dimension. Anderson and Segall (2011) present a model relating dome growth, magma overpressure and friction laws for conduit plugs. Jackson et al. (2018) deals with the thermo-chemical evolution of magma storage systems. Maccaferri et al. (2011) develop a 2D model for dike propagation in an elastic medium.

Studies like these might be able to find alternative explanations for observations that are traditionally interpreted in only one way. They can also be used to estimate the magnitude of effects that a process can have, advising future studies to consider or neglect the process.

1.5 Modeling challenges

The reason why so few previous studies have attempted to model magmatic systems including the magma dynamics (see section 1.3.2) is that it leads to a number of different challenges:

(i) Magmatic systems are 3D features that cannot be reduced to 2D. Unlike a subduction zone which may be homogeneous on a scale of hundreds of kilometers

along the trench, magma bodies often do not exceed a few kilometers in any direction. Even reducing a spherical body to a circular body in 2D introduces large errors as the solution will be equivalent to an infinite pipe instead of a sphere. This issue is demonstrated in section 4.E. Running models in 3D results in a cubic dependence of the number of degrees of freedom on resolution compared to a quadratic dependence in 2D.

(ii) Another issue that leads to increased computational cost is that magmatic systems can contain small scale features like melt channels or complex shaped magma bodies which necessitate a high resolution.

(iii) As magmas introduce a lot of heat into the crust, it is important to use temperature dependent viscosity laws for the crustal units which are more expensive to solve than linear viscosities. Steep temperature gradients also lead to strong viscosity contrasts between the different units.

(iv) While flow laws relating stress, temperature and effective viscosity exist for a lot of rocks through experimental studies, they remain unexplored for partial melts and magmatic mushes.

(v) Crustal magma bodies are usually revealed by seismic imaging techniques. As these constraints are often blurry, the real shape of the magma body remains ambiguous. For poorly constrained material parameters, it is common to test different values but testing different geometries requires a parameterization scheme to keep the number of variable parameters manageable.

Challenges (i) to (iii) can all be addressed by utilizing a numerical code that is efficient and scales well on massive parallel computing clusters. Section 1.6 introduces the code used for all studies within this thesis. To deal with challenge (iv), melt-bearing domains (i.e. magma bodies) are approximated with a low linear viscosity as they can be expecting to be significantly weaker than crustal rocks in any case. As (v) is a problem that is relevant to many geodynamic modeling problems, a flexible parameterization is developed in this thesis to address this issue (see chapter 2).

1.6 Thermomechanical model

All studies presented in this thesis utilize the 3D thermomechanical finite difference code LaMEM (Kaus et al., 2016). To discretize the equations of sections 1.6.1 and 1.6.2, LaMEM uses a staggered grid in combination with a marker-in-cell approach (Harlow and Welch, 1965). With the exception of section 2.3.2 all studies presented here use an internal free surface to include topography and track surface deformation. The surface is supported by sticky-air (Crameri et al., 2012) and a stabilization routine that facilitates large time steps (Kaus et al., 2010; Duretz et al., 2011). Free slip conditions are applied along the boundaries of the model domain, setting velocities components that are perpendicular to the boundaries to zero.

1.6.1 Conservation equations

LaMEM solves the coupled system of equations that describe conservation of momentum, mass and energy:

$$\frac{\partial \tau_{ij}}{\partial x_j} - \frac{\partial P}{\partial x_i} + \rho g_i = 0, \tag{1.5}$$

$$\frac{1}{K}\frac{DP}{Dt} - \alpha\frac{DT}{Dt} + \frac{\partial v_i}{\partial x_i} = 0, \tag{1.6}$$

$$\rho C_p \frac{DT}{Dt} = \frac{\partial}{\partial x_i}\left(k\frac{\partial T}{\partial x_i}\right) + H. \tag{1.7}$$

τ_{ij} is the Cauchy stress deviator, $x_i (i = 1, 2, 3)$ denotes the Cartesian coordinates, P is pressure (positive in compression), ρ density, g_i the gravitational acceleration vector, K the bulk modulus, α the thermal expansion coefficient, T the temperature, v_i the velocity vector, C_p the specific heat capacity, k the thermal conductivity, H the volumetric heat source and D/Dt is the material time derivative. Velocity, pressure and temperature are the primary unknowns. τ_{ij} is defined as follows:

$$\tau_{ij} = \sigma_{ij} + P\delta_{ij}, \tag{1.8}$$

where σ_{ij} is the full stress tensor and δ_{ij} is the Kronecker delta.

1.6.2 Rheology equations

The stress-strain-relationship is characterized by a visco-elasto-plastic rheology where the strain rate is the sum of the elastic, viscous and plastic components:

$$\dot{\varepsilon}_{ij} = \frac{1}{2}\left(\frac{\partial v_i}{\partial x_j} + \frac{\partial v_j}{\partial x_i}\right) - \frac{1}{3}\frac{\partial v_k}{\partial x_k}\delta_{ij} = \dot{\varepsilon}^{\mathrm{el}}_{ij} + \dot{\varepsilon}^{\mathrm{vi}}_{ij} + \dot{\varepsilon}^{\mathrm{pl}}_{ij}. \tag{1.9}$$

$\dot{\varepsilon}_{ij}$ denotes the deviatoric strain rate tensor, while $\dot{\varepsilon}^{\mathrm{el}}_{ij}$, $\dot{\varepsilon}^{\mathrm{vi}}_{ij}$ and $\dot{\varepsilon}^{\mathrm{pl}}_{ij}$ represent the elastic, viscous and plastic strain rate components.

The elastic component can be expressed as:

$$\dot{\varepsilon}^{\mathrm{el}}_{ij} = \frac{1}{2G}\frac{D\tau_{ij}}{Dt} = \frac{1}{2G}\frac{\tau_{ij} - \tau^*_{ij}}{\Delta t}, \tag{1.10}$$

where G is the elastic shear modulus and $D\tau_{ij}/Dt$ corresponds to the objective derivative of the stress tensor which can be approximated as a function of the current stress tensor (τ_{ij}) and the advected and rotated stress history of the previous time step (τ^*_{ij}) as well as the time step Δt.

The viscous component can be expressed as:

$$\dot{\varepsilon}^{\mathrm{vi}}_{ij} = \frac{\tau_{ij}}{2\eta_{\mathrm{eff}}} = \dot{\varepsilon}^{\mathrm{lin}}_{ij} + \dot{\varepsilon}^{\mathrm{dif}}_{ij} + \dot{\varepsilon}^{\mathrm{dis}}_{ij}, \tag{1.11}$$

where η_{eff} is the effective creep viscosity which may be linear (i.e. Newtonian, η_{lin}), temperature dependent (i.e. diffusion creep, eq. 1.12), temperature and strain rate dependent (i.e. dislocation creep, eq. 1.13) or a combination of multiple mechanisms (eq. 1.19). $\dot{\varepsilon}^{\mathrm{lin}}_{ij}$, $\dot{\varepsilon}^{\mathrm{dif}}_{ij}$ and $\dot{\varepsilon}^{\mathrm{dis}}_{ij}$ are the strain rates of linear, diffusion and dislocation creep.

$$\eta_{\mathrm{dif}} = \frac{1}{2}(B_{\mathrm{dif}})^{-1}\exp\left(\frac{E_{\mathrm{dif}} + V_{\mathrm{dif}}P}{RT}\right) \tag{1.12}$$

$$\eta_{\mathrm{dis}} = \frac{1}{2}(B_{\mathrm{dis}})^{-\frac{1}{n}}(\dot{\varepsilon}^{\mathrm{dis}}_{\mathrm{II}})^{\frac{1}{n}-1}\exp\left(\frac{E_{\mathrm{dis}} + V_{\mathrm{dis}}P}{nRT}\right) \tag{1.13}$$

η_{dif} and η_{dis} are the viscosities of diffusion and dislocation creep respectively. Likewise, B_{dif} and B_{dis} are the creep constants, E_{dif} and E_{dis} the activation energies and V_{dif} and V_{dis} the activation volumes of the respective flow laws. n is the powerlaw exponent

and R the universal gas constant. The subscript $_{\mathrm{II}}$ denotes the square root of the second invariant of a tensor. In the instance of strain rate:

$$\dot{\varepsilon}_{\mathrm{II}} = \left(\frac{1}{2}\dot{\varepsilon}_{ij}\dot{\varepsilon}_{ji}\right)^{1/2}. \tag{1.14}$$

For symmetric tensors $\dot{\varepsilon}_{ij}\dot{\varepsilon}_{ji} = \dot{\varepsilon}_{ij}\dot{\varepsilon}_{ij}$.

Substituting equations 1.10 and 1.11 into equation 1.9, and splitting the known from the unknown terms yields:

$$\dot{\varepsilon}_{ij} + \frac{\tau^*_{ij}}{2G\Delta t} = \frac{\tau_{ij}}{2G\Delta t} + \dot{\varepsilon}^{\mathrm{lin}}_{ij} + \dot{\varepsilon}^{\mathrm{dif}}_{ij} + \dot{\varepsilon}^{\mathrm{dis}}_{ij} + \dot{\varepsilon}^{\mathrm{pl}}_{ij}. \tag{1.15}$$

The left-hand side of equation 1.15 represents the effective deviatoric strain rate:

$$\dot{\varepsilon}^{\mathrm{eff}}_{ij} = \dot{\varepsilon}_{ij} + \frac{\tau^*_{ij}}{2G\Delta t}. \tag{1.16}$$

After substituting equation 1.16 into equation 1.15, it can be expressed using the square root of the second invariant of stress and strain rate (eq. 1.14) as all right-hand side terms are proportional to the same deviatoric stress tensor:

$$\dot{\varepsilon}^{\mathrm{eff}}_{\mathrm{II}} = \frac{\tau_{\mathrm{II}}}{2G\Delta t} + \dot{\varepsilon}^{\mathrm{lin}}_{\mathrm{II}} + \dot{\varepsilon}^{\mathrm{dif}}_{\mathrm{II}} + \dot{\varepsilon}^{\mathrm{dis}}_{\mathrm{II}} + \dot{\varepsilon}^{\mathrm{pl}}_{\mathrm{II}}. \tag{1.17}$$

The viscous strain rate terms can be expressed as functions of stress and viscosity:

$$\dot{\varepsilon}^{\mathrm{eff}}_{\mathrm{II}} = \frac{\tau_{\mathrm{II}}}{2G\Delta t} + \frac{\tau_{\mathrm{II}}}{2\eta_{\mathrm{lin}}} + \frac{\tau_{\mathrm{II}}}{2\eta_{\mathrm{dif}}} + \frac{\tau_{\mathrm{II}}}{2\eta_{\mathrm{dis}}} + \dot{\varepsilon}^{\mathrm{pl}}_{\mathrm{II}}. \tag{1.18}$$

As the dislocation strain rate term depends on itself (eq. 1.13), equation 1.18 can be expressed as:

$$\dot{\varepsilon}^{\mathrm{eff}}_{\mathrm{II}} = \frac{\tau_{\mathrm{II}}}{2G\Delta t} + \frac{\tau_{\mathrm{II}}}{2\eta_{\mathrm{lin}}} + \frac{\tau_{\mathrm{II}}}{2\eta_{\mathrm{dif}}} + \left(\frac{\tau_{\mathrm{II}}}{2\eta_{\mathrm{dis}_0}}\right)^n + \dot{\varepsilon}^{\mathrm{pl}}_{\mathrm{II}}, \tag{1.19}$$

where η_{dis_0} is the strain rate independent part of η_{dis}:

$$\eta_{\mathrm{dis}_0} = \frac{1}{2}(B_{\mathrm{dis}})^{-\frac{1}{n}} \exp\left(\frac{E_{\mathrm{dis}} + V_{\mathrm{dis}}P}{nRT}\right). \tag{1.20}$$

This formulation (eq. 1.19) shows that the rheological model can account for multiple viscous deformation mechanisms. At the same time, the rheology can be simplified by omitting terms from the right-hand side. The dominant mechanism will be the one with the lowest viscosity. The formulation also ensures that elastic deformation dominates at small time scales and viscous deformation at large time scales. If Δt is small, the first term on the right-hand side becomes large, so deformation is characterized by the shear modulus G. If Δt is large, the term becomes small, so deformation is characterized by the viscous terms. As equation 1.19 cannot be solved analytically, an iterative approach is necessary for each node of the numeric grid. This is demonstrated in section 1.6.3.

The plastic strain rate is defined as follows:

$$\dot{\varepsilon}^{\mathrm{pl}}_{ij} = \dot{\lambda}\frac{\partial Q}{\partial \sigma_{ij}}, \tag{1.21}$$

where $\dot{\lambda}$ is the plastic multiplier and the plastic flow potential Q is defined as:

$$Q = \tau_{\mathrm{II}} - \sin(\psi)P, \tag{1.22}$$

where ψ is the dilation angle. As we assume incompressible plasticity ($\psi = 0$), equation 1.22 can be simplified to:

$$Q = \tau_{\mathrm{II}}. \tag{1.23}$$

Substituting equation 1.23 into equation 1.21 yields:

$$\dot{\varepsilon}_{ij}^{\mathrm{pl}} = \dot{\lambda}\frac{\partial \tau_{\mathrm{II}}}{\partial \sigma_{ij}} = \dot{\lambda}\frac{\tau_{ij}}{2\tau_{\mathrm{II}}}. \tag{1.24}$$

The second component of plasticity is the plastic yield function:

$$F = \tau_{\mathrm{II}} - \sin(\phi)P - \cos(\phi)c_0, \tag{1.25}$$

where ϕ is the friction angle and c_0 the cohesion. To solve the visco-elasto-plastic problem, the following steps are performed:

(i) τ_{II} is iteratively calculated using equation 1.19 and assuming $\dot{\varepsilon}_{\mathrm{II}}^{\mathrm{pl}} = 0$ (i.e. the visco-elastic case).

(ii) The yield function F is computed.

(iii) If $F \leq 0$, all stress is accommodated by visco-elastic deformation and $\dot{\lambda} = \dot{\varepsilon}_{\mathrm{II}}^{\mathrm{pl}} = 0$.

(iv) If $F > 0$, plastic deformation occurs. As the plastic flow potential is independent of pressure (eq. 1.23), τ_{II} can be adjusted to fulfill $F = 0$ without a change in pressure, $\dot{\lambda} > 0$ and $\dot{\varepsilon}_{\mathrm{II}}^{\mathrm{pl}}$ can be computed using the adjusted τ_{II} and a rearranged equation 1.19:

$$\dot{\varepsilon}_{\mathrm{II}}^{\mathrm{pl}} = \dot{\varepsilon}_{\mathrm{II}}^{\mathrm{eff}} - \frac{\tau_{\mathrm{II}}}{2G\Delta t} - \frac{\tau_{\mathrm{II}}}{2\eta_{\mathrm{lin}}} - \frac{\tau_{\mathrm{II}}}{2\eta_{\mathrm{dif}}} - \left(\frac{\tau_{\mathrm{II}}}{2\eta_{\mathrm{dis}_0}}\right)^n. \tag{1.26}$$

1.6.3 Local iterations

Equation 1.18 is commonly (e.g., Billen and Hirth, 2007; Stadler et al., 2010) approximated with the use of a harmonic mean:

$$\dot{\varepsilon}_{\mathrm{II}}^{\mathrm{eff}} = \frac{1}{2}\tau_{\mathrm{II}}\left(\frac{1}{G\Delta t} + \frac{1}{\eta_{\mathrm{lin}}} + \frac{1}{\eta_{\mathrm{dif}}} + \frac{1}{\eta_{\mathrm{dis}}}\right) + \dot{\varepsilon}_{\mathrm{II}}^{\mathrm{pl}}. \tag{1.27}$$

This formulation does however have the issue that η_{dis} depends on the dislocation creep stain rate $\dot{\varepsilon}_{\mathrm{II}}^{\mathrm{dis}}$ which is unknown. Using $\dot{\varepsilon}_{\mathrm{II}}^{\mathrm{eff}}$ to compute η_{dis} leads to an inaccurate and time step dependent (see eq. 1.16) result. This is illustrated in Figure 1.2 which shows 0D and 1D examples of stress evolution using local iterations (eq. 1.19) and the harmonic mean (eq. 1.27). The harmonic mean will be accurate if the rheology does not include dislocation creep or solely includes dislocation creep as the effective strain rate and dislocation creep strain rate will be identical in the latter case.

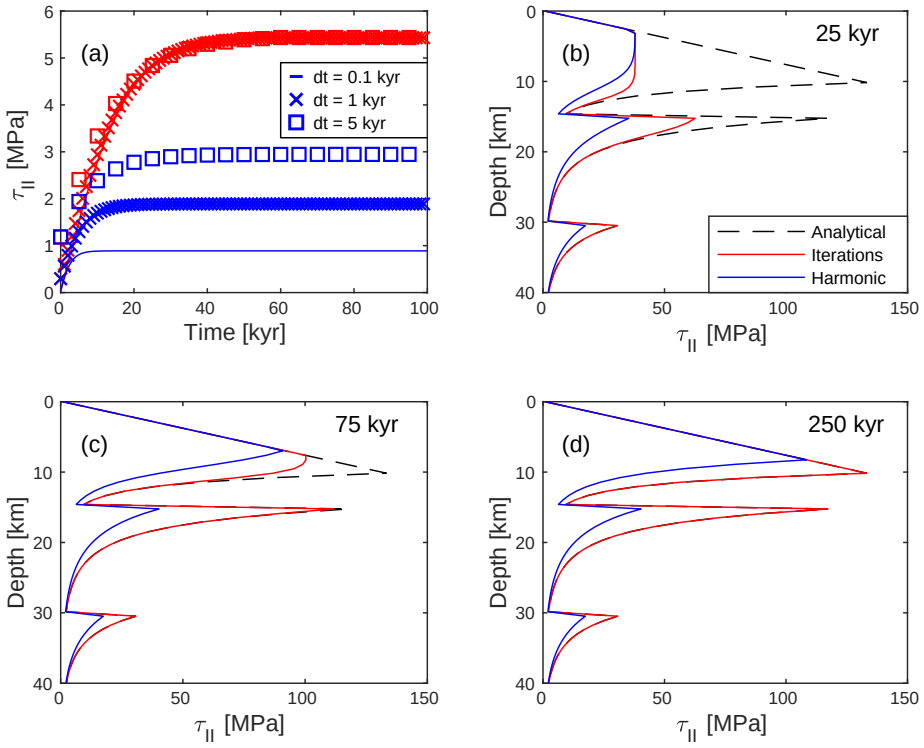

FIGURE 1.2: Comparison of stress evolution using local iterations (eq. 1.19, red) and the harmonic mean (eq. 1.27, blue). (a) Visco-elastic 0D example. Symbols correspond to the time step that was employed. Using local iterations reaches the viscous limit independently of the time step whereas the harmonic mean produces time step dependent results that do not converge to the correct solution. (b-d) Different snapshots of a visco-elasto-plastic 1D example for a layered crust with a linear temperature profile. Dashed black line shows the visco-plastic analytical solution of the stress profile. Both curves have reached steady state after 250 kyr. Table 1.1 shows the parameters used to produce the examples.

TABLE 1.1: Material parameters for stress evolution examples

Parameter		0D	1D		
			UC	MC	LC
G	[Pa]	5e9	20e9	35e9	50e9
η_{lin}	[Pa s]	1e22	-	-	-
B_{dis}	[$\text{Pa}^{-\text{n}}\,\text{s}^{-1}$]	3.1e-20	1.55e-17	1.68e-25	7.68e-21
n		2.3	2.3	3.3	4.2
E_{dis}	[$\text{J}\,\text{mol}^{-1}$]	154e3	154e3	186.5e3	445e3
ϕ	[°]	-	30	30	30
c_0	[Pa]	-	1e6	1e6	1e6
$\dot{\varepsilon}_{\text{II}}$	[s^{-1}]	1e-15	1e-15	1e-15	1e-15
T	[K]	723	273-573	573-873	873-1073
ρ	[$\text{kg}\,\text{m}^{-3}$]	-	2700	2800	2900

1.6.4 Strengths and weaknesses

As mentioned in section 1.3, the effects of buoyancy are usually neglected in the interpretation of volcanic surface deformation. LaMEM is driven by buoyancy forces (eq. 1.5) and therefore a good tool to include those effects. Additional strengths are the temperature- and strain rate dependent visco-elasto-plastic rheology, the free surface, the scalability on massive parallel clusters (Kaus et al., 2016) and the coupling to the initial geometry generator geomIO (Bauville and Baumann, 2019, `https://bitbucket.org/geomio/geomio`).

The disadvantage of using LaMEM is the inability to use the internal boundary condition (i.e. expanding pressure source) that is commonly utilized to approximate magma intrusion. Whereas expanding or contracting cavities can be implemented into finite element frameworks with flexible grids, they are difficult to include into the regular grid of LaMEM. Section 5.6.1 presents an outlook of how future LaMEM studies could include intrusion effects. Sections 5.6.2 to 5.6.4 discuss additional features that would be desirable for numerical modeling of magmatic systems.

1.7 Author contributions

Chapter 2: Geodynamic Modeling with Uncertain Initial Geometries - *A. Spang, T.S. Baumann, B.J.P. Kaus*
AS developed the concept and methodology of the study, implemented the methodology, performed the modeling, processed the results and wrote the manuscript. TSB contributed to the development of the methodology, reviewed and edited the manuscript. BJPK gave advice on the applications, reviewed and edited the manuscript and acquired project funding.
Chapter 3: Multiphysics Approach to Constrain the Dynamics of the Altiplano-Puna Magmatic System - *A. Spang, T.S. Baumann, B.J.P. Kaus*
AS development the concept of the study, performed the modeling, processed and analyzed the results and wrote the manuscript. TSB contributed to the concept and methodology of the study, reviewed and edited the manuscript. BJPK developed the initial concept of the study, reviewed and edited the manuscript and acquired project funding.
Chapter 4: Quantification of Volcano Deformation caused by Volatile Accumulation and Release - *A. Spang, M. Burton, B.J.P. Kaus, F. Sigmundsson*
AS developed the methodology of the study, performed the modeling, processed and analyzed the results and wrote the manuscript. MB provided the concept of the study, contributed to the methodology and reviewed and edited the manuscript. BJPK contributed to the methodology, reviewed the manuscript and acquired project funding. FS contributed to the methodology and reviewed and edited the manuscript.

1.8 Software

This thesis was written in *TeXstudio* using the "Masters/Doctoral Thesis" template from `www.latextemplates.com`. *ParaView* was used to visualize modeling results and create figures. Code development was performed in *Visual Studio Code* and *Matlab*. *Python* and *Matlab* were used for data analysis and figure creation. *Inkscape* was used to create and edit figures. All other software is mentioned within the chapters.

Chapter 2

Geodynamic modeling with uncertain initial geometries

This chapter has been accepted in:
Spang, A., Baumann, T. S., & Kaus, B. J. P. (2022). Geodynamic Modeling with Uncertain Initial Geometries. *Geochemistry, Geophysics, Geosystems.*

Abstract

Geodynamic codes have become fast and efficient enough to facilitate sensitivity analysis of rheological parameters. With sufficient data, they can even be inverted for. Yet, the geodynamic inverse problem is often regularized by assuming a constant geometry of the geological setting (e.g., shape, location and size of salt diapirs or magma bodies) or approximating irregular bodies with simple shapes like boxes, spheres or ellipsoids to reduce the parameter space. Here, we present a simple and intuitive method to parameterize complex 3D bodies and incorporate them into geodynamic inverse problems. The approach can automatically create an entire ensemble of initial geometries, enabling us to account for uncertainties in imaging data. Furthermore, it allows us to investigate the sensitivity of the model results to geometrical properties and facilitates inverting for them. We demonstrate the method with two examples. A salt diapir in an extending regime and free subduction of an oceanic plate under a continent. In both cases, small differences in the model's initial geometry lead to vastly different results. Be it the formation of faults or the velocity of plates. Using the salt diapir example, we demonstrate that, given an additional geophysical observation, we are able to invert for uncertain geometric properties. This highlights that geodynamic studies should investigate the sensitivity of their models to the initial geometry and include it in their inversion framework. We make our method available as part of the open-source software geomIO.

Plain language summary

Computer models of geological settings have become a popular tool of research. They require the user to provide information on where the different geological units (rock layers, salt domes, magma bodies etc.) start and end as well as material parameters like density and strength of the units. As many of these input parameters are not well known, a lot of studies perform multiple simulations with different parameter combinations to investigate the influence the individual parameters and their uncertainties have. However, the initial geometry often remains fixed as it is difficult to

describe with only few parameters and therefore unrealistic to vary. Here, we present a new method to describe and manipulate the geometry of geological units with a small number of parameters. This allows us to also vary the initial geometry and investigate how the model results depend on it. We apply our method to a salt diapir and a subduction zone to demonstrate the impact of initial geometry on the simulation results. To make our method available to the community, we implement it as a tool into geomIO, an open-source software package to generate initial geometries for geodynamic models.

2.1 Introduction

Geodynamic modeling has become a powerful tool to investigate how different mechanical and thermodynamical parameters influence and control geological systems such as orogens, subduction zones, magmatic systems, basins and other terrestrial bodies (e.g., Alisic et al., 2010; Jadamec et al., 2013; Baumann and Kaus, 2015; Ratnaswamy et al., 2015; Reuber et al., 2018). With the help of observations, the abovementioned studies can constrain rheology, density and thermal properties of geological units with forward and inverse approaches.

It is common practice in geodynamic modeling to assign material properties such as density and rheology in space with the help of geometrical objects that approximate units like rock layers, magma bodies or tectonic plates (Zelst et al., 2021). There is a collection of open-source software packages covering this task. UWGeodynamics (Beucher et al., 2019, `https://uwgeodynamics.readthedocs.io/`) uses simple geometrical objects and polyhedra to generate setups for the Underworld code (Moresi et al., 2002, `https://www.underworldcode.org/`). GemPy (e.g., Varga et al., 2019; Schaaf et al., 2021, `https://www.gempy.org/`) allows the creation of layered and folded rock units, including faults and shapes like magma bodies and provides tools for gravity modeling and uncertainty analysis. The Geodynamic World Builder (Fraters et al., 2019, `https://geodynamicworldbuilder.github.io/`) focuses on ocean settings like subduction zones and spreading centers and is compatible with various geodynamic codes. Tect_Mod3D (formerly SlabGenerator, e.g., Jadamec et al., 2013) is another software geared towards subduction zones. Easy (`https://easyinit.readthedocs.io/`) provides several tools to set initial conditions. geomIO (Bauville and Baumann, 2019, `https://bitbucket.org/geomio/geomio`) allows for the creation of 3D setups from vector graphic drawings (in Inkscape), provides gravity forward modeling and is coupled to the thermomechanical code LaMEM (Kaus et al., 2016).

Unlike the material properties themselves, the initial geometry of geodynamic models is usually treated as a constant throughout the study and not included in any parameter variations. This is because creating the initial geometry is, especially in three dimensions (3D), a time consuming process and parameterization is difficult (Zelst et al., 2021). While the density of a geological unit can be described with a single number, defining its location and boundaries involves a large number of parameters if its shape is more complex than a basic geometric bodies such as planes, boxes, spheres or ellipsoids. Because of that, many modeling studies (e.g, Pearse and Fialko, 2010; Baumann et al., 2014; Čížková and Bina, 2015, and previously mentioned geodynamic studies) do not only have to ignore the uncertainties that are associated with the initial geometry but also lose the ability to investigate the influence of the initial geometry on the model results. Other studies generate different initial geometries and demonstrate a link between geometry and results, but can either not parameterize the geometry

(e.g., Le Pourhiet et al., 2003) or are bound to simple properties like the thickness of a horizontal, planar layer (e.g., Duretz et al., 2020).

To facilitate the inclusion of a flexible geometry in geodynamic investigations, it needs to be efficiently parameterized with a number of geometrical parameters that does not outweigh the number of material parameters. Flexible geometries are commonly used in geomodeling (Wellmann and Caumon, 2018), potential-field modeling like gravity and magnetics (Jessell, 2001) and seismic inversion (Bosch et al., 2010). Techniques include voxel models (e.g., Guillen et al., 2004), discrete object modeling (e.g., Oldenburg and Pratt, 2007), flexible prisms (e.g., Fullagar et al., 2000), parameterized surfaces (e.g., Pereyra, 1996), explicit surfaces (e.g., Caumon et al., 2009) and implicit surfaces (e.g., Frank et al., 2007) but most approaches result in a collection of triangulated surfaces and/or voxel models (Galley et al., 2020).

It is our aim to present a method to intuitively parameterize and vary the 3D geometry of key features (e.g., salt domes, magma bodies, subducting slabs) of geodynamic models. The method is implemented as a tool in geomIO including a user manual and examples (`https://bitbucket.org/geomio/geomio/wiki/VaryGeomTutorial.md`) and is fully coupled to a state-of-the-art thermomechanical code in LaMEM (`https://bitbucket.org/bkaus/lamem/src/master/`). This facilitates the inclusion of geometric uncertainties in geodynamic modeling and enables us to constrain geometric properties of subsurface geological features with surface observations.

In section 2.2, we present the method and show examples of how it works for arbitrary shapes and subducting plates. In section 2.3, the method is applied to 2 different geological scenarios. (i) Seismic reflection reveals a salt diapir but its horizontal and vertical extent are uncertain. We generate an ensemble of possible initial geometries and demonstrate that they lead to distinctly different faulting patterns. This allows us to link geometric features to model results and constrain the geometry of the diapir with a synthetic surface observation. (ii) We model free subduction of an oceanic plate underneath a continent and investigate the dependence of the velocities of both plates on the initial dip angle of the subducting slab. We also track the evolution of the dip angle as the plate subducts and compare the results to natural observations.

2.2 Methods

Our method is based on changing a single body at a time. As the definition of any complex 3D shape requires a large number of coordinates, we always need a reference model or starting geometry, which may be any 3D volume that is not a non-manifold geometry. We then create parameters which describe a transformation of this reference model into a different shape. Section 2.2.1 describes our general transformation algorithm applicable to any shape, and section 2.2.2 shows an example of how it can be used to transform a sphere into a more complex shape. Section 2.2.3 shows how the method can be adapted for a subduction setting. Supplementary text 2.B and Figure 2.G.1 explain the workflow of using the method in a geodynamic study.

2.2.1 Transformation algorithm

2.2.1.1 Scaling parameters

To manipulate the reference model, we compute the intersection of the 3D body with a finite number of horizontal planes that are perpendicular to the z-direction. In a second step, we select a subset of the resulting two-dimensional (2D) polygons (red in Figure 2.1a), which are referred to as control polygons. For each of the control

polygons (P_i) we define two scaling parameters (Sx_i and Sy_i) and compute scaling parameters for all other polygons in the following manner:

(i) Polygons below the lowermost control polygon copy its scaling parameters.

(ii) The scaling parameters of polygons between two control polygons are linearly interpolated between those of the control polygons.

(iii) Polygons above the uppermost control polygon copy its scaling parameters.

To achieve a homogeneous transformation in the horizontal plane, Sx_i must equal Sy_i which reduces the number of necessary parameters to one per control polygon. Finally, there is a single parameter (Sz) to transform the body in the vertical direction.

2.2.1.2 Vertical scaling

To scale the body in the vertical direction, the spacing between the polygons is multiplied by the vertical scaling parameter (Sz):

$$z_{i,new} = (z_i - z_{ref}) * Sz + z_{ref} \tag{2.1}$$

Where z_i is the vertical coordinate of the polygon and z_{ref} is the reference depth of vertical scaling. If $Sz > 1$, the body is vertically extended, if $Sz < 1$, the body is shrunk. z_{ref} should be chosen in dependence of the object to be transformed. For shapes like magma or ore bodies that are not bound to another unit, it makes sense to use the body's center of mass while for a salt diapir, its base is more appropriate.

2.2.1.3 Horizontal scaling

To scale the body in the two horizontal directions, the following steps are applied to each polygon individually. First, we compute the position of the polygon's center of mass and transform the coordinates of all nodes on the polygon to be relative to it:

$$\begin{pmatrix} \vec{x_i}' & \vec{y_i}' \end{pmatrix} = \begin{pmatrix} \vec{x_i} & \vec{y_i} \end{pmatrix} - \begin{pmatrix} x_{i_c} & y_{i_c} \\ ... & \\ x_{i_c} & y_{i_c} \end{pmatrix} \tag{2.2}$$

Where $\vec{x_i}'$ and $\vec{y_i}'$ are vectors containing the relative coordinates of the nodes of the polygon, $\vec{x_i}$ and $\vec{y_i}$ are vectors containing the absolute coordinates of the nodes and x_{i_c} and y_{i_c} are the absolute coordinates of the polygon's center of mass. Then, all x-coordinates are multiplied by Sx_i and all y-coordinates by Sy_i. Lastly, the coordinates are transformed back into absolute values:

$$\begin{pmatrix} \vec{x}_{i,new} & \vec{y}_{i,new} \end{pmatrix} = \begin{pmatrix} \vec{x_i}' & \vec{y_i}' \end{pmatrix} * \begin{pmatrix} Sx_i & 0 \\ 0 & Sy_i \end{pmatrix} + \begin{pmatrix} x_{i_c} & y_{i_c} \\ ... & \\ x_{i_c} & y_{i_c} \end{pmatrix} \tag{2.3}$$

If $Sx_i > 1$, the polygon extends in x-direction and if $Sx_i < 1$, the polygon shrinks. The same is true for Sy_i and the y-direction.

2.2.1.4 Additional options

Equations 2.1 - 2.3 are the core of our method and sufficient to describe all operations used in the following example and the application in section 2.3.1. Supplementary text 2.C describes additional options that we implemented.

2.2.2 Example

For the sake of convenient visualization, we choose a sphere as our reference model. We represent the sphere with 21 equally spaced, horizontal polygons (Figure 2.1a) but the number of plain intersections is arbitrary. Polygons 13, 15 and 19 are chosen to be control polygons (red in Figure 2.1a) and for each one we set the parameters Sx and Sy (red in table 2.1). The other scaling parameters are then computed according to section 2.2.1.1 and used to transform the sphere in Figure 2.1a into the shape shown in Figure 2.1b. As we did not specify a vertical scaling parameter Sz, the body does not change its height. Figure 2.1c shows another example using the same parameters of table 2.1 with $Sz = 0.6$.

The procedure can be imagined as pulling ($S > 1$) or pinching ($S < 1$) a rubber object at the locations of the control polygons. The only difference being, that the top and bottom of the object are not fixed but deform together with the closest control polygon. To keep top or bottom fixed, simply make the first (bottom) or last (top) polygon a control polygon with $S = 1$.

The number and position of the control polygons and the scaling parameters can be chosen by the user. Examples of using the tool are given at: `https://bitbucket.org/geomio/geomio/wiki/VaryGeomTutorial.md`.

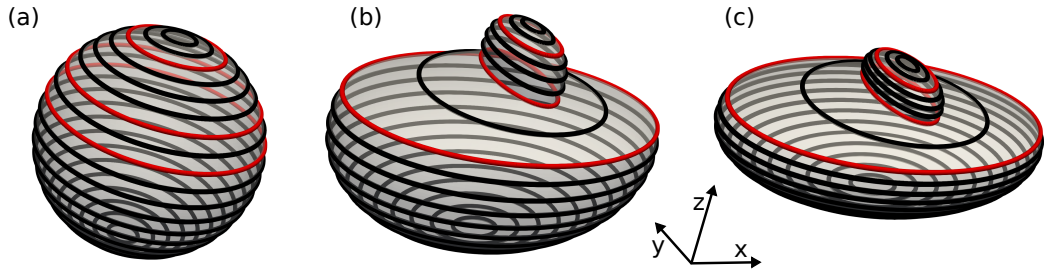

FIGURE 2.1: Illustration of 3D bodies as a set of 2D polygons. The three red slices are the control polygons which are used to transform the body. (a) Reference model sphere represented as horizontal polygons. (b) Sphere from 2.1a after transformation with the scaling parameters of table 2.1. (c) Sphere from 2.1a after transformation with $Sz = 0.6$ and the scaling parameters of table 2.1. Inset shows the orientation of the coordinate system.

2.2.3 Subduction zones

Subduction zones are frequently investigated in geodynamic modeling studies. A central element is the orientation and location of the subducting slab. In this case, it is more convenient to represent the subducting plate as a collection of vertical polygons (Figure 2.2). We automatically detect the polygon nodes that make up the slab part (red in Figure 2.2b) and rotate them by angle θ to change the subduction angle (blue in Figure 2.2b). For 3D slabs that dip obliquely to the orientation of the coordinate system (Figure 2.2a), we first detect the direction of dip and recalculate θ' in the plane of the polygons so that the entire slab is rotated correctly. Additional

TABLE 2.1: Scaling parameters used to transform the sphere in Figure 2.1a into the shapes in Figures 2.1b,c. Note that the polygon numbering goes from the bottom to the top. Only the red numbers are free parameters that need to be chosen. The black numbers are generated automatically, depending on the red ones.

Polygon	Sx	Sy
21	0.50	0.90
...	0.50	0.90
19	0.50	0.90
18	0.45	0.83
17	0.40	0.75
16	0.35	0.68
15	0.30	0.60
14	0.90	0.80
13	1.50	1.00
...	1.50	1.00
1	1.50	1.00

rotation centers can also be placed anywhere along the slab to bend the deeper parts (Figure 2.G.5). This can be useful when the dip of the slab is well constrained close to the surface but changes at depth like along the west coast of South America.

Subduction setups often require a weak zone of elevated temperature, lowered viscosity or lowered yield strength to facilitate slip of the slab along the overriding plate. We automatically generate a weak zone of desired thickness following the curvature of the slab from the surface to a desired depth (green in Figure 2.2). Likewise, we can automatically add oceanic crust of desired thickness to the top of the slab (light blue in Figure 2.2).

2.3 Applications

In this section, we present two examples of applications to geological scenarios. Section 2.3.1 focuses on fault development associated with a salt diapir in an extending regime, including forward simulations and inversion. In section 2.3.2, we investigate the dependence of plate velocity on the initial dip angle of a subducting plate and the evolution of the dip angle. Spang et al. (2021) presents a third application in 3D to a magmatic system.

2.3.1 Application I: Salt

Our method is especially useful when constraints from imaging studies are ambiguous like in the case of the Epsilon diapir in Norway (Jackson and Lewis, 2012). After a seismic survey, the stem of the diapir was interpreted to be about 300 m wide (green in Figure 2.3) but a drilling survey revealed it to be more than 1 km wide instead. Jackson and Lewis (2012) state that the location of the flanks can move hundreds of meters depending on the interpretation of the survey. The authors present a tear-drop-shaped post-drilling interpretation (dashed purple in Figure 2.3) of the diapir's extent but acknowledge that most of the margins are still uncertain. Jones and Davison (2014) revisit the data on the Epsilon diapir and present a much straighter interpretation (solid purple in Figure 2.3).

Here, we use the survey of the Epsilon diapir to show how different initial geometries, within the range of uncertainty of imaging data, can result in vastly different

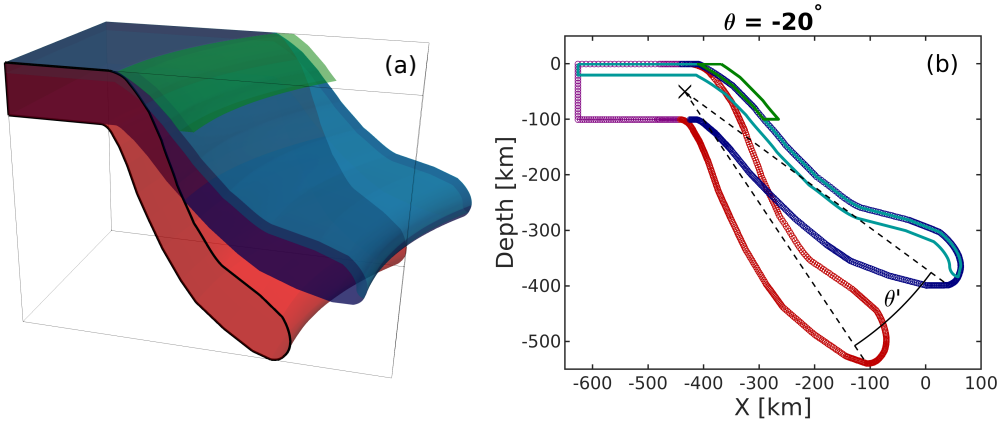

FIGURE 2.2: (a) 3D Example of a plate, subducting along a curved trench, drawn in geomIO (red) and an automatically generated variation with reduced subduction angle of 20° (blue). Alongside the variation, we can also automatically generate oceanic crust (light blue) and a weak zone (green) between slab and overriding plate. Black line shows one of the vertical polygons that the 3D volume is represented as inside our algorithm and is identical to the red+purple polygon in 2.2b. (b) Representation of the plates in 2.2a as a vertical polygons. Original in red, variation in blue, crust in light blue and weak zone in green. Purple nodes belong to both versions. Black cross shows the center of rotation.

model results. We also demonstrate how geodynamic models with variable initial geometries, supported by other observations, can help reduce ambiguity of imaging studies. Figure 2.3 shows the reflection profile and various interpretations. Without the information of the drilling survey, the red outline could also be a valid interpretation, so we use it as an initial guess and reference model for our variations. The dashed yellow lines show the location of four control polygons located at the basis, the thinnest (neck) and thickest (head) part of the diapir as well as on the transition from neck to head.

2.3.1.1 Faulting patterns in dependence of initial geometry

Using the red outline in Figure 2.3 as an initial guess or reference model, we create about 1500 different diapirs. For each variation, we generate a set of scaling parameters (S_1 to S_4) to be applied at the control polygons as well as one parameter (Sz) to vary the height of the diapir. Because it is a 2D example, S_1 to S_4 are equivalent to Sx_1 to Sx_4 and there are no Sy parameters. We generate the scaling parameters on a regular grid within the ranges given in table 2.G.3 and add random noise to sample the parameter space. The reference depth for scaling in the vertical direction is the base of the diapir.

We then model the evolution of each diapir in an extensional geodynamic setting for 100 kyrs, using the thermomechanical code LaMEM (Kaus et al., 2016). We employ a linear-visco-elasto-plastic rheology and a density contrast of 500 $\mathrm{kg\,m^{-3}}$. A more detailed description of the code and the material parameters can be found in supplementary text 2.D.

From the model output, we binarize the accumulated plastic strain to automatically identify faults that developed to accommodate the extension. With the help of principle component analysis, we extract preferred orientation (α), length (l), aspect

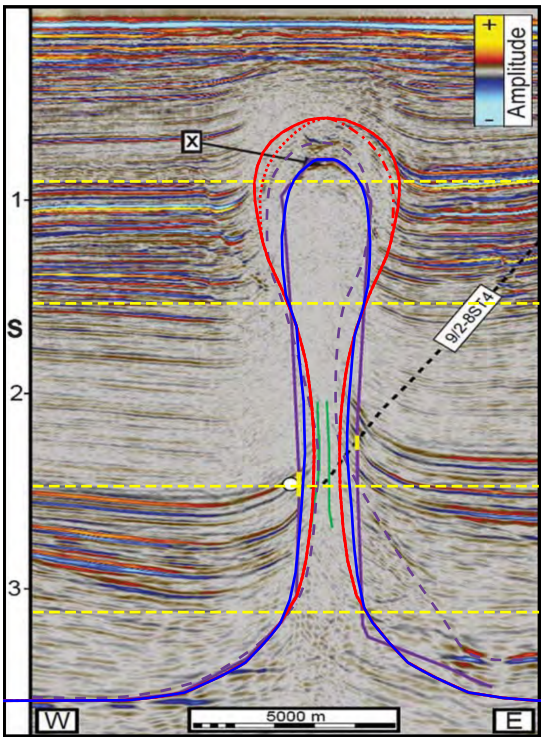

FIGURE 2.3: Seismic reflection profile of the Epsilon diapir modified from Jones and Davison (2014). Green lines show pre-drilling interpretation, dashed purple, post drilling interpretation of Jackson and Lewis (2012) and solid purple post-drilling interpretation of Jones and Davison (2014). Red line shows our symmetric initial guess and reference model. Dotted and dashed-dotted red lines show mirrored variations of red to test the effect of asymmetry. Solid blue line shows our synthetic 'true' geometry that we try to fit in section section 2.3.1.2. Dashed yellow lines show location of control polygons.

ratio (r) and the location (x, z) of the faults or fault systems. The aspect ratio of faults is computed by taking the ratio between the magnitudes of their two principle components (i.e. Eigenvalues).

2.3.1.2 Inverting for geometry

With a parameterized geometry, it is possible to invert for the unknown structure of the diapir with the help of an observable. Using a scaling parameter set of 1.2, 2.0, 0.8, 0.6 ($S_1 - S_4$) and 0.94 (Sz), we produce a synthetic diapir (blue in Figure 2.3) similar to the interpretation of (Jones and Davison, 2014). We then forward model the evolution of this diapir in an extensional setting for 100 kyrs which results in a single normal fault (Figure 2.4a). The size, location and orientation of that fault might be visible in a seismic study (Juhlin et al., 2010) and could serve as an observable which we can use to constrain the diapir geometry through inversion.

We compare the faults developed by the 1500 variations to our synthetic observation (fault in Figure 2.4a, developed by the blue diapir in Figure 2.3). After identifying the 50 best fitting models, we create 8 new variations with similar parameters for each one to improve our coverage in the area of low misfit (Sambridge, 1999a, Neighborhood algorithm). This procedure is commonly used to deal with non-linear and -unique inverse problems (e.g., Baumann and Kaus, 2015) and is repeated four times here, yielding a final ensemble of about 3100 variations. After 2 iterations, it was clear that the minimum for Sx_4 was close to our initial lower bound of 0.5 (table 2.G.3)

and we relaxed the bound to 0.25 for the 3rd and 4th iteration of the neighborhood algorithm.

We also perform a second inversion, using only 2 control polygons (locations are shown in Figure 2.6) alongside vertical scaling to investigate how robust the approach is. Because of the smaller parameter space, we test an initial set of about 500 variations and then add 4 × 400 variations with the neighborhood algorithm for the 2 control polygon case.

Computing a misfit between two geometric observations is not as straight forward as comparing numeric outputs and observations. To address this issue, Wijns et al. (2003) used human appraisal to rank modeled faulting patterns, while Boschetti et al. (2003) utilized self organizing maps to do the same. We compute the misfit of an individual fault pattern, by combining some of the geometric properties of the modeled fault and comparing them to our synthetic observation:

$$\Phi_i = \left(\frac{\sqrt{(|x_i| - |x_o|)^2 + (z_i - z_o)^2}}{l_n} + \frac{||\alpha_i| - |\alpha_o||}{\alpha_n} + \frac{|r_i - r_o|}{r_n} \right) \times N \tag{2.4}$$

Φ_i is the misfit of a fault to our synthetic observation. Subscript i corresponds to the geometry variation, subscript o to the synthetic observation and subscript n to a normalization constant for each property. The first term of the right hand side compares the location of the fault centers with x corresponding to the lateral and z to the vertical coordinate. α is the angle between the fault and the horizontal direction and r the aspect ratio of the fault. N is the number of faults that develop. l_n is 2 km, a tenth of the model width, α_n is 5° and $r_n = r_o$. These parameters were chosen to make sure that all three right hand side terms are in the range of 0 to 1 for the majority of models. Figure 2.4 shows how large each of the three terms of equation 2.4 are for 8 selected fault systems.

We decided to use the absolute values of x and α as section 2.4.1.1 suggests that the side, to which the faults develop, is not coupled to the geometry but is related to how the curved diapir boundaries intersect with the rectangular grid. This is supported by the fact that the issue persists at higher resolution models and disappears for the asymmetric cases (supplementary text 2.E and Figure 2.G.8).

2.3.2 Application II: Subduction

We use the method introduced in section 2.2.3 to test the dependence of plate velocity on the initial dip angle (β_0) of the subducting slab. Using a reference model, dipping with 60°, we test 16 variations in the range of 30° to 90°. We use a simple 2D model with an oceanic plate of 70 km thickness (corresponding to a thermal age of 30 Myr) subducting underneath a continent of 100 km thickness. Both plates are free (i.e. not fixed to the edges of the model) and as we do not prescribe any boundary velocities, the movement of the plates in entirely driven by the negative buoyancy of the cold slab. We test models with a 20 km (4 cells) and 30 km (6 cells) wide weak zone. Supplementary text 2.D provides more details on the setup and the thermomechanical code we use.

2.4 Results

2.4.1 Application I: Salt

2.4.1.1 Faulting patterns in dependence of initial geometry

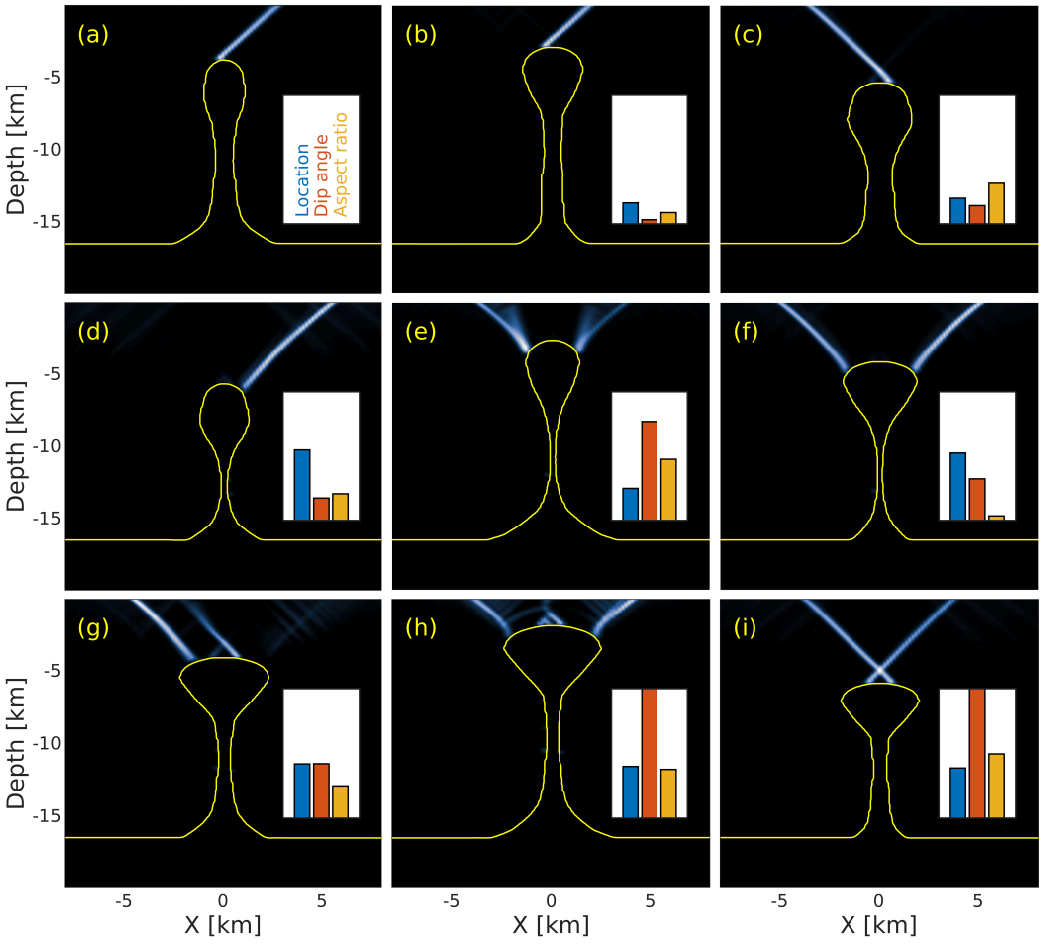

FIGURE 2.4: Accumulated plastic strain after 100 kyrs corresponding to normal faults that formed to accommodate the extension of the model. (a) Synthetic 'true' diapir (blue in Figure 2.3) and corresponding fault which serves as our synthetic observation, other faults are compared to (eq. 2.4). (b and c) 'Regular case': Deformation focuses on a single fault for different diapir heights. This happens for the majority of cases. (d) Deformation focuses on a single fault but the fault does not start at the center of the diapir top. (e) Deformation is not taken up by a single fault but two areas with a lot of small faults. (f) Faults form on both sides of the diapir. (g) Two parallel faults form with some minor opposite ones. (h) A large number of smaller faults develop. (i) Model develops two crossing faults. Insets show misfit of the observed fault/fault system to the synthetic observation in 2.4a. Blue bar corresponds to the location term, orange to the orientation term and yellow to the aspect ratio term of equation 2.4.

To accommodate the extension, the models start developing faults at the tip of the diapir as well as the surface. The faults then grow from the surface downwards or from the diapir upwards and eventually connect both (supplementary Figure 2.G.6). In the majority of cases, the strain then focuses on one of the two directions and a single fault forms, taking up most of the deformation. Both sides were preferred in a large number of models for all heights of diapirs (Figure 2.4b,c). In about 25% of the

cases, the fault did not connect to the center of the diapir, but instead it formed at the edges of the diapir top (Figure 2.4d–h). For some tall diapirs, the deformation did not focus on a single fault but was distributed over an area close to the surface (Figure 2.4e). In some cases, one dominant fault formed, but a part of the deformation was also accommodated by other parallel and opposite faults (Figure 2.4g,h). In few cases, two faults formed that shared the strain between them (Figure 2.4f,i).

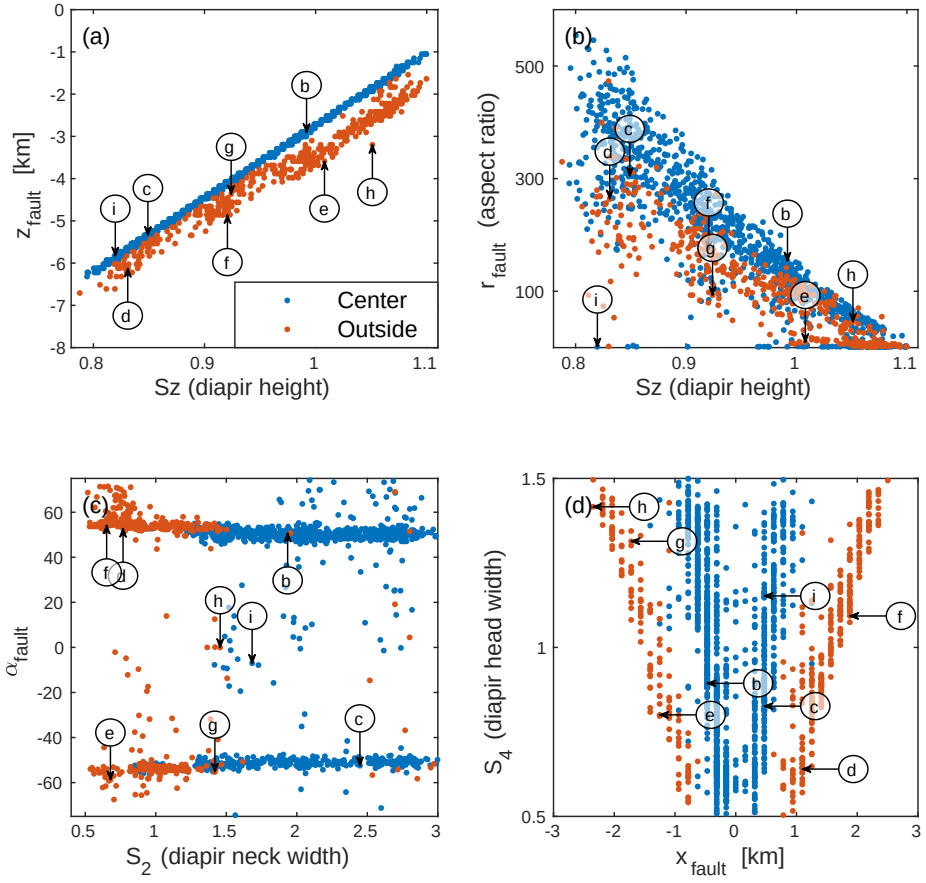

FIGURE 2.5: Different fault properties (α, r, x, z) in relation to scaling parameters. Arrows show where the examples in Figure 2.4b–i plot to relate fault types with the parameters. (a) Depth of the lower end of the fault in dependence of Sz. This allows for the distinction between faults that start from the center (blue) and faults that start from at the side (orange) of the diapir. Same color code in b–d. (b) Fault aspect ratio in dependence of Sz. (c) Fault orientation in dependence of S_2. $\alpha < 0$: fault goes to the left. (d) Lateral position of the fault center in dependence of S_4.

Figure 2.5 shows a selection of geometric fault properties in dependence of the scaling parameters applied to the diapir. Supplementary Figure 2.G.7 shows all relations between scaling parameters and fault properties. Intuitively, there is a good correlation between the height of diapir (Sz) and the depth of the lower end of the fault as the fault connects the top of the diapir to the surface (Figure 2.5a). It is, however, evident that there is some spread towards deeper fault tips as well. This deviation represents cases where the fault does not start at the tip or center of the diapir, but instead to one of the sides (Figure 2.4d–h). We use the relation between

Sz and the depth of the fault tip to discriminate between faults that connect to the center of the diapir (blue in Figure 2.5) and faults that connect to the sides (orange).

The aspect ratio scales similarly with Sz as the depth of the fault tip because long faults are not wider than short faults (Figure 2.5b). The spread is a bit bigger and there are more anomalous cases. Where Sz and r are small, two crossing faults developed (Figure 2.4i) and the image processing was not able to properly split them, returning flawed values for the width. Cases of low r and large Sz relate to those shown in Figure 2.4e,h and predominantly happen when the faults do not form in the center of the diapir (orange in Figure 2.5b).

Figure 2.5c shows that most faults have an angle of roughly 50 degrees. It also shows a striking dependence of the fault location on S_2 (the neck of the diapir). For small S_2, the faults form almost exclusively to the sides of the diapir (orange) while they occur predominantly in the center (blue) for high S_2. Overall, more faults extend to the right. Given that the diapirs are symmetric, this may be due to small asymmetries that arise from gridding.

Figure 2.5d relates the width of the diapir head (S_4) and the lateral coordinate of the fault center. It shows that the faults form further from the center of the domain, the wider the diapir is. This is the only correlation for S_4 (Figure 2.G.7). The figure also clearly shows the two different trends of faults forming in the center or at the sides of the diapir head with few exceptions. S_1 (width of the diapir base) and S_3 (width at transition zone from neck to head of the diapir) do not show any correlation with any of the faults' geometric properties (Figure 2.G.7).

We also tested two sets of models with the same scaling parameters but a slightly asymmetric reference model (red dotted and red dashed-dotted in Figure 2.3). The results are presented in supplementary text 2.E and Figure 2.G.8.

2.4.1.2 Inverting for geometry

After four iterations of the neighborhood algorithm, we have a total of 3100 models. Figure 2.6a shows the 200 diapirs that develop faults with the lowest misfit in comparison with the synthetic observation (fault in Figure 2.4a). All 200 are almost a perfect match for the head of the diapir in terms of height and shape. The transition between head and neck of the diapir shows very large spread over almost the entire range of possible extents. The neck and base of diapir show less spread but are not as well constrained compared as the top of the diapir.

Figure 2.6b shows the misfit of each model in dependence of the two most important parameters, the width of the diapir head (S_4) and the height of the diapir (Sz). Sz is the most well defined parameter with models outside the range of 0.9 to 1.0 showing large misfit. But inside that range, there is also a correlation between misfit and S_4 with the minimum in the area of 0.6. As the location of this minimum is very close to our lower bound for Sx_4, we extended it from 0.5 to 0.25 for the last 2 iterations of the neighborhood algorithm.

Figures 2.6c and 2.6d show the results of attempting the same inversion by only using 2 control polygons instead of 4 alongside vertical scaling to fit the synthetic observation. Again, the height and upper part of the head as well as the thickness of the diapir neck are well constrained. Most low-misfit geometries have a kink at 7 km depth which is the result of fitting both the shape of the head and width of the neck with only 2 control polygons. Furthermore, none of the low-misfit models have the correct width of the diapir base.

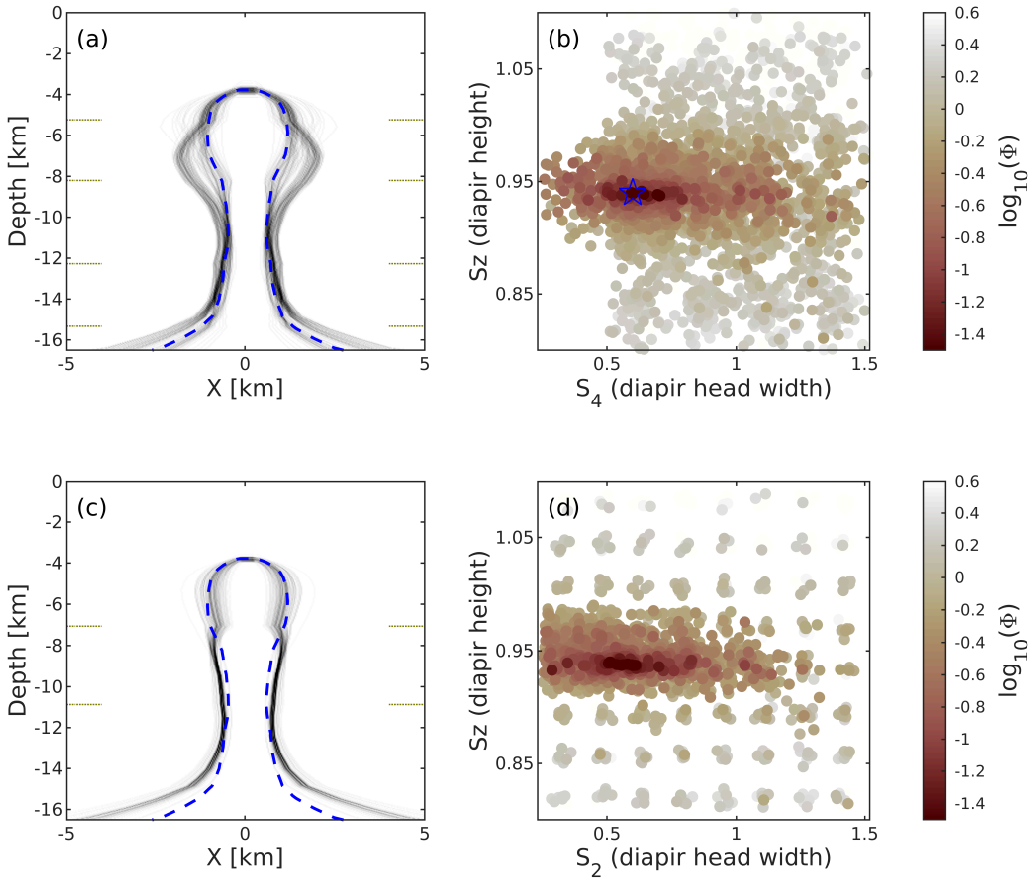

FIGURE 2.6: (a) Synthetic diapir in dashed blue (solid blue in Figure 2.3) and the 200 variations out of 3100 with the smallest misfit in gray. Dots on the sides indicate locations of the 4 control polygons. (b) Misfit ($\log_{10}(\Phi)$) as a function of width of the diapir head (S_4) and height of the diapir (Sz). Note the denser distribution of samples around the minimum courtesy of the neighborhood algorithm. Blue star indicates the location of the synthetic 'true' geometry (dashed blue in 2.6a). Figure 2.G.9 shows misfit as a function of all parameter combinations. (c) Similarly to 2.6a, Top 200 out of 2100 variations, using 2 control polygons. (d) Misfit as function of diapir height and head width for the 2 control polygon example.

2.4.2 Application II: Subduction

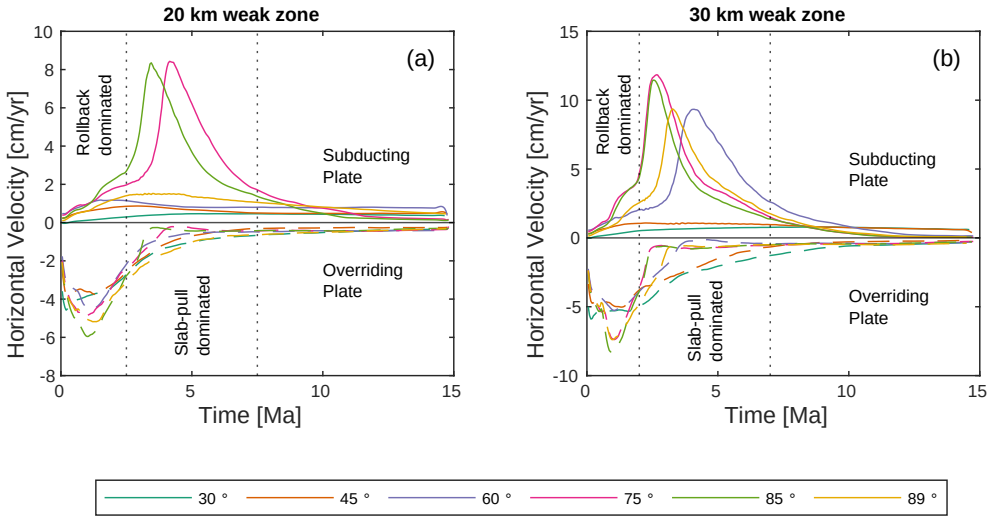

FIGURE 2.7: Average velocity of subducting (solid lines in upper panel) and overriding plate (dashed lines in lower panel) in dependence of time for a selection of different initial slab angles (β_0). Dotted vertical lines indicate periods dominated by different mechanisms. Within the first 2.5 Myr, the convergence is mostly accommodated by slab rollback and trench retreat. In the following 5 Myr, it is dominated by the trenchward motion of the subducting plate. (a) Models have a weak zone that is 20 km wide (about 4 grid cells). (b) Models have a weak zone 30 km wide (about 6 grid cells).

All subduction models start out with an initial stage of slab rollback, trench retreat and continent extension while the slab starts sinking. Over time, the horizontal velocity of the suducting plate increases depending on the angle of the slab (Figure 2.7). Models that start with a steep subduction angle ($\beta_0 > 65°$) eventually reach a stage where velocities increase strongly and the trench reverses direction and starts to advance towards the continent, leading to shortening of the fore-arc. Once the slab approaches the bottom of the model, velocities decrease again. This also stops the advance of the trench, leading to another rollback period.

2.4.2.1 Convergence velocity

In Figure 2.8a, we show the difference between the average horizontal velocities of subducting and overriding plate (i.e. the convergence velocity) as a function of time and initial subduction angle β_0. Within the first 2 Myr, all models undergo a period of convergence with maximum velocities of 4 $\mathrm{cm\,yr^{-1}}$ for low β_0 and 7 $\mathrm{cm\,yr^{-1}}$ for high β_0. In this period, the convergence velocity is mainly caused by the retreat of the trench (see also Figure 2.7). For $\beta_0 <= 65°$, the convergence rate then slowly declines over time. However, models that start with a steeper slab go through a second period of rapid acceleration after about 4 Myr, reaching up to 9 $\mathrm{cm\,yr^{-1}}$ at $\beta_0 = 80°$ before declining as well. In this period, the velocity of the subducting plate is the main contributor to the convergence velocity (Figure 2.7). While velocities generally increase with β_0, they drastically decrease again at $\beta_0 > 85°$ as we approach a vertical initial slab. Supplementary text 2.F presents an example of how a velocity profile (e.g., Sdrolias and Müller, 2006) can be used to invert for the initial subduction angle β_0 similar to section 2.4.1.2.

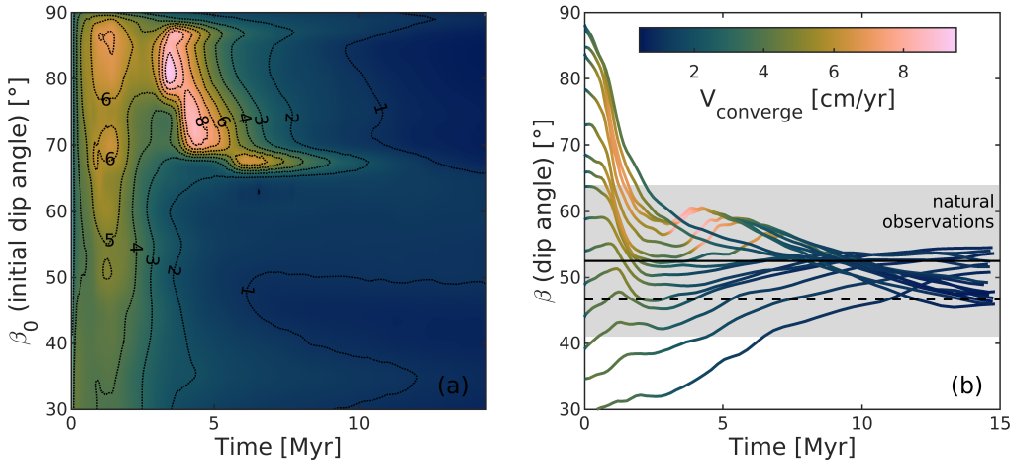

FIGURE 2.8: (a) Convergence rate between oceanic and continental plate in dependence of initial subduction angle (β_0) through time. (b) Dip angle of the subducting slab (β) as a function of time for all models. Color gradient along the curves shows convergence velocity. Solid black line shows global average of dip angles from Lallemand et al. (2005) and shaded gray area indicates one standard deviation. Dashed black line shows global average of dip angles from Syracuse and Abers (2006).

Models with a wider weak zone (30 km instead of 20 km) show the same general behavior, but the velocity of both plates is higher. There are also more models that enter the second phase of acceleration (Figure 2.7).

2.4.2.2 Subduction angle

Figure 2.8b shows the evolution of the dip angle for all models. While slabs that start out with a shallow dip angle gradually steepen over time, slabs that start steep quickly undergo flattening until leveling out at about 60°. Models that undergo a second phase of acceleration (see Figure 2.8a) slightly steepen from 55° to 65° during that period again. Once the slabs start approaching the bottom of the model (660 km depth), they flatten towards 45°. All models converge to a dip angle between 45° and 55° which is agreement with global averages as reported by Lallemand et al. (2005) and Syracuse and Abers (2006).

2.5 Discussion

2.5.1 Parameterization and transformation

The method we present in this study is based on two main concepts. The use of a reference geometry (sphere in section 2.2.2 and Figure 2.1, red plate in section 2.2.3 and Figure 2.2, red outline in section 2.3.1 and Figure 2.3, $\beta_0 = 60°$ model in section 2.3.2) and control polygons/rotation centers that act as anchors for the transformation.

2.5.1.1 Strengths and weaknesses

Using a reference geometry removes the necessity to define a large number of coordinates for every new variation. Instead, each complex shape is represented by a small number of values that describe how it is different to the reference geometry. This

comes at the price of limiting the shape of possible variations. It would for instance not be possible to make the diapir in Figure 2.3 lean towards one side, introduce any asymmetry (in the x-y-plane) that was not present before or split the head in two without creating a new reference model with those features. But since the initial geometry of geodynamic models is commonly constrained by imaging surveys, there usually is enough information to create an appropriate reference model of the geological unit (Figure 2.3).

The use of control polygons and interpolation between them allows us to greatly reduce the number of necessary parameters compared to providing scaling parameters for each polygon or changing individual coordinates/vertices. Homogeneous three-dimensional scaling of the body is possible with a single control polygon and parameter ($Sx = Sy = Sz$). At the same time, complex changes as shown in Figure 2.1 can be achieved with only 6 or 7 parameters. Free choice of the position of the control polygons allows for great flexibility. The closer control polygons are to another, the shorter the wavelength of variation. If a part of the geological unit is well constrained, this part can be kept locked by bounding it with two control polygons with constant scaling parameters of 1, while the other parts can stay variable. As mentioned before, our transformations cannot introduce additional complexity into the individual polygons.

Figure 2.6c illustrates that using a smaller number of control polygons (2 instead of 4) can be sufficient to fit the most influential features of the diapir. But it also demonstrates a potential pitfall of using few control polygons. Because the observation (fault system) is sensitive to the neck width but not the base width (Figures 2.6a and 2.G.7) but both features are governed by the same control polygon, the base of the diapir appears to be well constrained but is actually wrong (Figure 2.6c). It is important to keep in mind that each control polygon should only govern one feature of a body.

2.5.1.2 Relation to other approaches

Our approach shares similarities with that of (Sevilla et al., 2020) which also applies 2D transformations at different levels of the third dimension that control how the entire 3D shape is transformed. Both methods seem capable of producing similar transformations with the same number of parameters but we consider the scaling parameters to be more intuitive than the control points of NURBS surfaces.

There is also similarity to the work of (Galley et al., 2020) as groups of surface nodes are moved together to preserve smooth surfaces while other groups of nodes remain stationary. In the case of the diapir (Figure 2.3) we can change height and width at 4 levels with only 5 parameters whereas moving a single surface vertex in 2D already requires 2 parameters. The approach of (Galley et al., 2020) does in turn provide more flexibility to introduce asymmetric features.

Our adaptation for subduction zones shares the philosophy of using a combination of arbitrary coordinates (provided by the Inkscape drawing) and features that are specific to subduction zones like dip angle and plate thickness with the GWB (Fraters et al., 2019). The main difference is the use of a reference geometry which means that weak zone, crust and flattening/steepening segments can be added with one or two parameters each instead of building the plate out of individual segments each requiring 3 or more parameters. By not relying on a reference geometry, the GWB has advantages in quickly introducing big geometry changes.

2.5.2 Importance of initial geometry

Both applications (more details in the following sections) demonstrate that different initial geometries within the range of uncertainty of geophysical imaging can lead to drastically different modeling results. Therefore, it is crucial to test different setups and develop an understanding of the influence that the geometry of the geological structures can have. While this finding is not necessarily new as previous studies have highlighted the dependence of results on initial geometry (e.g., Le Pourhiet et al., 2003; Duretz et al., 2020), the issue often remains unaddressed in many state-of-the-art geodynamic studies (see section 2.1) that use a single geometry or a handful of end-member cases without parameterization (e.g., Liao et al., 2017; Tetreault and Buiter, 2012).

Our approach enables the user to quickly, on the order of a second per version, and automatically create any number of variations of a complex 3D body in their model. This not only allows for the incorporation of uncertain constraints but can also reveal unexpected dependencies of the model results on the initial geometry of the model. The scaling parameters even facilitate a quantitative description of such dependencies.

2.5.3 Application to salt

Figure 2.4 shows how different initial salt geometries result in distinctly different faults. We observe some intuitive relationships like the link between height of the diapir and position or aspect ratio of the fault (Figure 2.5a,b). But, we also find unexpected correlations like a thin diapir neck facilitating faults at the sides of the diapir (Figure 2.5c). We also learn that the base of the diapir (S_1) and the transition from head to neck (S_3) have little to no impact on the developing faults and could therefore be kept constant in further investigations of the system.

It is apparent that faults can develop to both sides of the diapir independently of the geometry for the symmetric case. For the asymmetric case, faults that develop at the side of the diapir head exclusively appear on the side that has a stronger curvature (Figure 2.G.8c,f). We tested the asymmetry on both sides to exclude the possibility that this effect is caused by our grid discretization.

Finally, we can see that, given the observation of a fault and a good understanding of the material parameters, geodynamic modeling could help improve imaging results and reduce ambiguity regarding the extent of a diapir. Figure 2.6 shows that it is in principle possible to constrain the height and head width of the diapir with the help of an observed fault while deeper structures that have no influence of the faulting pattern remain blurred. Applying this to a natural example would involve more unknowns like the material parameters of salt and crust, additional crustal layers, heterogeneities in the salt and topography, resulting in a larger parameter space to consider. However, geometry, parameterized by scaling parameters, can be included in such a study (Spang et al., 2021).

2.5.4 Application to subduction

Figures 2.7 and 2.8a show how strongly the velocity of plates and the entire dynamics of the model depend on the initial angle of the subducting slab. While models with an initial angle $\beta_0 <= 65°$ move at relatively even velocities throughout 15 Myr, models with steeper slabs run through a period of strongly increasing velocities that are high enough to stop or even reverse the retreat of the trench. The timing and maximum velocity of this phase of acceleration also depend on the initial geometry of the model.

Another geometrical parameter that strongly influences the velocities of the plates is the thickness of the weak zone between subducting and overriding plate (Figure 2.7). With a thicker weak zone, there is less friction between the plates and they reach higher velocities. So, both parameters (initial dip angle of the slab and thickness of the weak zone) can exert a first order control on the model dynamics and could overprint a lot of other effects. With our method, it is easy to change either parameter and investigate their influence on the model results without investing a lot of time into creating different initial geometries.

Figure 2.8b shows that independently from the initial subduction angle (β_0), all models converge to a similar angle of about 50° after a few Myr. This range is in agreement with global averages of subucting slabs (Lallemand et al., 2005; Syracuse and Abers, 2006) which suggests that 50° is the preferred angle for long-term slab-pull-dominated subduction.

2.6 Conclusions

In this study, we present a simple and intuitive method to describe and manipulate 3D bodies in a heterogeneous manner with a limited set of parameters. This not only allows us to include uncertainties about initial geometry in the modeling process, but also enables us to quantify the relationship between initial geometry of a model and the computed output. As shown by our study and Spang et al. (2021), this allows us to even improve constraints on geometry by integrating different observations and invert for geometric properties.

We present two application examples. (i) A salt diapir with an ambiguous geometry in seismic imaging. We show that slight geometric variations that would all satisfy the imaging data, can result in the development of vastly different faulting patterns in an extending regime. It is also evident that small asymmetries in the diapir lead to distinctive differences in the developing faults around the diapir. Furthermore, we show that, with our parameterization, initial geometry can be treated like any material parameter and included in sensitivity studies or inversion frameworks. (ii) A subduction zone where we vary the initial dip angle of the subducting slab as well as the thickness of the weak zone between subducting and overriding plate. Both parameters influence the velocity evolution of the plates by an order of magnitude. We show that, independently of the initial dip angle, all slabs approach a subduction angle of about 50°.

Our study presents an intuitive method to parameterize and manipulate the initial geometry of geodynamic models and highlights the importance of considering different geometries instead of using just one. We implemented the method as a tool in the open-source software package geomIO which is fully compatible with the open-source, thermomechanical stokes code LaMEM. Areas of application include salt tectonics, subduction settings, volcanic systems with varying sizes/shapes of magma bodies and models of orogenesis with uncertain extents of critical units. As geomIO can forward model Bouguer anomalies, constraints from gravity surveys can directly be considered in the creation of the initial geometry of geodynamic models.

2.7 Acknowledgments

The authors thank John Naliboff, Florian Wellmann and one anonymous reviewer for their help in improving the quality of the manuscript. This study was funded by the European Research Council through the MAGMA project, ERC Consolidator Grant #

771143. We used perceptually uniform colormaps to prevent optical data distortion (Crameri, 2018). Parts of this research were conducted using the supercomputer Mogon II and/or advisory services offered by Johannes Gutenberg University Mainz (hpc.uni-mainz.de), which is a member of the AHRP (Alliance for High Performance Computing in Rhineland Palatinate, www.ahrp.info) and the Gauss Alliance e.V..

Supplementary

2.A Open research section

Software used for this research is available on zenodo at: https://doi.org/10.5281/zenodo.6538270 (Kaus et al., 2016; Bauville and Baumann, 2019)

2.B General workflow

This text outlines the general workflow of how our tool can be used for a geodynamic study. It contains 7 steps (illustrated in Figure 2.G.1), of which the last 4 may repeat if an inversion is to be performed. Steps 1-4, 6 and 7 can be completed on any modern computer or laptop that has access to Inkscape, Matlab and Paraview (for visualization only). Step 5 requires LaMEM and more computing power. Single 2D simulations can be performed on regular machines but for 3D or a large number of 2D simulations, a computing cluster is necessary.

(i) Draw the reference geometry in Inkscape. This includes all units like the background lithosphere, mantle and anomalous bodies like salt and magma bodies or subducting plates. Instructions can be found at: https://bitbucket.org/geomio/geomio/wiki/Home. This results in an .svg file.

(ii) Use the basic functionality of geomIO to read the .svg file and create the reference geometry. This results in a .vtk file for each unit. The different units can be visualized directly in Matlab. Alternatively, the .vtk files can be opened in Paraview.

(iii) Choose the unit that should be varied and the control polygons. Prepare and load in scaling parameters for each variation or use the build-in options to generate them.

(iv) Use the new functionality of geomIO and the options selected in step (iii) to create an ensemble of setups. Figure 2.G.2 shows examples of how this can be accomplished. For a more detailed description of all available options visit https://bitbucket.org/geomio/geomio/wiki/VaryGeomTutorial.md.

(v) Use LaMEM to run forward models with each of the setups generated in step (iv).

(vi) Use any software to post-process the results from LaMEM (e.g., compute a misfit to observations, analyze result dependencies on input parameters). LaMEM output is in .vtk format, so it can be directly visualized in Paraview, or read and reformatted in Python or Julia.

(vii) Optional: Select new scaling parameters and return to step (iv). New scaling parameters can be the result of an optimization algorithm (e.g., neighborhood algorithm (Sambridge, 1999a), NAplus (Baumann et al., 2014)).

To reproduce the results (including Figures) of this study, visit our repository on zenodo (https://doi.org/10.5281/zenodo.6538270). It contains the versions of geomIO and LaMEM that were utilized as well as detailed step-by-step instructions of how to reproduce our results. As LaMEM requires more computing power, we also included the post-processed output in the repository.

2.C Additional options

2.C.1 Absolute transformation parameters

One issue of the method described in section 2.2.1.3 is that the absolute change in coordinates of polygon nodes is determined by the size of the polygon. In Figure 2.G.3b, the central polygon (lowermost control polygon) is elongated by 0.5 units in y-direction while the lowermost polygon is only elongated by 0.015 units. If this effect is not desired, we offer a second transformation algorithm which works with absolute transformation parameters (dx and dy). dx and dy are the maximum transformations per direction and they are scaled for every node on the polygon, depending on the node's position:

$$\begin{pmatrix} \vec{x}_{new} & \vec{y}_{new} \end{pmatrix} = \begin{pmatrix} \vec{x} & \vec{y} \end{pmatrix} + \begin{pmatrix} \frac{\vec{x}'}{|\overrightarrow{xy}|} & \frac{\vec{y}'}{|\overrightarrow{xy}|} \end{pmatrix} * \begin{pmatrix} dx & 0 \\ 0 & dy \end{pmatrix} \tag{2.5}$$

$$|\overrightarrow{xy}|_n = \sqrt{{x'_n}^2 + {y'_n}^2} \tag{2.6}$$

The fraction in equation 2.5 corresponds to element-wise division. The lower half of the body in Figure 2.G.3c was changed with absolute transformation parameters. While the central polygon (lowermost control polygon) is identical to the one in Figure 2.G.3b, all polygons below are wider, most notably the lowest one. Figure 2.G.4a shows how the different methods affect the lowermost polygon. The approach of absolute transformation is limited when it comes to shrinking parts of the body which have very small polygons.

2.C.2 Coordinate rotation

The body might have a preferred orientation which is not aligned with either the x- or the y-direction, so scaling it in a different direction might be desirable. To do that, we include the option to rotate the coordinate system such that the orientation, in which transformation is preferred, aligns with one of the axes. This is done by defining the rotation matrix

$$Q = \begin{pmatrix} cos(\theta) & sin(\theta) \\ -sin(\theta) & cos(\theta) \end{pmatrix} \tag{2.7}$$

where θ represents the preferred direction of transformation and rotates the coordinate system clockwise. To apply it, equation 2.3 has to be modified to:

$$\begin{pmatrix} \vec{x}_{i,new} & \vec{y}_{i,new} \end{pmatrix} = \begin{pmatrix} \vec{x_i}' & \vec{y_i}' \end{pmatrix} * Q * \begin{pmatrix} Sx_1 & 0 \\ 0 & Sy_1 \end{pmatrix} * Q^T + \begin{pmatrix} x_{i_c} & y_{i_c} \\ ... & \\ x_{i_c} & y_{i_c} \end{pmatrix} \tag{2.8}$$

Figure 2.G.4b shows an example case where a polygon is elongated in NNE-SSW direction, so without rotating the coordinate system it would not be possible to only transform the polygon along its longest axis. However, by rotating the y-axis to align with the orientation, then applying the scaling and rotating it back, we can do that. Figure 2.G.4c shows that more complex shapes can be handled in the same way.

2.D Model details

2.D.1 LaMEM

For our models, we utilize the thermomechanical finite differences code LaMEM (Kaus et al., 2016). It solves for the conservation of momentum, mass and energy (eq. 2.9-2.11), using a staggered grid in combination with a marker-in-cell approach (Harlow and Welch, 1965).

$$\frac{\partial \tau_{ij}}{\partial x_j} - \frac{\partial p}{\partial x_i} + \rho g_i = 0 \tag{2.9}$$

$$\frac{1}{K}\frac{Dp}{Dt} - \alpha\frac{DT}{Dt} + \frac{\partial v_i}{\partial x_i} = 0 \tag{2.10}$$

$$\rho C_p \frac{DT}{Dt} = \frac{\partial}{\partial x_i}\left(\lambda \frac{\partial T}{\partial x_i}\right) \tag{2.11}$$

τ_{ij} is the Cauchy stress deviator, $x_i (i = 1, 2, 3)$ denotes the Cartesian coordinates, p is pressure (positive in compression), ρ density, g_i gravitational acceleration, K the bulk modulus, α the thermal expansion coefficient, T the temperature, v_i the velocity vector, C_p the specific heat capacity, λ the thermal conductivity and D/Dt is the material time derivative.

The rocks are characterized by a visco-elasto-plastic rheology where the strain rate is the sum of the elastic, viscous and plastic components:

$$\dot{\epsilon}_{ij} = \dot{\epsilon}^{el}_{ij} + \dot{\epsilon}^{vi}_{ij} + \dot{\epsilon}^{pl}_{ij} \tag{2.12}$$

$\dot{\epsilon}_{ij}$ denotes the total deviatoric strain rate tensor, while $\dot{\epsilon}^{el}_{ij}$, $\dot{\epsilon}^{vi}_{ij}$ and $\dot{\epsilon}^{pl}_{ij}$ represent the elastic, viscous and plastic strain rate components. For a detailed discussion of this equation and all of its components, the reader is referred to Kaus et al. (2016). Here we will focus on the material parameters which impact the 3 components.

The elastic component depends on the shear modulus G:

$$\dot{\epsilon}^{el}_{ij} = \frac{1}{2G}\frac{D\tau_{ij}}{Dt}, \tag{2.13}$$

where $D\tau_{ij}/Dt$ is the objective derivative of the stress tensor.

The viscous component depends on the viscosity η:

$$\dot{\epsilon}^{vi}_{ij} = \frac{\tau_{ij}}{2\eta} \tag{2.14}$$

η is either a constant (see tables 2.G.1 and 2.G.2) or follows the stress- and temperature-dependent powerlaw relationship of dislocation creep:

$$\eta = \frac{1}{2}(B_n)^{-\frac{1}{n}}(\dot{\epsilon}_{II})^{\frac{1}{n}-1}\exp\left(\frac{E_n + pV_n}{nRT}\right), \tag{2.15}$$

where B_n is the creep constant, $\dot{\epsilon}_{II}$ the square root of the second invariant of the strain rate ($\dot{\epsilon}_{II} = (\frac{1}{2}\dot{\epsilon}_{ij}\dot{\epsilon}_{ij})^{1/2}$), E_n the activation energy, p the pressure, V_n the activation volume, n the powerlaw exponent, R the universal gas constant and T the temperature.

The plastic component is governed by the Drucker-Prager failure criterion (Drucker and Prager, 1952):

$$\tau_{II} \leq \sin(\phi)p + \cos(\phi)c_0 \tag{2.16}$$

where τ_{II} is the square root of the second invariant of the stress tensor ($\tau_{II} = (\frac{1}{2}\tau_{ij}\tau_{ij})^{1/2}$), ϕ is the friction angle, p the pressure and c_0 the cohesion. As long as τ_{II} does not exceed the failure criterion, the stress is accommodated by visco-elastic deformation.

2.D.2 Model details application I: Salt

We model a homogeneous slice of crust that is 20 km wide and deep and hosts a 3.5 km thick salt bed from which the diapir rises. Along the boundaries of the model, we employ free slip conditions (velocities normal to boundaries equal zero). At the top of the crust, we use a stabilized (Kaus et al., 2010) stress free internal surface and 5 km thick layer of sticky air (Crameri et al., 2012). We use 128 cells in the horizontal and 256 cells in vertical direction. For simplicity, we use linear viscosities η for all materials. Table 2.G.1 summarizes the material parameters that we employed. A shear modulus of 15 GPa and a Poisson's ratio of 0.25 correspond to a Young's modulus of 37.5 GPa which is consistent with previous laboratory and modeling studies on salt (Ingraham et al., 2015; Zong et al., 2017; Baumann et al., 2018).

2.D.3 Model details application II: Subduction

Our subduction model is 2000 km wide and extends from the surface to 660 km depth. We use 512 cells in the horizontal and 256 cells in the vertical direction, yielding resolutions of about 4 and 2.5 km respectively. The 100 km thick continent is made up of 40 km of crust and 60 km of lithospheric mantle. We assign different linear temperature gradients to the continental crust and lithosphere and use a half-space cooling model for the subducting plate that corresponds to a thermal age of 30 Myr. As the plate has already started subducting at the start of our simulations, we add another 1 Myr of temperature diffusion to account for the heating during that initial stage of subduction (Figure 2.G.10a). All materials are described by a temperature- and stress-dependent visco-plastic rheology. Table 2.G.2 summarizes all material parameters. We use free slip boundary conditions along all model edges and do not prescribe any boundary velocities.

2.E Asymmetry

The asymmetry was introduced by slightly reducing the curvature of the diapir head on one side (Figure 2.3, 2.G.8). As for the symmetric case, we can see a clear distinction between faults that develop from the center of the diapir head and those that develop

from the side of the head (Figure 2.G.8a,d). But while central faults still develop to both sides, outside faults now exclusively develop on one side of the diapir (Figure 2.G.8c,f). Mirroring the asymmetry leads to a mirrored result. In all cases, outside faults now appear on the side that retained the original curvature.

This suggests that for symmetric cases, the side that develops the dominant fault is influenced by the small difference between how one side of the curved diapir boundary aligns with the grid cells compared to the other side. This is still the case for the central faults at asymmetric diapirs, but towards the outside of the diapir head, the asymmetry is more important for the location of the dominant fault.

2.F Inverting for initial angle

Reconstructions (e.g., Sdrolias and Müller, 2006) show that convergence velocities between plates fluctuate throughout the evolution of subduction zones. These fluctuations are frequently interpreted to be the result of subdcution of ocean plateaus or ridges (e.g., Martinod et al., 2010) but our models show that the convergence rate also fluctuates without any changes in the elevation or density structure of the oceanic plate. Instead the velocity profile seems to be coupled to the initial dip of the subducting slab (β_0), so given a good understanding of the rheology of the system, a velocity reconstruction could also be used to invert for an initial angle using modeling. To demonstrate the feasibility of this approach, we use a synthetic profile that we generated using $\beta_0 = 72.5°$ (dotted line in Figure 2.G.11a). We add normally distributed random noise ($\sigma = 0.5\,\mathrm{cm\,yr^{-1}}$) to the profile to get a synthetic observation in 1 Myr intervals (black circles in Figure 2.G.11a). We then run a set of models in 5° intervals (blue in Figure 2.G.11b), compute the RMS misfit (Φ) and add models in 1° intervals in areas of low misfit (orange in Figure 2.G.11b).

Figure 2.G.11b shows that we can find the true β_0 with only a few forward models. In a real application, there might be more parameters involved in the inversion process but as there is an obvious dependency of the velocity profile on the initial angle, an inversion with more models should still converge to the correct solution.

2.G Supplementary tables and figures

Table 2.G.1: Material parameters for salt application

Material	$\rho\,[\frac{\mathrm{kg}}{\mathrm{m}^3}]$	G [GPa]	ν[ ]	η [Pas]	c_0[MPa]	ϕ[°]
Crust	2700	30	0.25	10^{24}	10	30
Salt	2200	15	0.25	10^{19}	10	30

Table 2.G.2: Material parameters for subduction application

Material	$\rho\,[\frac{\mathrm{kg}}{\mathrm{m}^3}]$	$B_n\,[\mathrm{MPa^{-n}\,s^{-1}}]$	E_n [kJ]	$V_n\,[\frac{\mathrm{cm}^3}{\mathrm{mol}}]$	n[ ]	c_0[MPa]	ϕ[°]
OP* Crust	2800	6.7 x 10^{-6}	156	0	2.4	10	30
OP* Lithosphere	3250	1.1 x 10^5	530	9.5	3.5	10	30
SP* Lithosphere	3300	1.1 x 10^5	530	9.5	3.5	10	30
Mantle	3300	1.1 x 10^5	530	9.5	3.5	10	30
Weak Zone	3250	$\eta = 10^{20}$ Pas				0.1	5

*OP corresponds to overriding and SP to subducting plate.

TABLE 2.G.3: Scaling parameter ranges

	S_1	S_2	S_3	S_4	Sz
min	0.5	0.5	0.5	0.5	0.8
max	2.0	3.0	2.0	1.5	1.1

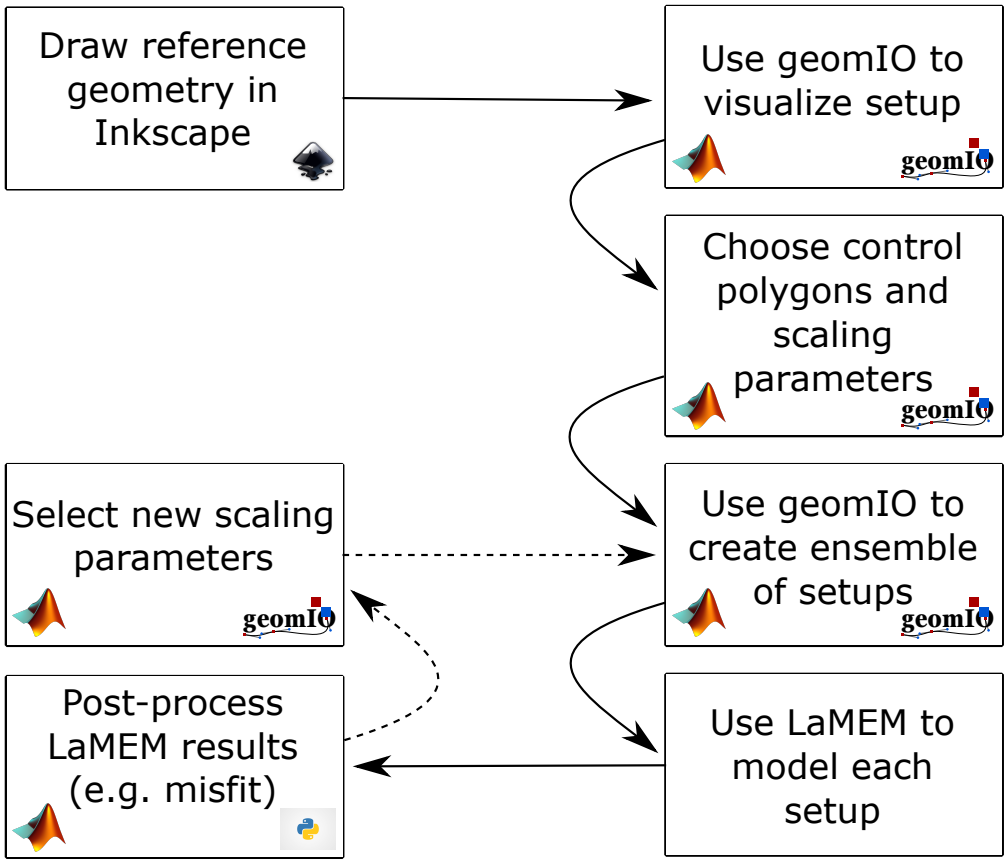

FIGURE 2.G.1: General workflow for using geomIO and the new tool presented in this work in combination with LaMEM. The dashed arrows indicate that these steps are optional and are only necessary to minimize misfit or explore additional parameter space. Text S1 describes the procedure in more detail.

(a)

```
% vary geom settings
opt.varyGeom.do             = true;                 % activate geometry variation
opt.varyGeom.volume         = 'Diapir';             % name of volume in Inkscape
opt.varyGeom.dim            = '2D_X';               % mode
opt.varyGeom.genType        = 'grid';               % how to generate scaling parameters
opt.varyGeom.Grid.lb        = [0.5; 0.5; 0.5; 0.5]; % lower bound for scaling parameter generation
opt.varyGeom.Grid.ub        = [2.0; 3.0; 2.0; 1.5]; % upper bound for scaling parameter generation
opt.varyGeom.Grid.num       = [2; 2; 2; 2];         % number of samples for each scaling parameter
opt.varyGeom.Grid.Sz        = [0.8; 1.1; 2];        % options for vertical scaling parameter generation
opt.varyGeom.Grid.noise     = 0.3;                  % noise to be added to scaling parameters
opt.varyGeom.stretchType    = 'factor';             % scale by factor or absolute value
opt.varyGeom.SzType         = 'bot';                % reference level for vertical stretching
opt.varyGeom.CtrlPoly       = [153, 253, 385, 482]; % indices of control polygons
opt.varyGeom.CP_ref         = 'global';             % reference system for control polygons
opt.varyGeom.CP_track       = true;                 % control polygons change depth with vertical scaling
opt.varyGeom.outName        = './SaltExample';      % output name
opt.varyGeom.outNameOffset  = 0;                    % offset numbering of output
opt.varyGeom.writeParaview  = false;                % write .vtk files
opt.varyGeom.writePolygons  = true;                 % write LaMEM polygons
opt.varyGeom.drawOutlines   = true;                 % draw outline along profile
opt.varyGeom.outlineProf    = [0, 0];               % coordinates of outline profile
```

(b)

```
% vary subduction settings
opt.varySub.do           = true;          % activate subduction variation
opt.varySub.vols         = 'SimpleSlab'; % name of volume in Inkscape
opt.varySub.ref          = 'trench';      % reference system of rotation center coordinates
opt.varySub.xRot         = [0, 120];      % rotation center coordinates
opt.varySub.theta        = [10, -20];     % angles of rotation
opt.varySub.tolZ         = 1;             % tolerance when identifying the plate
opt.varySub.drawOutlines = true;          % draw outline along profile
opt.varySub.outlineProf  = [0, 0];        % coordinates of outline profile

% options to add layers
opt.varySub.addWZ        = true;          % add a weak zone
opt.varySub.d_WZ         = 20;            % thickness of weak zone
opt.varySub.ID_WZ        = 4;             % LaMEM ID
opt.varySub.type_WZ      = 0;             % LaMEM marker type
opt.varySub.d_Lith       = 100;           % thickness of overriding plate

opt.varySub.addCrust     = true;          % add crust
opt.varySub.d_OC         = 10;            % thickness of crust
opt.varySub.ID_OC        = 5;             % LaMEM ID
opt.varySub.type_OC      = 0;             % LaMEM marker type
```

FIGURE 2.G.2: Code snippet examples that show the options that are set in geomIO to create the geometry variations. (a) Salt diapir example. (b) Subduction example. Full codes used in this study are available on zenodo (https://doi.org/10.5281/zenodo.6538270).

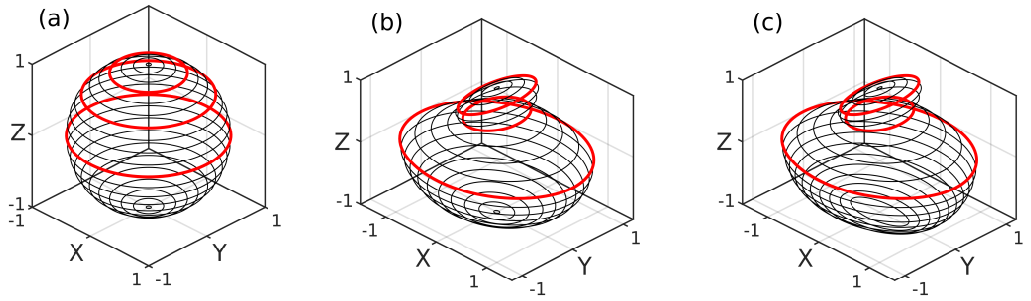

FIGURE 2.G.3: Illustration of 3-dimensional bodies as sets of 2-dimensional polygons. The three red polygons are the control polygons which are used to transform the body. (a) Sphere with radius 1, represented as 21 polygons. (b) Sphere from 2.G.3a after transformation by scaling. (c) Sphere from 2.G.3a with the upper half being transformed by scaling and the lower half by absolute transformation parameters. Note how the lower half is wider in 2.G.3c than in 2.G.3b.

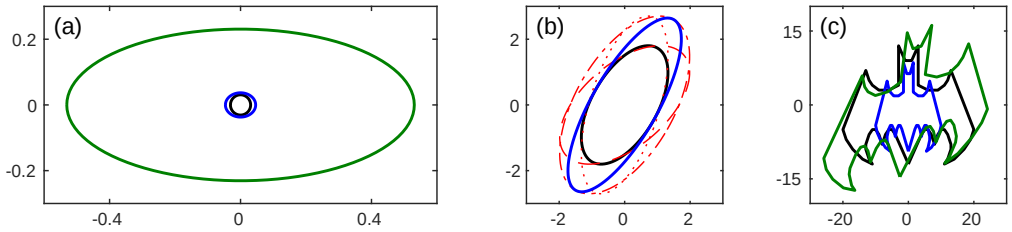

FIGURE 2.G.4: Illustration of how the transformation methods work on single 2-dimensional polygons. (a) Example of how the different transformation methods affect the lowermost polygon in Figure 2.G.3. Original in black, scaling in blue (used for Figure 2.G.3b) and transformation by absolute values in green (used for Figure 2.G.3c). (b) Scaling a polygon with preferred orientation. Original in black, dashed red line: Sx = 1.5, dotted red line: Sy = 1.5, dashed and dotted red line: Sx = Sy = 1.5, blue line: Sy = 1.5 and $\theta = 30$. (c) Illustration of how complex shapes are handled. Original in black, scaled version in blue (Sx = 0.5, Sy = 0.75), scaling and coordinate system rotation in green (Sy = 1.5, $\theta = 45$).

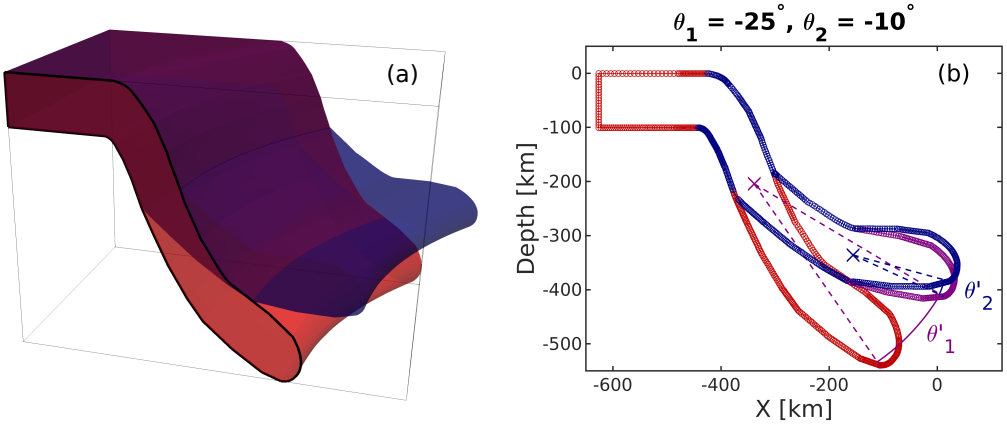

FIGURE 2.G.5: (a) 3D Example of a plate, subducting along a curved trench, drawn in geomIO (red) and an automatically generated variation that is bent at two locations in 200 and 320 km depth (crosses in 2.G.5b). Black line shows one of the vertical polygons that the 3D volume is represented as inside our algorithm and is identical to the red polygon in 2.G.5b. (b) Representation of the plates in 2.G.5a as vertical polygons. Red: original, purple: after the first rotation, blue: after both rotations. Crosses show the centers of rotation.

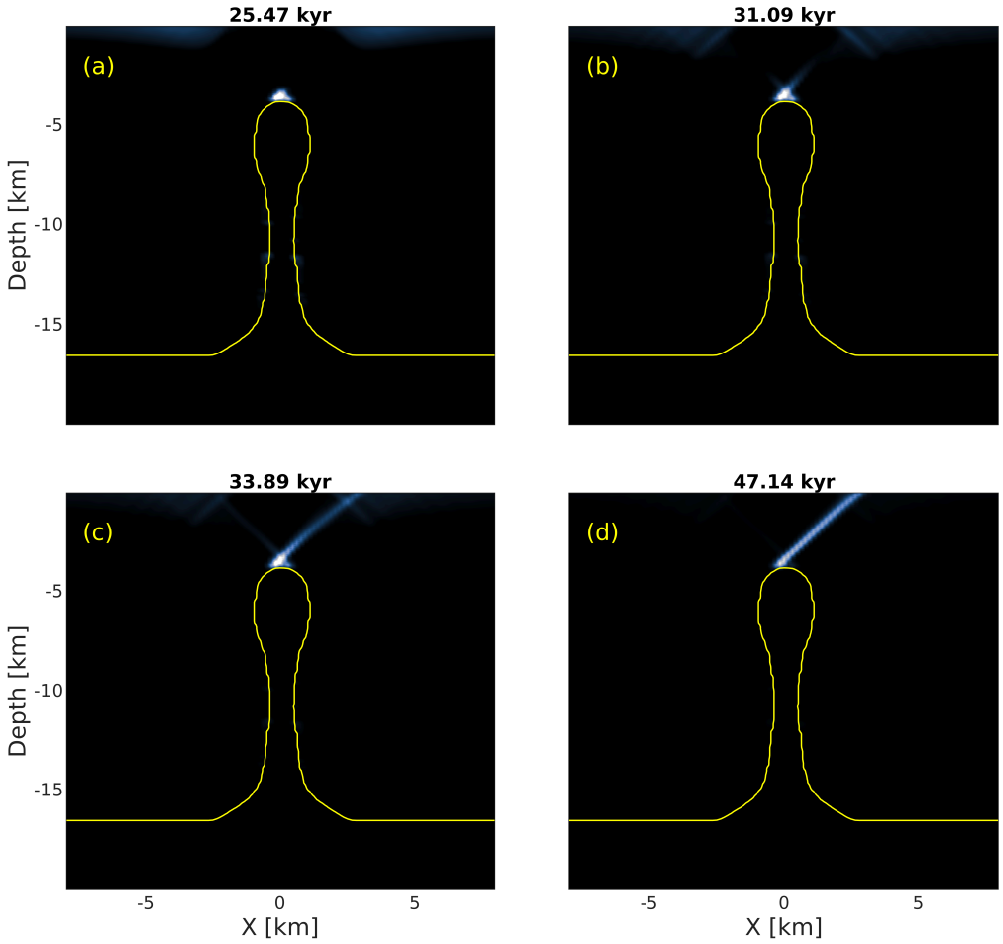

FIGURE 2.G.6: Evolution of plastic strain (i.e. faults) around the synthetic 'true' diapir (blue in Figure 2.3). (a) Early stage plastic failure along the surface and at the tip of the diapir. (b) First faults start to connect diapir and surface. (c) Faults have connected diapir and surface. Right fault takes up most of the deformation. (d) Right fault takes up all the deformation and left fault is no longer active.

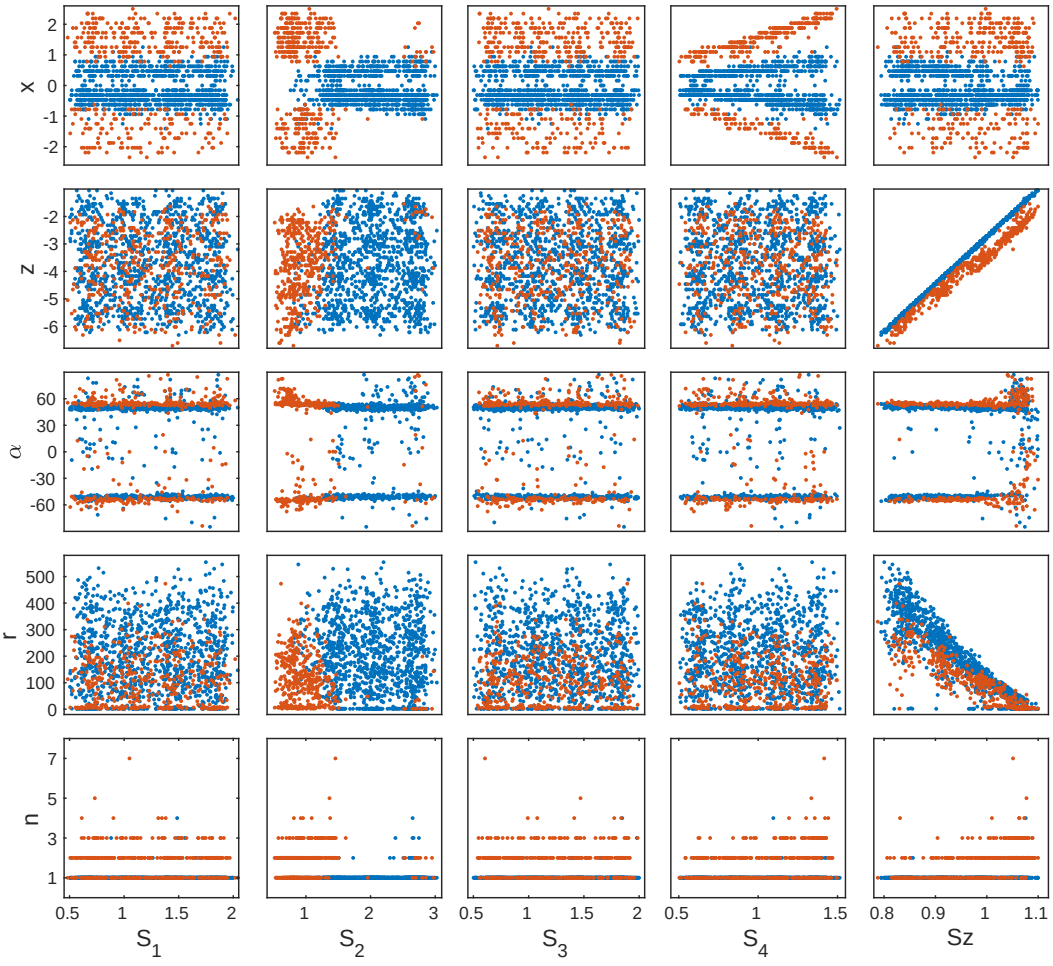

FIGURE 2.G.7: All fault properties in relation to each scaling parameter. x: lateral coordinate of lower fault tip, z: vertical coordinate of lower fault tip, α: dip angle of fault, r: aspect ratio of fault, n: number of faults. Blue dots denote faults that connect to the center and orange dots denote faults that connect to the side of the diapir head. Note that the orange dots are plotted on top which is why they hide a lot of blue dots in the lowest row of sub-figures.

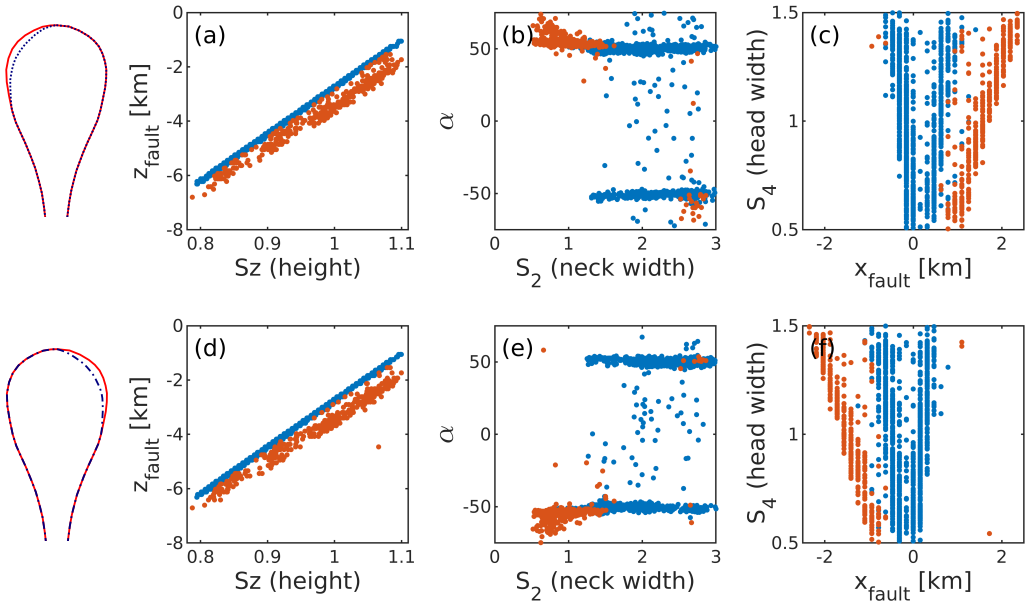

FIGURE 2.G.8: Results for two mirrored asymmetric setups. Upper row has been changed on the left (dotted in Figure 2.3), lower row on the right (dashed-dotted in Figure 2.3). Same color code as in Figure 2.5 (blue dots denote faults that developed from the center of the diapir head and orange dots denote faults that developed from it's sides). (a) and (d) Depth of the lower end of the fault in dependence of Sz. (b) and (e) Fault orientation in dependence of S_2. $\alpha < 0$: fault goes to the left. (c) and (f) Lateral position of the lower end of the fault in dependence of S_4.

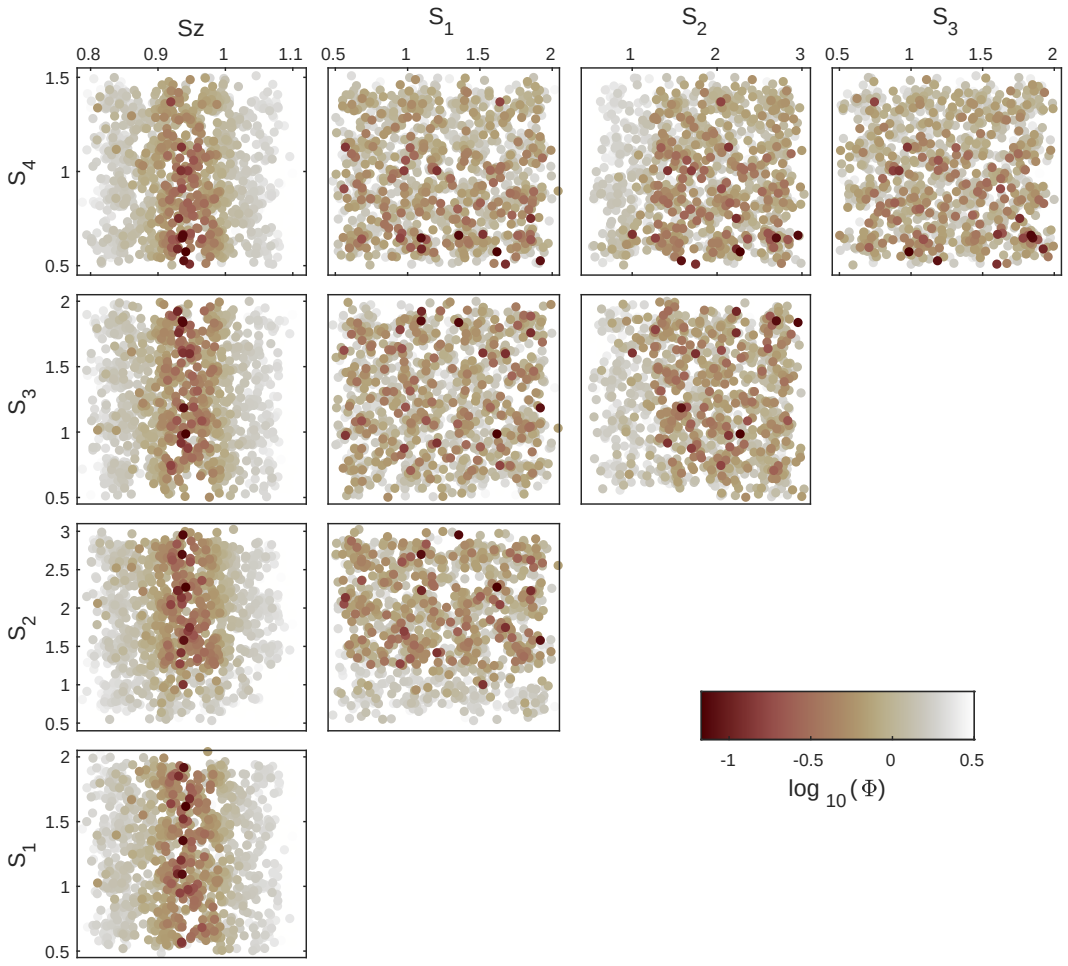

FIGURE 2.G.9: Misfit of the fault systems in dependence of all sets of 2 scaling parameters. Low misfit always correlates with medium Sz values and often correlates with low S_4. High misfit always correlates with low S_2. S_1 and S_3 do not show correlation with the misfit.

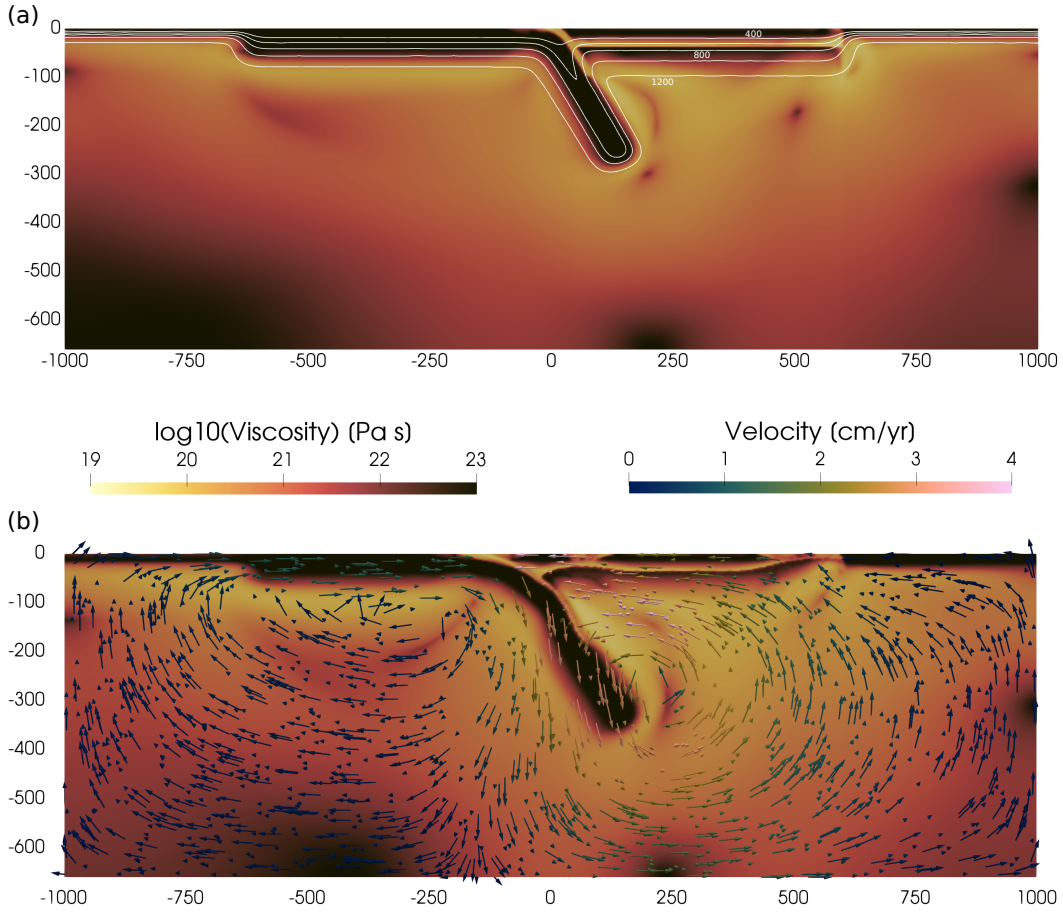

FIGURE 2.G.10: (a) Viscosity in the reference model ($\beta_0 = 60°$) at the first time step. White contour lines show temperature in 200 °C intervals. Top and bottom of the model have temperatures of 0 and 1350 °C respectively. Axes are in km. (b) Snapshot of the same model after 2 Myr. Slab has started to sink, trench has started retreating and continent has undergone buckling and extension. Arrows show velocity field.

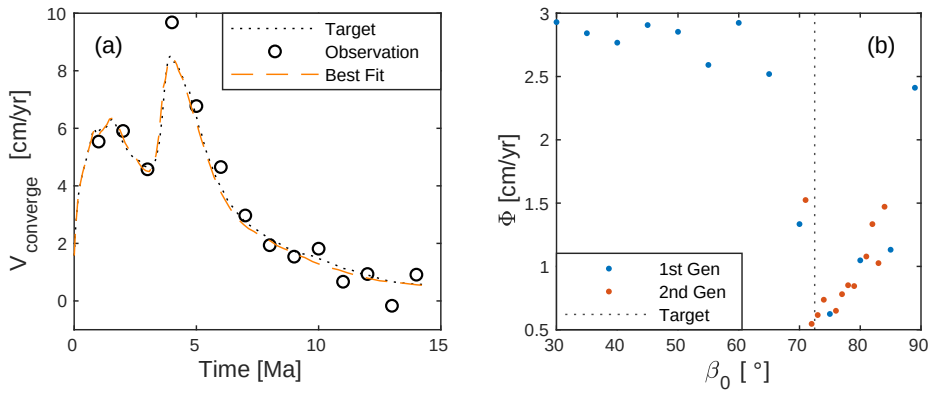

FIGURE 2.G.11: Results of inversion for initial angle (β_0). (a) Dotted black line shows profile of target model ($\beta_0 = 72.5°$) and black circles show noisy observation based on the target model. Dashed orange line shows best fitting model ($\beta_0 = 72°$). (b) RMS misfit (Φ) as a function of initial dip angle β_0. Blue dots shows first set of models in 5° intervals and orange dots show second set in 1° intervals in areas of low misfit. Dotted black line indicates β_0 of the target model.

Chapter 3

A multiphysics approach to constrain the dynamics of the Altiplano-Puna magmatic system

This chapter has been published in:
Spang, A., Baumann, T. S., & Kaus, B. J. P. (2021). A multiphysics approach to constrain the dynamics of the Altiplano-Puna magmatic system. *Journal of Geophysical Research: Solid Earth, 126*, e2021JB021725. https://doi.org/10.1029/2021JB021725

Abstract

Continuous Interferometric Synthetic Aperture Radar (InSAR) monitoring (> 25 years) has revealed a concentric surface deformation pattern above the Altiplano-Puna magma body (APMB) in the central Andes. Here, we use a joint interpretation of seismic imaging, gravity anomalies and InSAR data to constrain location, 3D geometry and density of the magma body. By combining gravity modeling, thermomechanical modeling, scaling law analysis and Bayesian inference, we are able to create a relationship between the geometry of a mid-crustal magma body and surface observations. Furthermore, we can estimate the uncertainties associated with the geometry of the APMB and identify the most important parameters that control the dynamics of the system. We constrain the density contrast between the APMB and the surrounding host rock to 90 - 130 $\mathrm{kg\,m^{-3}}$ (2σ) and the associated melt fraction to 15 - 22 %. Our visco-elasto-plastic 3D thermomechanical model reproduces the observed surface deformation self-consistently by buoyancy driven magma transport without the need for additional pressure sources. The flow pattern is controlled by a central rise at the top of the APMB whose geometry can be constrained with the help of InSAR observations while Bouguer anomalies constrain the deeper parts of the APMB. Automated scaling law analysis shows that the rheology of the upper crust and the magma mush as well as the density contrast between the two are the most important parameters in the system and need to be constrained for a better understanding of the subsurface processes.

Plain language summary

Volcanoes can have a big impact on economic infrastructure, the security of the population and the creation of ore deposits. They are fed and controlled by magmatic

systems in the crust beneath them and we currently have no techniques to directly observe these systems. In our study, we show how numerical (computer) models that obey the laws of physics allow us to compute the observations that we would make at the surface, given a certain set of physical and geometrical parameters. By automatically changing these parameters and comparing our modeling results to real surface observations, we can discover which parameter ranges and combinations are likely. This way, we can constrain location, size, geometry, density and melt content of the Altiplano-Puna magma body in the central Andes, using only surface observations. We are able to show that different surface observables are sensitive to different parts of the magmatic system which emphasizes the importance of including multiple data sets and modeling techniques in numerical studies.

3.1 Introduction

The existence of large scale partially molten regions in the crust where mantle derived melts can accumulate, differentiate, mix and assimilate to eventually ascend towards the surface or crystallize to build plutonic bodies is a widely accepted concept in geology. With the impact that volcanic eruptions can have on economic infrastructure (e.g., Ajtai et al., 2010) and the security of the population (e.g., Naranjo et al., 1986) as well as the importance of magmatic systems in the creation of ore deposits (e.g., Hedenquist and Lowenstern, 1994), the comprehension of such systems is highly relevant. Yet, due to our inability to directly observe the dynamics within magmatic systems or to recreate lab scale models with realistic pressure and temperature conditions, our understanding remains incomplete. Numerical models that obey the laws of physics can however go beyond the limits of observations or laboratory experiments and can shed light on previously unexplored processes. Instead they are limited by the availability and quality of data as well as the complexity of a system. Here, we want to demonstrate the advantages of using joint interpretations of different data sets and physically consistent thermomechanical models.

The Altiplano-Puna volcanic complex (APVC) (De Silva, 1989) and the associated Altiplano-Puna magma body (hereafter APMB) (Chmielowski et al., 1999) in the central Andes (Figure 3.1) are an excellent setting for such a study as the recent research project PLUTONS (`http://plutons.science.oregonstate.edu/`) has provided a lot of data to base a numerical model upon (Pritchard et al., 2018; Pritchard and Gregg, 2016). Large parts of the research area are located more than 3 km above sea level (asl) and host a chain of volcanoes related to the subduction of the Nazca plate beneath south America (Godoy et al., 2014). The eruption products are dominated by dacitic to andesitic lava flows and dacitic ignimbrites (e.g., De Silva, 1989; Godoy et al., 2014; Kay et al., 2010; Wörner et al., 2018).

Pritchard and Simons (2002) reported that they observed a 70 km wide, concentric uplift pattern centered around the dormant stratovolcano Uturuncu, using Interferometric synthetic-aperture radar (InSAR) data provided by the ESA. A decade later, Fialko and Pearse (2012) as well as Henderson and Pritchard (2013) identified a 150 km wide ring of subsidence surrounding the uplifting area and showed that the pattern had been stable since 1992. With the help of levelling and GNSS data, Gottsmann et al. (2018) argued that the uplift rate has even been constant since 1965. So far, a sizable number of studies have successfully attempted to reproduce the symmetric pattern with models of varying complexity and propose inflating magma bodies in depths ranging from 5 to 40 km below sea level. Pritchard and Simons (2004), Henderson and Pritchard (2013), Walter and Motagh (2014), Henderson and Pritchard (2017),

and Kukarina et al. (2017) use a purely elastic, Hickey et al. (2013) a linear-visco-elastic and Hickey and Gottsmann (2014) and Gottsmann et al. (2017) a temperature-dependent visco-elastic rheology. The most complex study of the area to date is a 3D model with an elastic upper crust overlying a temperature- and strain rate-dependent visco-elastic lower crust, including buoyancy effects (Fialko and Pearse, 2012). Similarly advanced models exist for other magmatic systems as well (e.g., Pearse and Fialko, 2010; Hickey et al., 2016).

One component missing from all previous studies is the consideration of plastic failure. Reuber et al. (2018) applied a model that includes plasticity and a complex initial geometry on top of the mechanics used by Fialko and Pearse (2012) to the Yellowstone magmatic system. We will use such a state-of-the-art thermomechanical code in combination with gravity modeling and a new way to parameterize complex 3D bodies to create a relationship between the geometry of a mid-crustal magma body and surface observations. Seismic imaging, Bouguer anomalies and InSAR data will help us constrain the geometrical and physical properties of the APMB as well as its dynamics.

3.2 Data and methods

We attempt to find a model geometry which is consistent with as many different observables as possible. For the location, shape, size and density of the APMB, we consider results from seismic imaging, Bouguer anomalies, InSAR as well as geochemical analysis of the eruption products of Uturuncu. To describe the background lithosphere, we consider seismic imaging and Bouguer anomalies as well as established density models of the area. All measures of depth in this study are in reference to sea level. In sections 3.2.1 to 3.2.3, we describe the data, used in this study while sections 3.2.4 to 3.2.6 focus on creating the model setup. Section 3.2.7 gives details on the thermomechanical code, we use to perform numerical modeling.

3.2.1 Imaging surveys

Imaging studies inferring the presence of magma in the central Andean crust date as far back as the 1980s (e.g., Schwarz et al., 1984; Breitkreuz and Zeil, 1984; Wigger, 1988). Starting with Chmielowski et al. (1999), a large number of studies have identified a layer, that they suggest to be the APMB or more generally a zone of partial melting. Chmielowski et al. (1999) and Zandt et al. (2003) interpreted the very low velocity zones ($V_s < 1.0$ km s^{-1}) in their shear wave models to be partially molten and thus conclude the APMB to be a sill like structure of less than 1 km thickness in about 15 km depth. The more recent study of Ward et al. (2014) combined receiver functions and ambient noise tomography to develop a V_s-model covering an area of about 400 x 400 km, extending to a depth of 50 km. The authors argue that any velocity lower than 2.9 km s^{-1} indicates the presence of melt and therefore suggest the APMB to extend from about 5 to 22 km depth. The concept of this shallow top of the partially molten zone is supported by the shallow brittle-ductile transition zone (BDTZ) around sea level, proposed by Jay et al. (2012). A magnetotellurics (MT) survey by Comeau et al. (2015) and Comeau et al. (2016) imaged a zone of low electrical resistivity (< 3 Ωm) starting at 14 km depth in the vicinity of Uturuncu and the authors acknowledge that their study does not allow for good estimates of the body's thickness. Most recently, McFarlin et al. (2018) presented a common conversion point stack of receiver functions, covering an area of about 100 x 100 km and imaged the top of the 9 km thick APMB at about 8 km depth. The V_p-model of Oncken et al. (2003) shows a

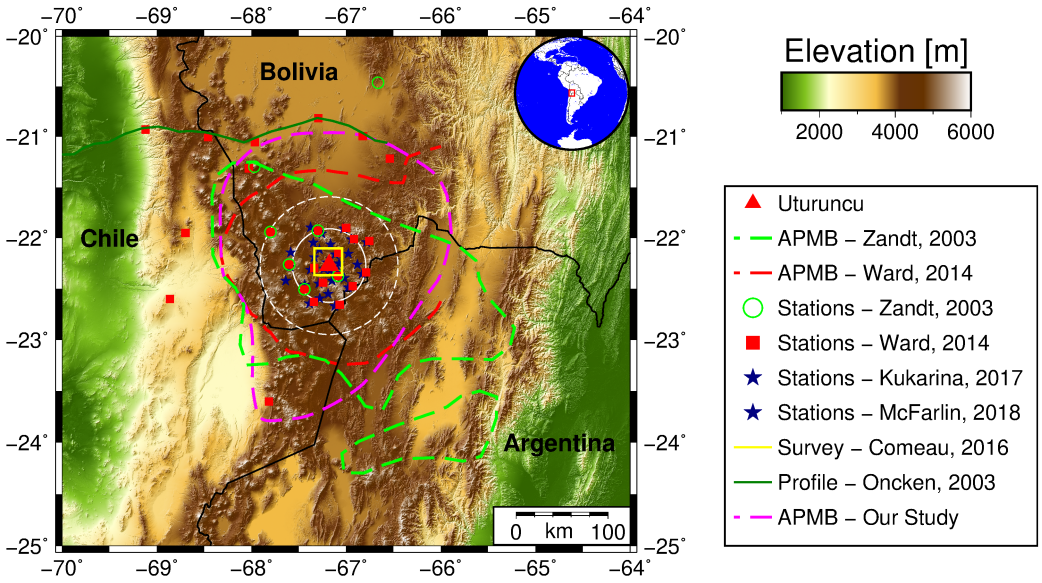

FIGURE 3.1: Topographic map of the study area, including seismic stations used in imaging studies. Green circles denote the stations used by Zandt et al. (2003) and Chmielowski et al. (1999) and the dashed green lines show the extent of the APMB, proposed by Zandt et al. (2003). Red squares denote stations used by Ward et al. (2014) and the dashed red line shows their suggestion of the maximum APMB extent. Dark blue stars denote the stations used by McFarlin et al. (2018) and Kukarina et al. (2017) while the yellow square shows the extent of the resistivity model of Comeau et al. (2016). Solid dark green line shows ANCORP reflection and magnetotellurics profile (Brasse et al., 2002; Oncken et al., 2003). White lines show extent of the "sombrero pattern" (Fialko and Pearse, 2012). Dashed magenta line shows the lateral extent of the best fitting APMB in our model at its widest part (15 km depth).

thin layer at 12 to 15 km depth but as their profile is further north, and considering the extent suggested by Zandt et al. (2003) and Ward et al. (2014), this study might be imaging the edge of the body. Supplementary Figure S1 summarizes the various suggestions for the extent of the APMB beneath its central volcano Uturuncu.

Using the same stations as McFarlin et al. (2018) and travel time inversion, Kukarina et al. (2017) present a distinctly different feature beneath Uturuncu, which is only 20 km in diameter and extends from about 5 km down to 40-80 km (depending on the isocontour) depth. The V_p-model of Heit et al. (2008) shows low velocities in the entire lithosphere which coincides with low electrical resistivities reported by Brasse et al. (2002) and Kühn et al. (2018).

Considering that the overwhelming majority of studies, including the large scale tomography of Yuan et al. (2000), image a low velocity zone within the upper half of the crust, we will focus on this scenario. The presence of partially molten areas in the lower crust is likely but the available geophysical constraints on their size and location are not sufficient to include them in the model.

3.2.2 InSAR data

We use surface deformation data to check the results of our forward models. Fialko and Pearse (2012) present gridded average line of sight (LOS) velocities from 1992 to 2010 and Lau et al. (2018) show how the maximum velocity has evolved from 1992 to 2018 (Figure 3.2). Both data sets are available at `https://igppweb.ucsd.edu/~`

fialko/data.html. To compare our modeling results to LOS velocities, we need to project them into LOS direction according to:

$$\Delta LOS = [U_n sin(\phi) - U_e cos(\phi)] sin(\lambda) + U_z cos(\lambda) \tag{3.1}$$

where ΔLOS is LOS velocity, U_n , U_e and U_z are the north, east and vertical component of the velocity vector respectively, ϕ is the azimuth (flight direction) of the satellite and λ is its incidence angle (Fialko et al., 2001). We use $\phi = -167.5$ and $\lambda = 21.5$ which are the averages between the two similar descending satellite tracks (ERS 10 and 282) used to create the LOS data set (Henderson and Pritchard, 2017).

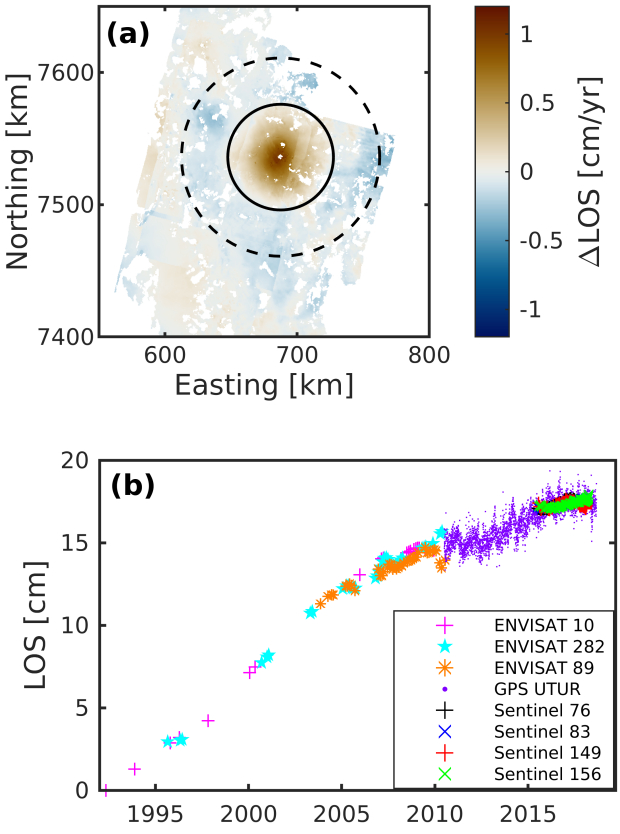

FIGURE 3.2: (a) Average LOS (line of sight) velocity from 1992 to 2010 from Fialko and Pearse (2012) around Uturuncu volcano. Circles correspond to the region of uplift (inner) and subsidence (outer) and are identical to the ones in Figures 3.1, 3.3a and 3.7. (b) Total vertical displacement of the center of uplift over time (Lau et al., 2018).

3.2.3 Gravity data

To help constrain the location and properties of the APMB, we consider gravity data. We compared the Bouguer anomaly grid (EGM2008, gravity_anomaly_bg, 0.05° resolution, 6 Sigma Gaussian filter with 75 km length) from the International Center for Global Earth Models (ICGEM, http://icgem.gfz-potsdam.de/home Barthelmes and Köhler, 2016) for the area of interest with the large regional data set

of the Collaborative Research Center 267 (SFB 267), presented in Götze and Kirchner (1997) (http://www.cms.fu-berlin.de/sfb/sfb267/results/data_catalogue/central_andean_data/gravitiy_data.html). Both data sets agree well (Figure 3.3c) and we decided to use the grid of the ICGEM (Figure 3.3a) for its regular resolution and larger area coverage.

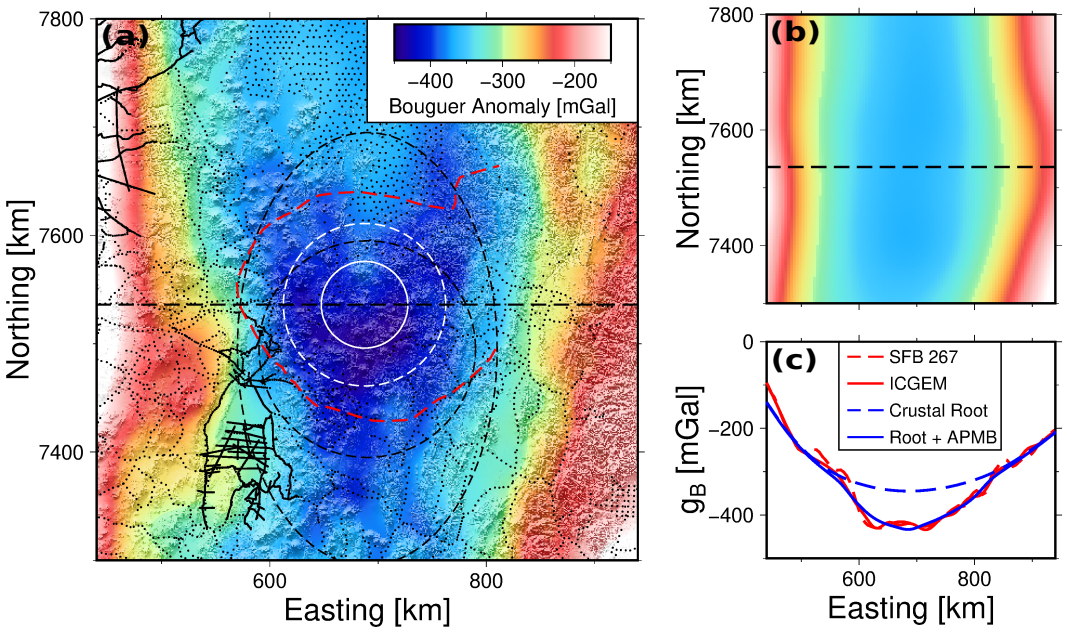

FIGURE 3.3: (a) Bouguer anomaly for the area of interest downloaded from the ICGEM (Barthelmes and Köhler, 2016) and low-pass filtered with a cut-off wavelength of 75 km. Black dots show gravity stations used for the regional SFB 267 survey. Dashed red line shows the extent of the APMB suggested by Ward et al. (2014). White lines show extent of the "sombrero pattern" (Fialko and Pearse, 2012). Thin black dashed lines show areas of different weights for eq. 3.2. The map covers the area between 69.5° W and 65° W as well as between 24.5° S and 20° S. (b) Bouguer anomaly of our version of the crustal root (same colorbar as in a). (c) Bouguer anomaly (g_B) along the EW-profiles in a and b for the data sets of the ICGEM (red solid) and the SFB 267 (red dashed). Blue dashed line shows the signal produced by our crustal root geometry and blue solid line shows the combined signal of crustal root and APMB.

3.2.4 Constraining the magma body's geometry

The center of our thermomechanical model is the APMB, whose shape, size and location we can constrain with the aforementioned insights from seismic imaging and gravity. We use the open source software geomIO (Bauville and Baumann, 2019, https://bitbucket.org/geomio/geomio) to create the 3D bodies that make up the system as it allows for the creation of 3D objects from drawn 2D slices and also provides an option to forward model the Bouguer anomaly of the created objects, using the approach of Talwani et al. (1959). To reproduce the gravity signal in a large mountain belt like the Andes, it is important to consider the influence of the thickened Andean crust, or more precisely, the crustal root that provides the necessary buoyancy for the large mountain masses. Its signal is evident in Figure 3.3a as the entire plateau shows Bouguer anomalies of about -350 mGal.

The root is approximated as a buoyant body (lower crust surrounded by denser mantle material) extending from 35 km depth to the Moho. We consider 3 different studies for constraints on Moho depth and density of lower crust and upper mantle

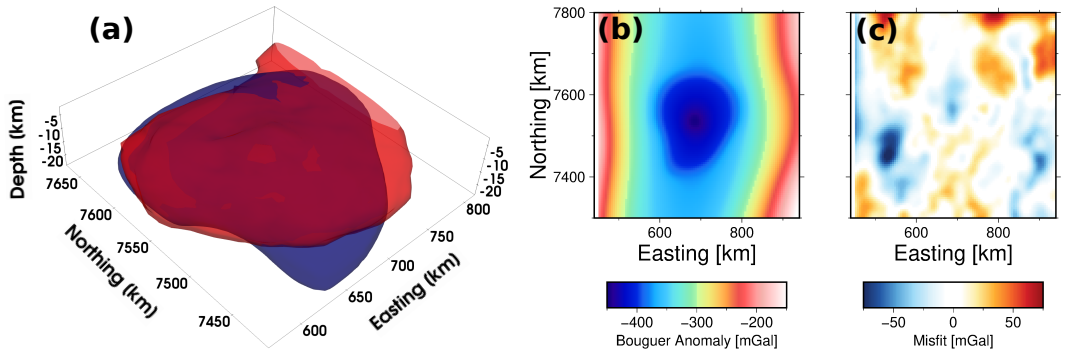

FIGURE 3.4: Results of the joint interpretation of seismic imaging and gravity data. (a) Our reference model of the APMB (blue) in comparison with the 2.9 km s $^{-1}$ isocontour from Ward et al. (2014) (red). (b) Gravity signal produced by the blue body in a. (c) Misfit of the signal in b to the data shown in Figure 3.3a.

(Prezzi et al., 2009; Tassara and Echaurren, 2012; Laske et al., 2013). Results show that a density contrast of 390 kg m^{-3} between crustal root and upper mantle, which is in the middle of the range of the aforementioned studies, allows us to reproduce the background gravity signal well (supplementary Figure S5).

Figure 3.3b shows the signal produced by the constructed crustal root to be in line with the observed Bouguer anomaly. The disparity between the calculated signal of the crustal root (dashed blue line) and the observed signal (red lines) in Figure 3.3c is interpreted to be the contribution of the APMB which we added as a second buoyant body in the crust. As we have no constraints on the exact distribution of material within the APMB and as gravity signals tend to average out small scale signals, we assumed the APMB to have a homogeneous density contrast to the surrounding crust. Depth, size and geometry were oriented towards the 2.9 km s^{-1} isocontour from Ward et al. (2014), but the body had to be extended and slimmed in the south to get a better fit to the gravity data (Figure 3.4). For the APMB, we found a $\Delta\rho$ of 125 kg m^{-3} to produce a good fit, which is similar to what Potro et al. (2013) and Gottsmann et al. (2017) use. The deviation from the data in the area above the APMB is ± 20 mGal (Figure 3.4b) and the biggest error is in the area of the Central Andean Gravity High (CAGH) (Götze and Krause, 2002), a dense body which is not part of our model.

3.2.5 Gravity inversion

Previous studies have used geophysical surface observations to constrain density and rheology simultaneously, but have assumed a constant model geometry (Baumann and Kaus, 2015). Here, we improve the approach by taking a variable geometry of the APMB into account, which allows us to investigate the relationship between the geometry of the magma body and the surface observations. The non-unique nature of gravity anomalies allows for a range of solutions as there is a trade-off between the density contrast of a body and its volume. To estimate the extent of realistic parameter combinations, we test a large number of different geometries and density contrasts which we generate automatically based upon our hand drawn reference model (Figure 3.4a). Supplementary text S1 describes our methodology for geometry variation. We use 2 control polygons (in 8.9 and 11.1 km depth) and the stretch factors Sx_1, Sx_2, Sy_1 and Sy_2 to transform the body in x(EW)- and y(NS)-direction (Figure 3.6f+g).

We then model the Bouguer anomaly of the geometry and compute the misfit between each model and the data, using a weighted RMS misfit function:

$$\Phi = \sqrt{\frac{\sum w_i (gB_{mod,i} - gB_{obs,i})^2}{\sum w_i}} \tag{3.2}$$

where Φ is the misfit of a model, gB_{mod} and gB_{obs} are the modeled and observed Bouguer anomalies respectively and w is the weight of the grid point. Every grid point inside a radius of 100 km from the location of the lowest Bouguer anomaly received the weight 1, while every grid point inside an ellipse with semi-major axes 120 (EW) and 200 (NS) km received a weight of 0.5 (Figure 3.3a). This allows us to exclude the effect of the (CAGH) (Götze and Krause, 2002), which is not part of our model, and limit the influence of grid points outside of the APMB's signal. We generate an initial set of 32768 (8^5) unique models using uniformly distributed values in the range of 0 and 250 kg m^{-3} for $\Delta\rho$ and in the range of 0.1 and 2.0 for the stretch factors. Next, we use the neighborhood algorithm (Sambridge, 1999a) to produce another 60000 models in areas of low misfit.

3.2.6 Lithospheric structure

For the lithospheric structure surrounding the APMB, we use a horizontally layered compromise between the global model crust 1.0 (Laske et al., 2013) and three regional crustal models based on rock chemistry and gravity inversion (Prezzi et al., 2009; Tassara and Echaurren, 2012; Ibarra et al., 2019) summarized in supplementary Figure S5. Sparks et al. (2008) studied the eruption products of Uturuncu and reported dacitic lavas with up to a few wt% of andesitic inclusions, concluding the APMB to be build by a lower layer of intruding andesites and an upper layer of more evolved dacites which are the product of differentiation and extensive crustal melting. This concept is supported by isotope studies (e.g., Kay et al., 2010; Michelfelder et al., 2014; Godoy et al., 2017; Wörner et al., 2018), which is why we split the APMB into a more viscous, dacitic, upper and a less viscous, andesitic, lower part. We put the boundary between both parts at the same depth as the upper crust/middle crust interface as we expect the andesites to naturally stall at this buoyancy boundary. Table S1 summarizes the material parameters and Figure 3.5 shows the setup used for the thermomechanical models.

3.2.7 Thermomechanical model

For our models we use the 3D thermomechanical finite differences code LaMEM (Kaus et al., 2016). It solves for the conservation of momentum, mass and energy (eq. 3.3-3.5), using a staggered grid in combination with a marker-in-cell approach (Harlow and Welch, 1965). Along the boundaries of the setup, we apply free slip conditions, allowing velocities > 0 parallel to the walls while setting perpendicular velocities to 0. At the top of the setup, we include about 10 km of sticky air above the stabilized free surface (Kaus et al., 2010; Duretz et al., 2011; Crameri et al., 2012).

$$\frac{\partial \tau_{ij}}{\partial x_j} - \frac{\partial p}{\partial x_i} + \rho g_i = 0 \tag{3.3}$$

$$\frac{1}{K}\frac{Dp}{Dt} - \alpha\frac{DT}{Dt} + \frac{\partial v_i}{\partial x_i} = 0 \tag{3.4}$$

$$\rho C_p \frac{DT}{Dt} = \frac{\partial}{\partial x_i}\left(\lambda \frac{\partial T}{\partial x_i}\right) + H \tag{3.5}$$

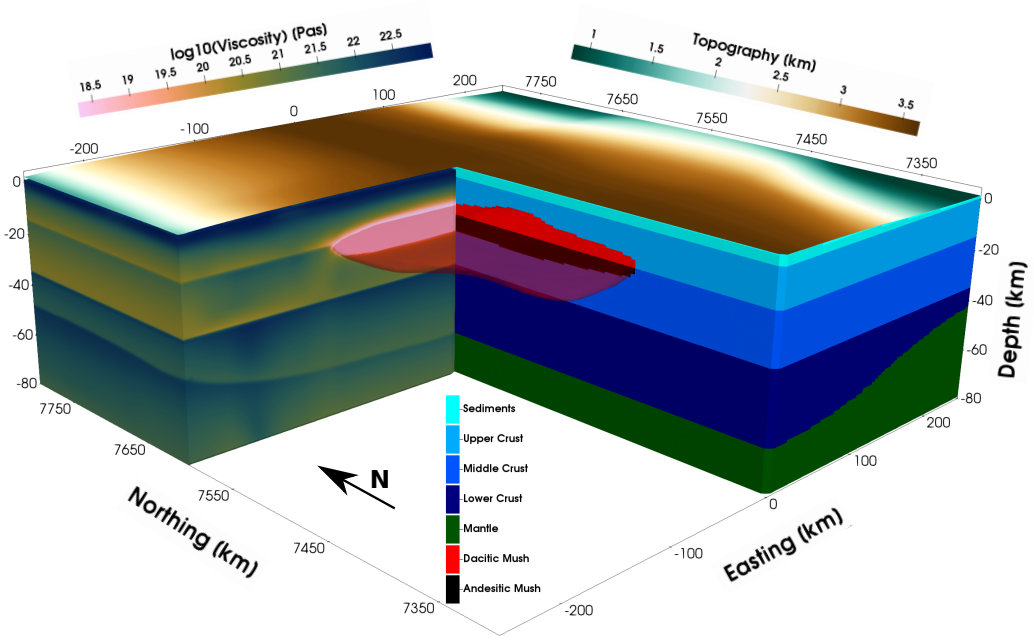

FIGURE 3.5: Setup for thermomechanical models based on crustal structure studies and our gravity analysis for crustal root and magma body. Vertical exaggeration: 2. Details on the material properties in table S1. Details on the synthetic topography in supplementary text S2.

τ_{ij} is the Cauchy stress deviator, $x_i (i = 1, 2, 3)$ denotes the Cartesian coordinates, p is pressure (positive in compression), ρ density, g_i gravitational acceleration, K the bulk modulus, α the thermal expansion coefficient, T the temperature, v_i the velocity vector, C_p the specific heat capacity, λ the thermal conductivity, H the volumetric heat source and D/Dt is the material time derivative. The rocks are characterized by a visco-elasto-plastic rheology where the strain rate is the sum of the elastic, viscous and plastic components:

$$\dot{\epsilon}_{ij} = \dot{\epsilon}^{el}_{ij} + \dot{\epsilon}^{vi}_{ij} + \dot{\epsilon}^{pl}_{ij} \tag{3.6}$$

$\dot{\epsilon}_{ij}$ denotes the total deviatoric strain rate tensor, while $\dot{\epsilon}^{el}_{ij}$, $\dot{\epsilon}^{vi}_{ij}$ and $\dot{\epsilon}^{pl}_{ij}$ represent the elastic, viscous and plastic strain rate components. For a detailed discussion of this equation and all of its components, the reader is referred to Kaus et al. (2016). Here we will focus on the material parameters which impact the 3 components.

The elastic component is controlled by the shear modulus G, which we compute from an averaged profile from Ward et al. (2017) (table S1). We also consider the rocks to be compressible and use a Poisson's ratio ν of 0.2 for all crustal rocks and the mantle (Gercek, 2007).

The viscous component is characterized by the viscosity η, which follows the temperature- and strain rate-dependent powerlaw relationship of dislocation creep:

$$\eta = \frac{1}{2}(B_n)^{-\frac{1}{n}}(\dot{\epsilon}_{II})^{\frac{1}{n}-1}\exp\left(\frac{E_n}{nRT}\right), \tag{3.7}$$

where B_n is the creep constant, $\dot{\epsilon}_{II}$ the square root of the second invariant of the strain rate ($\dot{\epsilon}_{II} = (\frac{1}{2}\dot{\epsilon}_{ij}\dot{\epsilon}_{ij})^{1/2}$), E_n the activation energy, n the powerlaw exponent, R the universal gas constant and T the temperature. All viscous parameters are summarized in table S1.

The plastic component is controlled by the yield strength τ_{yield}, which depends on the pressure p as well as the material parameters cohesion c_0 and friction angle ϕ:

$$\tau_{yield} = \sin(\phi)p + \cos(\phi)c_0 \tag{3.8}$$

Equation 3.8 corresponds to the Drucker-Prager failure criterion (Drucker and Prager, 1952) which is a good approximation of Byerlee's law Byerlee, 1978. Most research on magmatic rock friction angles is limited to granites and results usually vary around 30° (Jang et al., 2018). Cohesion estimates for intact rocks typically range around a few MPa (e.g., Hoek and Brown, 1997). Therefore we use $\phi = 30°$ and $c_0 = 10$ MPa for all rocks.

We use 256 cells in each horizontal direction and 128 cells in the vertical. This yields roughly 8.5 million cells and a horizontal resolution of 1.95, as well as a vertical resolution of 0.74 km. As we are interested in the present day state of the system, we only run the model for two time steps. The first timestep is not considered, as there is still influence of isostatic balancing between topography and Moho. From the second timestep onward, the surface velocities are dominated by the buoyancy of the magma body.

3.3 Results

3.3.1 Gravity inversion

To visualize the results of the gravity inversion, we plot the misfit of each individual model in dependence of 2 out of the 5 parameters. Figure 3.6a-c show a selection of the most important ones while a full overview can be found in Figure S2. There is a good correlation between $\Delta\rho$, Sx_1 and Sy_1 with the best fitting models being constrained between 80 to 130 kg m^{-3} and 0.8 to 1.3, respectively (Figure 3.6a,b). Sx_2 and Sy_2 show large spread with the range of low misfit models being controlled by $\Delta\rho$, Sx_1 and Sy_1 entirely (Figure 3.6c). This demonstrates that the lateral extent of the APMB is poorly constrained for the upper part of the magma body. We also performed an independent set of 1000 models, only varying $\Delta\rho$ and the vertical extent of the APMB (S_z). The results are displayed in supplementary Figure S3a and show that a $\Delta\rho$ of roughly 200 kg m^{-3} would be necessary to fit the Bouguer anomaly with a magma body of 9 km thickness as proposed by McFarlin et al. (2018). We therefore decided to keep the thickness of the APMB fixed to the extent suggested by Ward et al. (2014) to reduce the parameter space to a reasonable size for our investigation.

To obtain a more quantitative result, we follow a Bayesian inversion strategy and resample the parameter space with the rejection approach described by Sambridge (1999b). We use uniformly distributed random numbers in the ranges of 0 to 250 kg m^{-3} for $\Delta\rho$ and 0.1 to 2.0 for all stretch parameters as our priors. The resampling algorithm is described in more detail in supplementary text S4 and Figures 3.6d+e summarize the results. The accepted samples for $\Delta\rho$ show a normal distribution with a mean (μ) of 111 kg m^{-3} and a standard deviation (σ) of 9.7 kg m^{-3}. The stretch factors for the lower control polygon Sx_1 and Sy_1 are also normally distributed with $\mu = 1.04$ and 1.23 respectively and $\sigma = 0.08$ and 0.12. Samples for Sx_2 and Sy_2 which are related to the upper control polygon show no bell curve distribution but are instead found within the entire range with Sy_2 trending towards the lower and Sx_2 towards the upper end.

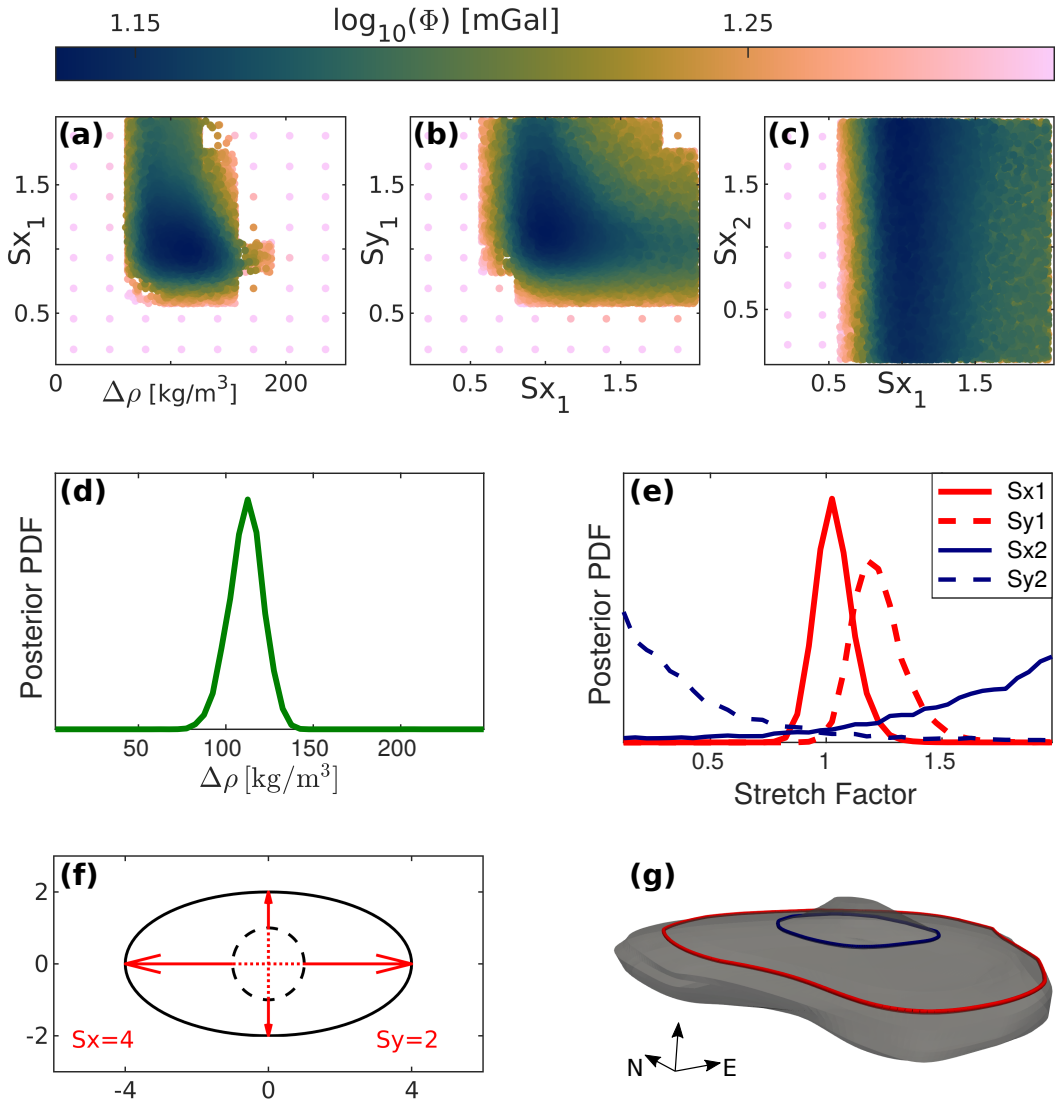

FIGURE 3.6: (a-c) Misfit (Φ) in dependence of sets of 2 parameters. Note that each dot in the areas of high misfit is the best fitting model of 512 (8^3) versions that all plot on the same coordinate when they are projected in this 2-dimensional parameter space due to the regular gridded initial models. (d-e) Posterior probability density functions (PDF) resulting from resampling the gravity models. (d) PDF for density contrast $\Delta\rho$, showing it to be 111 $\pm$ 9.7 kg m^{-3}. (e) PDF for Sx_1 in solid red, Sy_1 in dashed red, Sx_2 in solid blue and Sy_2 in dashed blue. This shows that the geometry of the lower part of the APMB (Sx_1 and Sy_1) is well constrained and can be described by Gaussian distributions. The opposite is the case for the upper part (Sx_2 and Sy_2). (f) Sketch to show how Sx and Sy affect a single polygon (dashed = original, solid = new). (g) 3D view of reference APMB. Everything below control polygon 1 (red) is affected by Sx_1 and Sy_1, while everything above control polygon 2 (blue) is affected by Sx_2 and Sy_2. Central part is affected by both sets.

3.3.2 Thermomechanical models

Using the magma body, constrained by seismic imaging and gravity modeling, we performed forward models in LaMEM to predict surface velocities and used eq. 3.1 to project them into line of sight direction. While the result did show areas of uplift and areas of subsidence, the pattern did not match the InSAR observations (Figure 3.7b). It was however apparent that the uplifting area was overlying the central rise of the APMB (i.e. where it was shallowest). As the spatial resolution of seismic imaging and gravity do not allow to constrain smaller scale features of the APMB, we altered the location and geometry of the central rise and achieved an improved fit to the InSAR data (Figure 3.7c). The model produces a circular, 80 km wide area of positive ΔLOS, with peak velocities of 1.1 - 1.2 cm/yr. Around the uplifting area, there is a diffuse ring of subsidence with ΔLOS of -0.3 to 0 cm/yr and a diameter of roughly 150 km. The ring is broken in the north-west and east where we find areas of minor (ΔLOS < 0.3 cm/yr) uplift and the remaining surface does not move noticeably. We also reproduce the 6 km westwards shift of peak ΔLOS when projecting the surface velocities into the ascending satellite track ENVISAT 89 ($\phi = -13$ and $\lambda = 41.1$), as reported by (Fialko and Pearse, 2012).

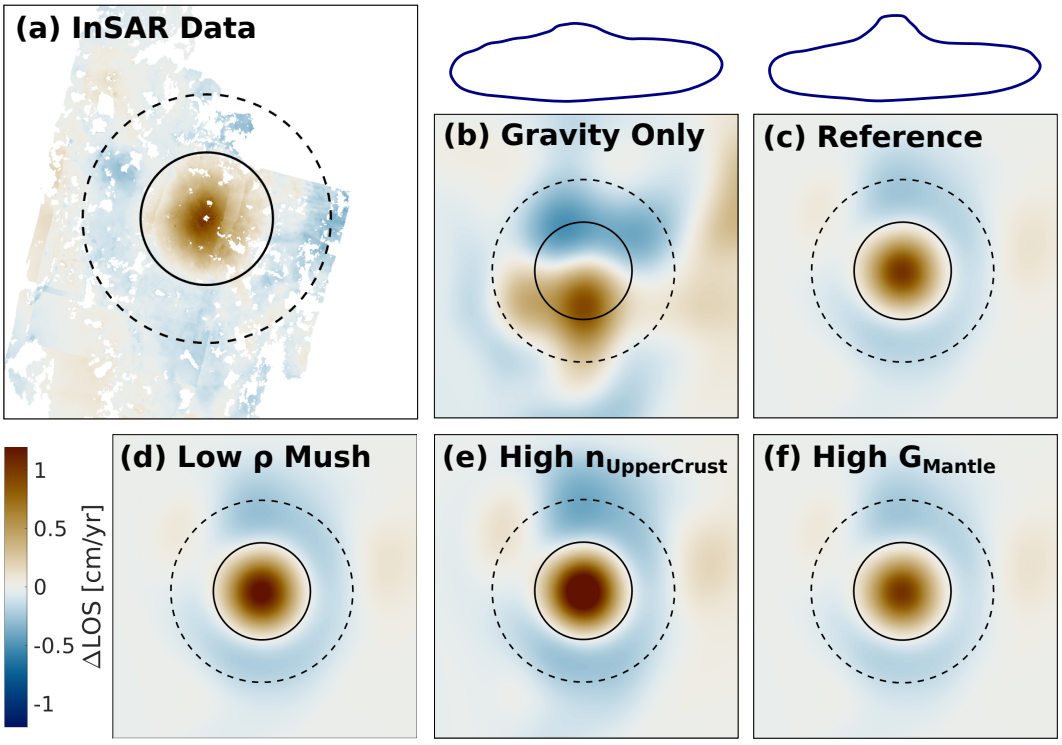

FIGURE 3.7: Comparison between InSAR data and the surface velocities of different models projected into LOS. Solid and dashed circles are for orientation and are identical to the ones in Figures 3.1, 3.2 and 3.3. (a) InSAR data. (b) Result of the geometry, solely constrained by seismic imaging and gravity. (c) Results after altering location and geometry of central rise and basis for the 2nd row. (d) Variation of c with a lower density mush. (e) Variation of c with a higher powerlaw exponent in the flow law of the upper crust. (f) Variation of c with a higher shear modulus in the mantle. Sketches above b and c are vertically exaggerated 2D-EW slices of the APMB that illustrate, how the shape of the central rise was changed between them.

Taking a look at the velocity field inside and around the APMB shows that material is flowing from the outskirts of the APMB towards the central rise and upwards,

pushing the overlying crust up and creating the concentric area of uplift (Figure 3.8a). At the same time, the crust overlying the parts of the APMB that are drained from sinks down, creating the ring of subsidence at the surface. There is also some minor flow towards the NW- and NE-edge of the magma body, corresponding to the two areas of minor uplift (Figure 3.7c). Given the aforementioned uncertainty in the geometry of the APMB's central rise, we investigated how changing it impacted the system. Figure 3.8b illustrates how thinning the central rise to half its diameter restricts the flow inside the APMB and weakens the surface deformation pattern.

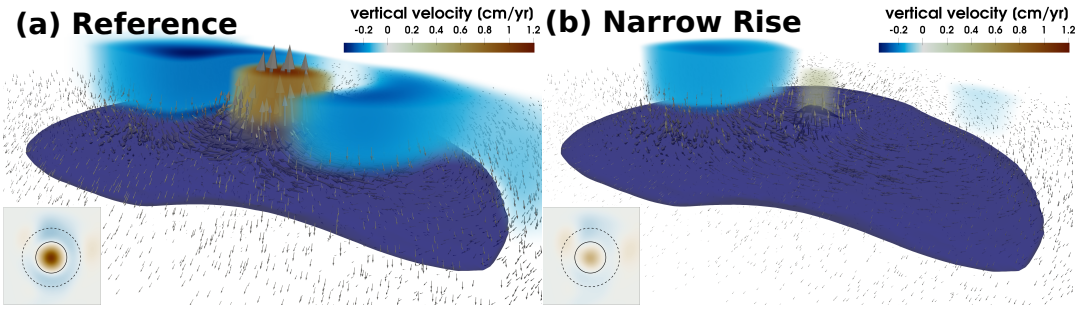

FIGURE 3.8: Velocity field inside and around APMB for the reference case (a) and a case where the central rise was narrowed to 50% of its diameter (b). Shaded areas show vertical velocity in the crust above the magma body. Areas between -0.1 and 0.3 cm/yr were made completely transparent for better visibility of the relevant features. Insets show the corresponding surface deformation, using the colorbar of Figure 3.7.

To gain more insight into the parameters that the model is sensitive to, we performed an automated sensitivity testing for the vertical velocity at the summit of Uturuncu following the approach of Reuber et al. (2018a). With a model and parameter set that can match the observations well, we can compute the finite-difference gradients of all parameters as well as a scaling law that describes how influential individual parameters are on the observation point. It has the form:

$$u_{obs} = A p_1^{b_1} p_2^{b_2} ... p_n^{b_n} \tag{3.9}$$

where u_{obs} is the observed velocity, A is a pre-factor, p_1 to p_n are the model parameters and b_1 to b_n are the respective scaling law exponents. If $b_i > 0$, an increase in parameter p_i will lead to an increase in u_{obs} and vice versa for $b_i < 0$. The absolute value of the scaling law exponent describes how strongly a relative change in the respective parameter would change the observable. Figure 3.9 shows $|b|$ for all model parameters, with upwards pointing triangles corresponding to $b > 0$ and downward pointing triangles corresponding to $b < 0$.

The scaling law suggests that the rheology of the upper crust (controlled by the activation energy En, the powerlaw exponent n and indirectly by the initial temperature T of the dacitic mush) is most influential on the maximum surface deformation. It is followed by the density contrast between dacitic mush and upper crust, the elastic components (shear modulus G and poisson ratio ν) of the dacitic mush as well as the geometry of the central rise (Sx_2 and Sy_2). The plastic parameters cohesion c_0 and friction angle ϕ as well as most thermal parameters (thermal expansivity α, heat capacity Cp and thermal conductivity k) that are not associated with the upper crust or dacitic mush have little effect on the surface velocity. The lower row of Figure 3.7 shows that the conclusions from the scaling law exponent analysis are consistent with our forward simulation results as Figure 3.7e represents an increase of the powerlaw exponent of the upper crust by 20% which is associated with a strong increase in LOS

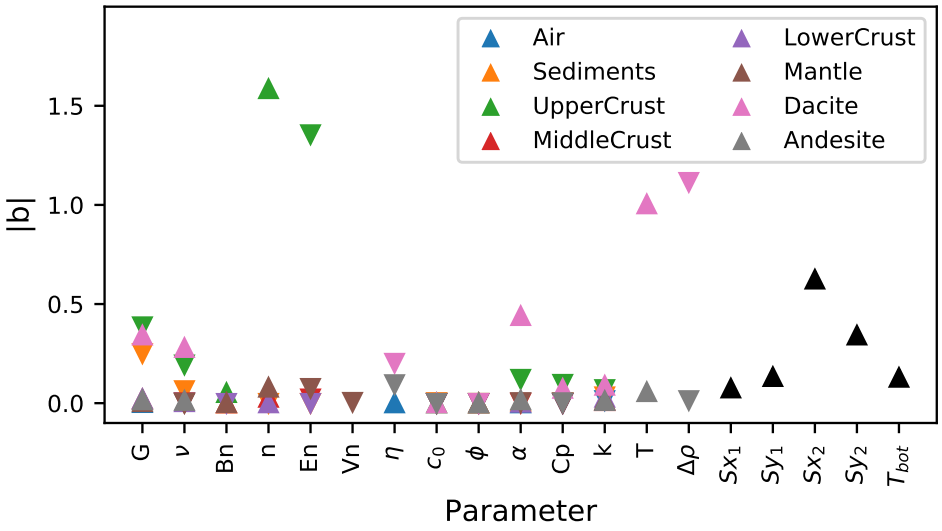

FIGURE 3.9: Automatically computed scaling law exponents for all parameters. The absolute value (|b|) of the exponent of a parameter is a measure of how strongly a relative change in that parameter would change the observation (in this case, the vertical velocity at the summit of Uturuncu). Note that not all materials use the same parameters (for instance, Dacite is characterized by linear viscosity η while the upper crust's rheology is defined by Bn, En and n). $\Delta\rho$ describes the density contrast between the magma and its associated host rock. Parameters Sx_1, Sy_1, Sx_2 and Sx_2 are geometric parameters of the APMB and T_{bot} the temperature at the bottom of the model. They are therefore not associated with any one material.

velocities. In Figure 3.7f, the shear modulus of the mantle was increased by 20% with little to no effect on the surface displacement. Figure 3.7d shows how changing the density contrast between crust and mush by 20% affects the system.

Running the model for a longer amount of time does not affect the surface deformation pattern. Only the amplitude of the velocities decreases over time, which is to be expected as without new supply of magma, the system will eventually reach isostatic equilibrium between the buoyant mush and the surface elevation it has uplifted. Fialko and Pearse (2012) report the same observation in their diapir model.

3.4 Discussion

3.4.1 Seismic imaging and gravity

The joint interpretation of seismic imaging studies and gravity data provides a robust picture of the large scale geometry of the APMB which neither data set could have provided on its own. Computing more than 90'000 different interpretations also allows us to estimate its uncertainties. The analysis also supports the concept of a magma body of about 15 km in thickness, as proposed by Ward et al. (2014). Figure S3a shows that a quite high $\Delta\rho$ of $\sim 200\ \mathrm{kg\,m^{-3}}$ and, associated with that, a melt content in the range of 40% (Figure 3.10) would be necessary to fit the thickness range (≈ 8 km) proposed by McFarlin et al. (2018). The case is even worse for a 1 km thin melt zone as suggested by the studies of the late 90s and early 2000s (e.g., Chmielowski

et al., 1999; Zandt et al., 2003). We did not extend our calculations to that range, but the trend in Figure S3a suggests that even pure melt would not be enough to reproduce the observed Bouguer anomalies with such a thin layer. As the center of the body is roughly at the same depth in all three scenarios, it is likely that it contains the highest melt fraction.

The resampling of the gravity data (Figure 3.6e) shows that the extent of the APMB below 11 km depth (defined by Sx_1 and Sy_1) is well constrained by the Bouguer anomalies. In EW-direction the size of our reference model fits the Bouguer anomalies well ($\mu_{Sx_1} = 1.04$) while it should be extended in NS-direction ($\mu_{Sx_1} = 1.23$). Figure 3.1 shows the maximum lateral extent of our best fitting geometry. Its northern edge coincides with the ANCORP profile (Oncken et al., 2003), suggesting that the thin low velocity layer they imaged, represents the edge of the APMB. The upper part of the magma body cannot be constrained with the help of gravity data. Despite being closer to the surface, the lower mass within the central rise has too little influence on the overall signal of the APMB. It is not clear why Sx_2 trends towards high and Sy_2 towards low values but the fact that we find samples within the entire parameter range shows the small influence of these parameters for the Bouguer signal.

3.4.2 Melt content

The constraints we gained on $\Delta\rho$ allow us to make estimations on the melt fraction within the APMB by assuming the APMB to be a mix of melt and crustal material, and computing the mass balance between both components. Melt density depends on its composition (table S2), including volatile components as well as temperature and pressure. Laumonier et al. (2017) proposes H_2O contents of up to 10 % for the lower andesitic part of the magma body. Figure 3.10 shows the correlation between density contrast, density of the crust, H_2O content and melt fraction. The red ellipsoid displays likely ranges for the density contrast (this study), density of the middle crust (Tassara et al., 2006; Prezzi et al., 2009; Laske et al., 2013; Ibarra et al., 2019) and H_2O content (Laumonier et al., 2017). Based on these ranges, the melt content in the andesitic part of the APMB should be on the order of 15-22 vol-%, which is in line with the estimation of 14-27 % based on several electrical conductivity studies (Schwarz and Krüger, 1997; Schilling et al., 2006; Comeau et al., 2015; Comeau et al., 2016). It also coincides with the upper range of the estimation of Ward et al. (2014) (4-25%) based on the reduction of shear wave velocity and with the preferred model of Potro et al. (2013) (∼25%) which is based on gravity data but proposes a different distribution of melt than this study. For the dacitic part we lack estimates for water content but assuming a similar range, we would expect about 5% more melt in the upper part of the APMB.

3.4.3 Thermomechanical modeling

3.4.3.1 The central rise

Modelling the thermomechanical dynamics of the system highlights that transport of mush material from the outskirts to the center of the APMB is crucial to reproduce the surface deformation pattern observed by InSAR (Figures 3.7 and 3.8). It also shows the necessity for a pronounced rise in the body. As the center of surface uplift depends on the location of the central rise and the pattern and magnitude of deformation on its shape and size, we can constrain how the APMB's shallow areas look like, which would not have been possible by only considering seismic imaging and gravity data (Figure 3.6e). To constrain the geometry of the central rise we ran 1000 forward

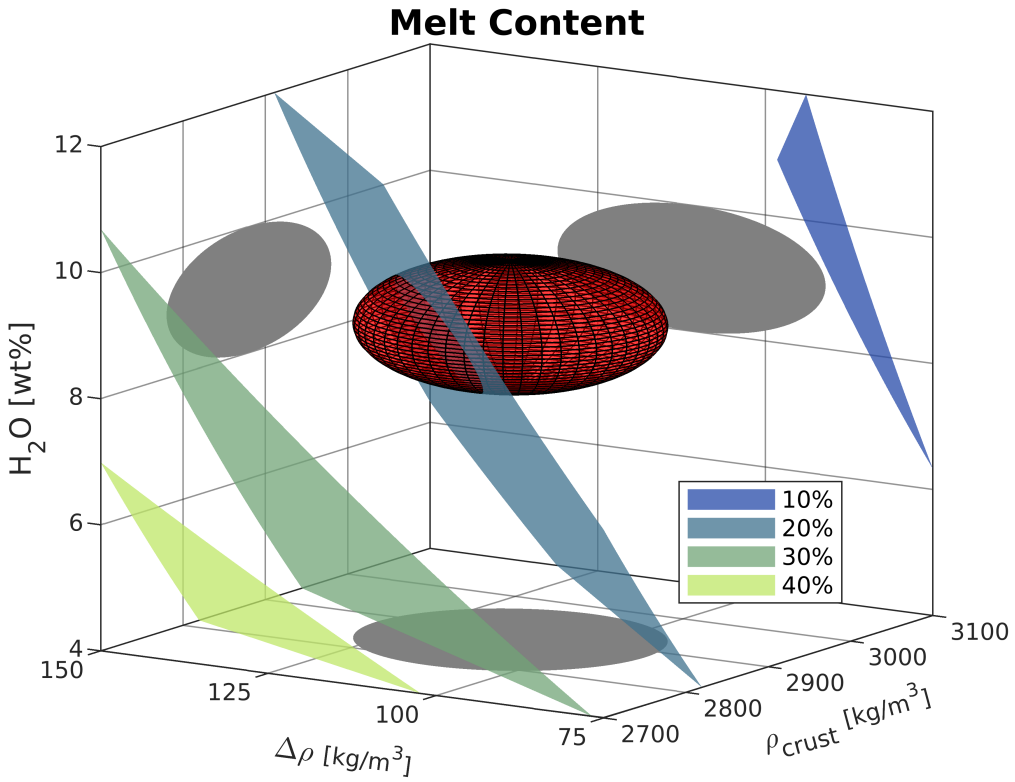

FIGURE 3.10: Estimation of andesitic melt content of the lower half of the APMB in dependence of crustal density, density contrast and H_2O content. Red ellipsoid indicates the data range, assumed in this study (gray ellipses are 2D projections). Planes show melt content. Details on the calculations are found in supplementary text S3.

models (400 initial + 600 in areas of low misfit) using 1.04 and 1.23 for Sx_1 and Sy_1 respectively, and 110 kg m^{-3} for $\Delta\rho$ while varying Sx_2 and Sy_2 in the entire range between 0.1 and 2.0. We kept the other three parameters constant as they are already well constrained from gravity and to reduce the size of the parameter space for the computationally more expensive thermomechanical models. Similarly to the gravity data, we resampled the models to get a probability distribution for Sx_2 and Sy_2, using the misfit between the modeled surface velocities projected into LOS (eq. 3.1) and the InSAR data (Figure 3.2a).

The resampling resulted in near-gaussian distributions for both stretch factors which are characterized by $\mu_{Sx2} = 0.70$ and $\mu_{Sy2} = 1.04$ as well as $\sigma_{Sx2} = 0.03$ and $\sigma_{Sy2} = 0.05$. Figure 3.11 combines these results with an interpolated representation of the gravity resampling. This demonstrates that analyzing the Bouguer anomalies (green curves) provides little to no constraints on the upper parts of the APMB but incorporating the thermomechanical simulations can compensate for that as the surface velocities are very sensitive to the geometry of the central rise. At the same time, the extent of the lower half of the APMB only has a negligible effect on the surface velocities. Combining the two approaches yields useful constraints on both the upper and the lower part of the magmatic system.

While the model can show the necessity for the central rise, it can not develop the rise from a flat topped APMB on its own. Consequently, it must have been initiated through some initial perturbation. One reasonable explanation is the reactivation of old pathways, as multiple geochemical studies suggest the transport of melt to

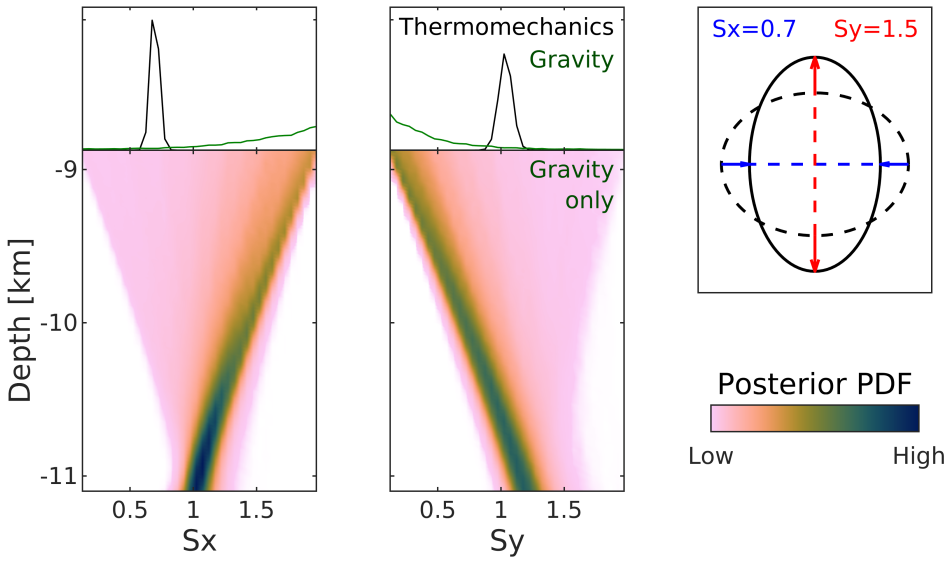

FIGURE 3.11: Combined results from the resampling of gravity and thermomechanical forward models. The lower sub-Figures show probability density for the stretch factors in 11.1 (Sx_1 and Sy_1) and 8.9 km depth (Sx_2 and Sy_2). White areas did not record a single sample among the accepted 20000. The upper sub-Figures show the results of the resampling of the thermomechanical models where only Sx_2 and Sy_2 were varied in black along the PDF of Sx_2 and Sy_2 from the gravity resampling in green. Right side shows another sketch of the way Sx and Sy influence a single polygon.

small, shallow magma reservoirs around sea level prior to eruptions (Sparks et al., 2008; Muir et al., 2014a; Muir et al., 2014b). Another possible explanation is the fact that the crust is hottest (and therefore weakest) above the center of the APMB, facilitating magma ascent there. Lastly, this may be the area where new batches of melt are emplaced from below. Provided that the deeply rooted, tooth-shaped anomaly imaged by Kukarina et al. (2017) represents melt pathways, the last scenario would be the most likely. The depth, location and width of the central rise's top agrees well with the top of this feature (Figure 3.12). Ward et al. (2014) also state that they see the magma body shallowest beneath Uturuncu.

3.4.3.2 Key parameters

The amplitude of the surface deformation pattern is controlled by the magnitude of material transport within the APMB, which in turn is a function of multiple quantities. The geometry of the central rise as well as the rheology of the upper crust and mush trade off against each other, so it is impossible to find a unique solution. We can, however, conclude that a change in any of them can explain the decrease in surface velocities over the past decade, as reported by Lau et al. (2018) (Figure 3.2b).

As both, rheology of the upper crust and of the magma mush depend on temperature, a loss of heat, possibly through waning magma supply or developing exit paths for hot fluids, would be a good candidate. Another possible scenario includes loss of volatiles or an increase in crystal content in the magma which can shift its viscosity by several orders of magnitude. This could also have a relevant effect on the surface velocities despite η_{Dacite} not ranking high in Figure 3.9. The possibility for a sudden

(on timescales of years to decades) slowdown of surface velocities could even help to solve the paradox that Gottsmann et al. (2018) are able to show that Uturuncu has been uplifting since 1965, while Perkins et al. (2016) show geomorphic evidence for no long-term (century scale) uplift. Another reason for the absence of long-term uplift is the aforementioned isostatic equilibrium that the buoyant magma reaches with the elevation it generated by uplift.

A look at deviatoric stresses in the crust show that they are highest above the central rise between surface and sea level, which is the only area where we observe plastic yielding in our simulations (for rock cohesion of both 1 and 10 MPa). This coincides with the domain where Jay et al. (2012) and Kukarina et al. (2017) detected the bulk of local earthquakes (Figure 3.12).

3.4.4 Comparison to other models

In this study, we present the first 3D model of the Altiplano-Puna magma system with a temperature- and strain rate-dependent visco-elasto-plastic rheology, including all deformation mechanisms that are observed for real rocks. As in the temperature-dependent visco-elastic model of Fialko and Pearse (2012), stresses are caused by density instabilities (i.e. light mush rising in a denser crust). Pritchard and Simons (2004), Hickey et al. (2013) as well as Henderson and Pritchard (2017) neglect buoyancy forces and create stresses through inflating point sources (Mogi Model (Mogi, 1958)) in a purely elastic or linear-visco-elastic (Hickey et al., 2013) crust. Gottsmann et al. (2017) is the only previous study that considered the entire magma body, using it as a source for depressurization, while pressurizing a vertically extending column. Figure 3.12 shows the different geometries proposed by the aforementioned studies.

There are some important similarities between our study and the work of Gottsmann et al. (2017), most notably the consideration of the entire APMB as an active part of the system and the presence of a central feature that attracts material. There is, however, a notable difference in the geometry of the central feature and to a lesser degree in the main body. But more importantly, Gottsmann et al. (2017) prescribe a pressure source in the vertical column (Figure 3.12) and a pressure sink in the rest of the body to simulate the effects of mush moving from there to the column. In our model, buoyancy forces are developing this flow of material self consistently, without a prescribed pressure source as the driving force.

An element that our study shares with the work of Fialko and Pearse (2012) is the role of buoyancy as the driving force of the system. But instead of a 10 km wide diapir of almost pure melt($\Delta\rho = 400\,\mathrm{kg\,m^{-3}}$), we consider the entire APMB as imaged by seismics and constrained by gravity as a buoyant body with a density contrast of about 110 $\mathrm{kg\,m^{-3}}$ to the surrounding crust.

3.5 Conclusions

We present a 3D nonlinear visco-elasto-plastic numerical model of the Altiplano-Puna magma system, which is consistent with observations made by seismic imaging, gravity surveys, crustal density models, earthquake locations and InSAR data. We use a joint interpretation of shear wave velocities and Bouguer anomalies to optimize the constraints on the extent of the APMB and to estimate its density contrast to the surrounding crust to be 90 - 130 $\mathrm{kg\,m^{-3}}$ (2σ). Based on that, and using crustal density models as well as the chemistry of eruption products, we can estimate the melt fraction in the lower part of the APMB to be 15-22 vol-%.

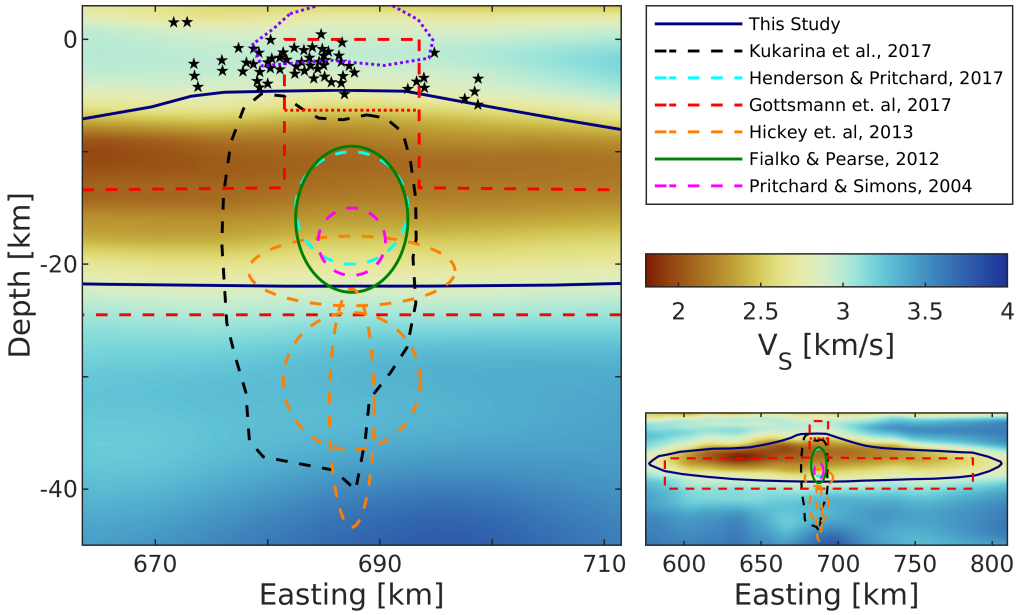

FIGURE 3.12: EW slice through the shear wave velocity model from Ward et al. (2014) beneath Uturuncu. On top, the various models that reproduce the observed InSAR pattern. Solid line models are density driven, dashed lines are inflating pressure sources. Black stars show earthquake locations from Kukarina et al. (2017) and dotted purple line shows bulk of earthquake locations reported by Jay et al. (2012). Dotted red line shows the transition between magma and hybrid material from Gottsmann et al. (2017). As most of the models of Pritchard and Simons (2004) plot on top of each other, they are summarized in one circle. Henderson and Pritchard (2017) also postulate a deflating pressure source at 65 km depth, which plots outside of the Figure. Dashed black line shows the Vp/Vs = 1.9 isocontour from Kukarina et al. (2017). Bottom right: Zoomed out to cover full body. Note the vertical exaggeration.

Forward models with the thermomechanical stokes code LaMEM show that the observed surface deformation can be caused by the buoyancy-driven transport of mush material from the outskirts of the APMB towards a central rise, pushing the overlying crust upwards. At the same time, the crust, overlying the areas being drained from, is subsiding in a ring-like pattern. In our model, there is no need for large intrusions (i.e. pressure sources) to reproduce the observed surface deformation. We also show the link between the geometry of the central rise and the surface deformation pattern and demonstrate that the amplitude of deformation depends mainly on the width of the rise as well as on the rheology of the upper crust and mush. Consequently, a better understanding of the rheological properties of upper crust and especially mush is necessary to improve our understanding of the dynamics of magmatic systems. Loss of heat or volatiles as well as growth of crystals are likely candidates to be currently slowing the surface deformation down and preventing long-term uplift.

Our results clearly show the advantages of using joint interpretations and physically consistent thermomechanical models, as most observables are only sensitive to parts of the system while leaving other parts unconstrained. Combining different data sets and different modeling techniques allows us to constrain more parameters and also quantify the uncertainties that the data include. Lastly, we demonstrate and quantify the influence of initial model geometries on the forward solution and recommend treating geometry as a parameter like rheology or density.

3.6 Acknowledgments

This study was funded by the European Research Council through the MAGMA project, ERC Consolidator Grant # 771143. The maps in Figures 3.1, 3.3 and 3.4 were created using the Generic Mapping Tool, version 5.4.3 (Wessel et al., 2013). We used perceptually uniform colormaps to prevent optical data distortion (Crameri, 2018). Parts of this research were conducted using the supercomputer Mogon II and/or advisory services offered by Johannes Gutenberg University Mainz (hpc.uni-mainz.de), which is a member of the AHRP (Alliance for High Performance Computing in Rhineland Palatinate, www.ahrp.info) and the Gauss Alliance e.V.. We also thank 2 anonymous reviewers for improving the quality of the manuscript with their suggestions.

Supplementary

3.A Open research section

Datasets for this research are available in these in-text data citation references:

- InSAR: (Fialko and Pearse, 2012),
  https://igppweb.ucsd.edu/~fialko/data.html

- Bouguer anomalies: (Barthelmes and Köhler, 2016),
  http://icgem.gfz-potsdam.de/home
  Model selection: EGM2008,
  Functional selection: gravity_anomaly_bg,
  Grid Step: 0.05°,
  Gaussian Filter: 6 Sigma, 75000 m

- Vs-model: (Ward et al., 2014; Ward et al., 2017),
  https://ds.iris.edu/ds/products/emc-apvcantrfward2014/,
  https://ds.iris.edu/ds/products/emc-apvcpunaantrfward2017/

Software for this research is available on zenodo at:

- LaMEM: (Kaus et al., 2016),
  http://doi.org/10.5281/zenodo.4419782

- geomIO: (Bauville and Baumann, 2019),
  http://doi.org/10.5281/zenodo.4339050

3.B Geometry manipulation

To manipulate the APMB's geometry, we cut it into horizontal polygons and choose two of those slices to be control polygons (red in Figure 3.F.4a). We define the stretch parameters (Sx_1 and Sy_1 for the lower control polygon, Sx_2 and Sy_2 for the upper one) and then compute the stretch parameters for all other polygons. Slices between the bottom of the body and the lower control polygon copy Sx_1 and Sy_1, slices in the middle are linearly interpolated and slices between upper control polygon and top of the body copy Sx_2 and Sy_2. Figure 3.F.4b shows an example of how this is done for $Sx_1 = 1.3$, $Sx_2 = 1.0$, $Sy_1 = 1.0$ and $Sy_2 = 1.5$.

The transformation is then applied to each polygon individually. First, we compute the position of the polygon's center of mass and transform the coordinates of all nodes on the polygon to be relative to it. Then, we multiply all relative x-coordinates with Sx and all y-coordinates with Sy. Finally, the relative coordinates are transformed back into absolute ones by adding the polygon's center of mass' coordinates again. Figures 3.6f and 3.11 show how the stretch parameters are applied to single polygons. The result on the entire body can be seen in Figure 3.F.4c. The lower part of the body was extended in x(EW)-direction ($Sx_1 > 1$) while its y(NS)-extent stayed constant

($Sy_1 = 1$). At the same time, the upper part was extended in y(NS)-direction ($Sy_2 > 1$) while not growing in x(EW)-direction ($Sx_2 = 1$).

To stretch the body in z(vertical)-direction, we multiply the spacing between the individual polygons with Sz (Figure 3.F.3b). There is only one Sz for the entire body and if it is larger than 1, the body extends in z-direction, if it is smaller than 1, it shrinks.

3.C Model topography

The initial topography plays an important role in the evolution of surface velocities since the setup will naturally try to approach isostatic equilibrium. It is therefore important to choose a topography which is very close to equilibrium with the buoyancy of the crustal root to not overshadow the surface motions caused by the buoyancy of the APMB (the InSAR data filter out the large scale movement due to isostacy by using a reference point and assuming a spatially constant rate for the entire area). Using the real topography proves impractical as it is not in isostatic balance with our lithospheric setup and has too many short wavelength components with its various peaks. To construct an isostatically balanced topography, we assume a flat surface at 3 km elevation, compute the lithostatic pressure across the bottom of the model (80 km depth) and then increase or decrease the surface elevation at every grid point until the pressure is the same across the entire bottom. This way, we achieve a topography which only needs one time step to be in equilibrium with the rest of the model, which significantly improves the speed of our simulations.

3.D Petrology

Table 3.F.2 summarizes the XRF analyses on both magma compositions (Sparks et al., 2008) and they are in line with the most abundant lavas in the entire APVC as reported by (Wörner et al., 2018). The chemistry of the magma also allows us to make estimations about the melt content within the APMB (see section 3.4.1).

If we assume the lava compositions of table 3.F.2 to be representative of the magmas in the upper and lower layer of the APMB respectively, we can compute their densities through the sum of the oxides:

$$\rho = \sum_{i=1}^{N} \frac{X_i M_i}{V_i} \tag{3.10}$$

ρ is the magma density, X_i the molar fraction, M_i the molar mass and V_i the molar volume of the respective oxide. V_i is a function of temperature and pressure:

$$V_i = \overline{V}_i + \alpha_i(T - 1673\,\mathrm{K}) + \beta_i(P - 0.1\,\mathrm{MPa}) \tag{3.11}$$

$\overline{V}_i$ is the partial molar volume of the oxide at 1673 K and atmospheric pressure. T and P are temperature and pressure respectively, α_i is the oxide's thermal expansion coefficient and β_i its compressibility. For the oxides, we use values from Lange and Carmichael (1987) ($\overline{V}$, α) and from Kress and Carmichael (1991) (β) while Ochs and Lange (1999) provide all 3 constants for H_2O.

3.E Resampling

In sections 3.3.1 and 3.4.3.1, we produce ensembles of parameter combinations and compute the misfit of their corresponding models to observations. By resampling these parameter combinations, we can use this information to gain robust estimates of the optimal parameter values and associated uncertainties. To resample the distribution, we follow the rejection procedure described by Sambridge (1999b). First, we generate a random proposal defined by five parameters $(\Delta\rho, Sx_1, Sy_1, Sx_2, Sy_2)$ in the gravity resampling or by two parameters (Sx_1, Sy_1) in the thermomechanical resampling. All parameters are generated from uniform distributions. We then calculate the acceptance ratio α for the proposal:

$$\alpha = exp(\gamma_{prop} - \gamma_{max}) \tag{3.12}$$

where *prop* refers to the current proposal and *max* refers to the best accepted proposal so far (the first proposal is always accepted as γ_{max} cannot be evaluated). γ is the argument of the likelihood function presented in Sambridge (1999b):

$$\gamma(m) = -\frac{1}{2}(d_o - g(m))^T C_D^{-1}(d_0 - g(m)) \tag{3.13}$$

where d_0 is the data vector (Bouguer anomaly from ICGEM (Barthelmes and Köhler, 2016) in the gravity resampling and InSAR data from Fialko and Pearse (2012) in the thermomechanical resampling). $g(m)$ are the model results (Bouguer anomalies in the gravity resmapling and surface velocities projected into LOS in the thermomechanical resampling) and C_D^{-1} is the inverse of the covariance matrix.

$$C_D^{-1} = \frac{1}{\sigma^2} I_n \tag{3.14}$$

where σ is the standard error and I_n is the identity matrix. We use $\sigma_{gravity} = 50$ and $\sigma_{thermomechanics} = 0.5$. For the last step, we then generate a second uniformly distributed random number $r \in [0, 1]$ and if $r \leq \alpha$ the proposal is accepted and added to the selection. Otherwise, the proposal is rejected and a new one is generated.

3.F Supplementary tables and figures

TABLE 3.F.1: Material parameters

Material	Top	Bottom	$\rho\,[\frac{\mathrm{kg}}{\mathrm{m}^3}]$	$V_s\,[\frac{\mathrm{km}}{\mathrm{s}}]$	G [GPa]	$B_n\,[\mathrm{MPa}^{-\mathrm{n}}\,\mathrm{s}^{-1}]$	E_n [kJ]	n
Sediments	Surface	0	2550	2.80	20	3.2×10^{-4}	154	2.3
Upper Crust	0	15	2700	3.35	30	3.2×10^{-4}	154	2.3
Middle Crust	15	35	2880	3.55	35	1.4×10^{-4}	445	4.2
Lower Crust	35	Moho	2930	3.75	40	8.0×10^{0}	485	4.7
Mantle	Moho	80	3320	4.40	65	2.5×10^{4}	532	3.5
Dacite	APMB	15	2575	2.25	15	$\eta = 10^{19}$ Pas		
Andesite	15	APMB	2755	2.45	15	$\eta = 10^{18}$ Pas		

Top and Bottom are in km below sea level. Surface is between 0.5 and 4 km above sea level and Moho is between 40 and 65 km below sea level.
V_s is an average value from Ward et al. (2017) and shear modulus G is computed from V_s.
Creep parameters (B_n, E_n, n) are chosen after Ranalli (1995) (Sediments: Wet Quarzite, Upper Crust: Wet Quarzite, Middle Crust: Mafic Granulite, Mantle: Dry Olivine) and Mackwell et al. (1998) (Lower Crust: Dry Diabase).

TABLE 3.F.2: Dry lava composition after Sparks et al. (2008).

Oxide	Dacite	Andesite
SiO_2	64.26	59.34
TiO_2	1.18	1.18
Al_2O_3	16.29	17.45
Fe_2O_3	5.49	6.98
MnO	0.07	0.10
MgO	2.30	4.46
CaO	4.24	6.37
Na2O	2.26	1.75
K2O	3.60	2.07
P_2O_5	0.30	0.26
SO_3	0.01	0.05
Total	100.00	100.00

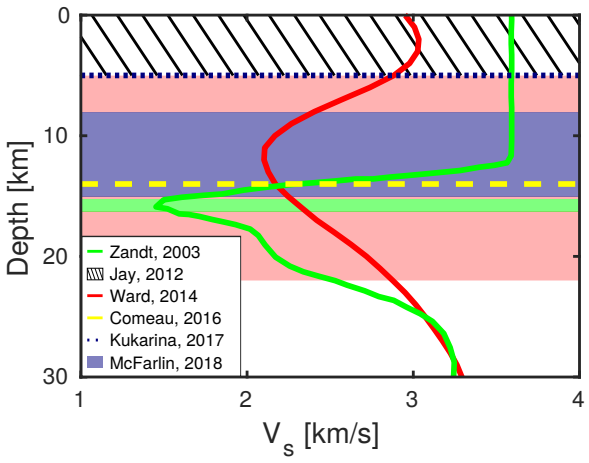

FIGURE 3.F.1: Constraints on APMB extent beneath Uturuncu (colors match the same studies as in Figure 3.1). Red line shows an average V_s-profile beneath Uturuncu summit $\pm$ 0.3° from Ward et al. (2014). Green line shows the average V_s-profile from Zandt et al. (2003). Corresponding colored areas show the extent of the APMB beneath Uturuncu, suggested by these 2 studies. Purple area represents McFarlin et al. (2018). Dashed yellow line shows the top of the APMB according to Comeau et al. (2015) and Comeau et al. (2016). Dotted dark blue line shows the top of the 'Tooth-anomaly' from Kukarina et al. (2017). Hatched area shows estimates for the brittle-ductile transition zone (BDTZ) from Jay et al. (2012).

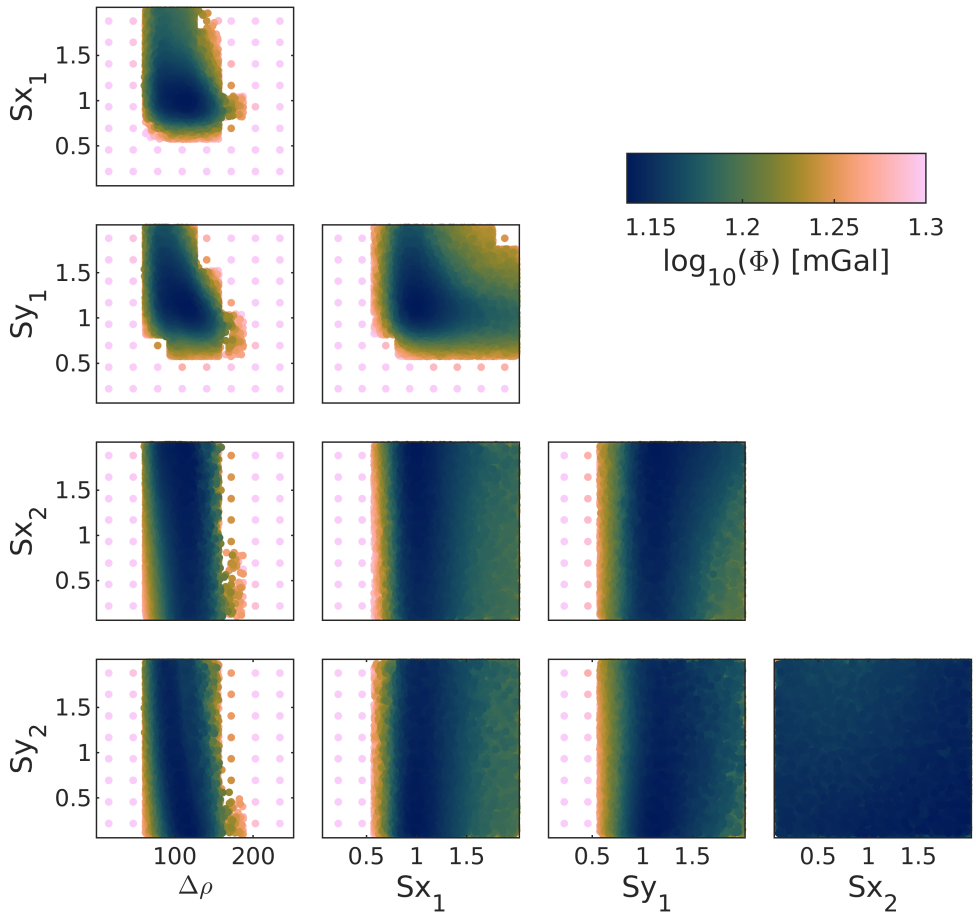

FIGURE 3.F.2: Bouguer anomaly misfit (Φ) in dependence of all sets of 2 parameters. Sx_2 and Sy_2 show no correlation with any of the other parameters.

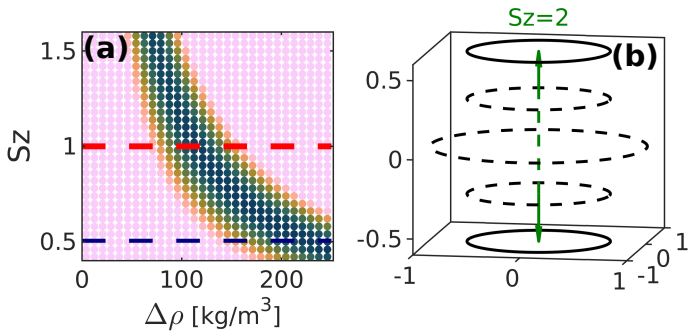

FIGURE 3.F.3: (a) Bouguer anomaly misfit (Φ) in dependence of density contrast $\Delta\rho$ and vertical stretch factor S_z. Same colorbar as in Figure 3.F.2. Dashed red line shows where the APMB suggested by Ward et al. (2014) would plot and dashed blue line shows where APMB suggested by McFarlin et al. (2018) would plot (Figure 3.F.1). (b) Sketch to show how Sz changes the location of polygons in vertical direction (dashed = original, solid = new, note that the central polygon stays unchanged as it is the in the center of mass).

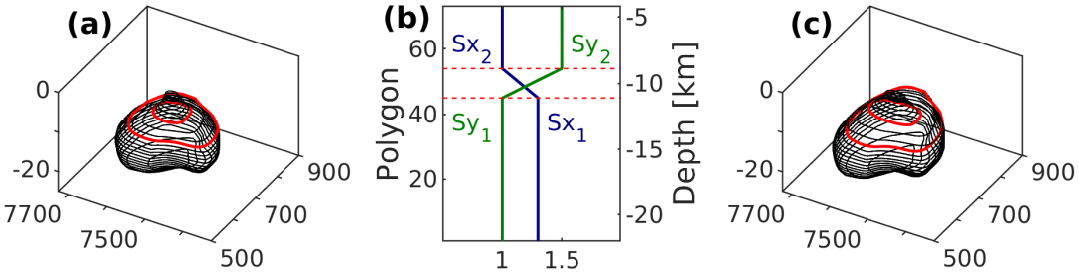

FIGURE 3.F.4: (a): Our reference model of the APMB as horizontal slices. Two red slices are control polygons. Axes show coordinates in km. (b): Example of how stretch parameters are computed and how they are associated with polygons and depth below sea level. Blue line shows Sx and green line shows Sy. Dashed red lines indicate position of control polygons. (c): APMB after application of the example stretch parameters in b. Note that the lower part of the body has been extended in x(EW)-direction and the upper part in y(NS)-direction.

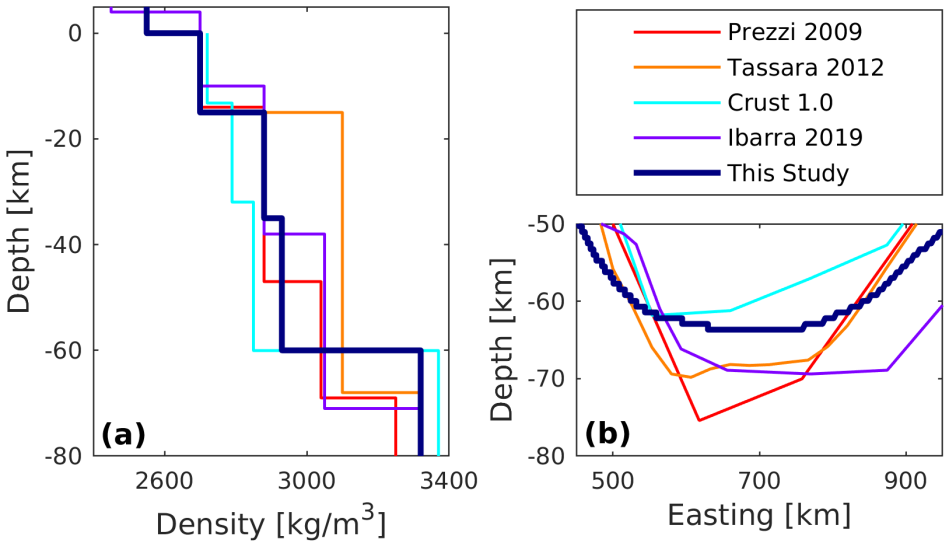

FIGURE 3.F.5: (a): Compilation of models for the lithosphere beneath Uturuncu. Prezzi et al. (2009), Tassara and Echaurren (2012), and Ibarra et al. (2019) use rock chemistry and gravity modeling for their density estimates while the Crust 1.0 model (Laske et al., 2013) uses p-wave velocities. (b): Depth of the Moho along the profile in Figure 3.3 according to the models shown a, including the Moho used in the initial geometry of this study.

Chapter 4

Quantification of volcano deformation caused by volatile accumulation and release

This chapter has been published in:
Spang, A., Burton, M., Kaus, B. J. P. & Sigmundsson, F. (2022). Quantification of volcano deformation caused by volatile accumulation and release. *Geophysical Research Letters, 49*, e2021GL097502. http://doi.org/10.1029/2021GL097502

Abstract

Crustal-stored magma reservoirs contain exsolved volatiles which accumulate in the reservoir roof, exerting a buoyancy force on the crust. This produces surface uplift and sudden loss of volatiles through eruption results in syn-eruptive subsidence. Here, we present three-dimensional, visco-elasto-plastic, numerical modeling results which quantify the ground deformation arising from the growth and release of a volatile reservoir. Deformation is mostly independent of crustal thermal distribution and volatile reservoir shape, but is a function of volatile volume, density and depth and crustal rigidity. We present a scaling law for the volatiles' contribution to syn-eruptive subsidence and show this contributes ∼20% of the observed subsidence associated with the 2015 Calbuco eruption. Our results highlight the key role that volatile-driven buoyancy can have in volcano deformation, show a new link between syn-eruptive degassing and deflation, and highlight that shallow volatile accumulation and release may have a significant impact on ground deformation of volcanoes.

Plain language summary

Magma contains a lot of gases which separate from it when it approaches the surface. These gases can collect right above the magma storage region a few kilometers below the surface. They have a much lower density than the rocks surrounding them and push upwards like a balloon filled with air that is pressed under water. In this study, we use computer models to understand how much a volcano would grow from the push of the gases below and how much it would shrink when the gases escape because of an eruption. We find that the gases can cause the volcano to grow and shrink up to a few centimeters during accumulation and release, respectively. The amount of surface movement depends on the volume, density and depth of the gas reservoir as well as on the toughness of the rocks above it. We derive a simple equation which

allows us to compute the surface movement using the aforementioned parameters. With this equation and estimates about the amount of accumulated gas at the 2015 Calbuco eruption, we can assume that about 20% of the observed surface movement was caused by the release of the magmatic gases.

4.1 Introduction

Volcano deformation is most frequently interpreted in terms of models of surface deformation due to processes in magma bodies of various geometries. The most widely applied model is that of a point source of pressure embedded within a uniform elastic halfspace (Mogi, 1958), but a range of more advanced models and approaches exist (e.g., Fialko et al., 2001a; Hickey et al., 2016). As liquid magma flows in/out of the these "deformation sources", they expand/contract. Most often, such magma flow is considered to cause uniform pressure change on the boundary of the magma body, and the density difference between magma and host rock is not considered specifically. It has, however, been demonstrated in a number of studies that magma buoyancy can cause significant stresses in volcano roots and contribute to failure of magma bodies (e.g., Sigmundsson et al., 2020). A particular phenomena not considered by traditional volcano deformation models is the effect of accumulated exsolved volatiles in volcano roots and their release during eruptions.

During major explosive eruptions an excess of gas may be observed, beyond that which can be explained by a petrological calculation of the original dissolved volatile amounts and the volume of erupted lavas. Excess gas was observed in the 1991 eruption of Pinatubo, Philippines and an analysis from Wallace and Gerlach (1994) showed that this could be explained by a pre-existing gas/volatile phase representing 0.7 to 1.3 wt% of the erupted magma. Volatile accumulation was proposed to occur in the roof zone of the system. On 22 April 2015, the Chilean volcano Calbuco produced a sub-Plinian eruption (Castruccio et al., 2016; Romero et al., 2016; Arzilli et al., 2019) with two explosive phases. The first was found to be powered by an excess gas phase with three times the amount of SO_2 estimated to be produced by the erupted mass (Pardini et al., 2018). In highly silicic systems, the volume of erupted products may be only a fraction of the magma reservoir volume, as eruptible magma is extracted from a large crystal mush (e.g., Bachmann and Bergantz, 2004). This creates the possibility that a voluminous volatile body is created within magmatic systems prior to eruption, ponding in the roof zone, producing both observed excess gas and a buoyancy force on the crust, arising from the volatiles' lower density ($\sim$ 500 $\mathrm{kg\,m^{-3}}$) compared with melt and crust. At a depth of 8 km and pressure of 200 MPa, the solubility of CO_2 in a basalt is $\sim$ 700 ppm (Newman and Lowenstern, 2002), while the initial CO_2 contents may be 1 wt% (10,000 ppm) or greater (Blundy et al., 2010). So a significant free volatile phase can be expected in magma reservoirs if the volatiles exsolve but cannot escape to the surface. The purpose of this study is to examine the impact of the sudden release of a large volume of exsolved volatiles and the associated loss of buoyancy to estimate the significance of this process for volcano deformation modeling.

To do that, we utilize the three-dimensional (3D) thermomechanical finite differences code LaMEM (Kaus et al., 2016) to model the stresses and deformation that a sudden change in the density field induces in the overlying crust and at the surface. LaMEM solves the density dependent Stokes equations for (nearly) incompressible visco-elasto-plastic fluid flow and runs on massively parallel clusters, allowing us to

use high resolutions, even in 3D. The code has already been applied to magmatic systems before (e.g., Reuber et al., 2018; Piccolo et al., 2020; Spang et al., 2021).

4.2 Methods

Section 4.2.1 introduces the software used for modeling as well as the physics and governing equations. Section 4.2.2 presents the model setup and the parameters used. Details on model resolution, time stepping and resolution tests are presented in supplementary text 4.B. Section 4.2.3 describes the key parameters that we identified and our approach to deriving a scaling law for the surface deformation due to volatile release. In section 4.2.4, we introduce our area of application, the Chilean volcano Calbuco.

4.2.1 Thermomechanical code

The 3D thermomechanical finite differences code LaMEM (Kaus et al., 2016) was used to calculate deformation due to magmatic sources hosted in a finite-size model domain. The code solves for the conservation of momentum, mass and energy (eq. 4.1-4.3), using a staggered grid in combination with a marker-in-cell approach (Harlow and Welch, 1965).

$$\frac{\partial \tau_{ij}}{\partial x_j} - \frac{\partial p}{\partial x_i} + \rho g_i = 0 \tag{4.1}$$

$$\frac{\partial v_i}{\partial x_i} = 0 \tag{4.2}$$

$$\rho C_p \frac{DT}{Dt} = \frac{\partial}{\partial x_i}\left(k \frac{\partial T}{\partial x_i}\right) + H \tag{4.3}$$

τ_{ij} is the Cauchy stress deviator, $x_i (i = 1, 2, 3)$ denotes the Cartesian coordinates, p is pressure (positive in compression), ρ density, g_i gravitational acceleration, v_i the velocity vector, C_p the specific heat capacity, T the temperature, k the thermal conductivity, H the volumetric heat source and D/Dt is the material time derivative.

Free slip conditions are applied to the boundaries of the model domain, allowing movement parallel to the domain edges while setting perpendicular velocities to 0. At the top of the setup, we include 1 km of sticky air above the stabilized free surface (Duretz et al., 2011; Kaus et al., 2010). The rocks are characterized by a temperature- and strain rate-dependent visco-elasto-plastic rheology where the strain rate is the sum of the elastic, viscous and plastic components:

$$\dot{\epsilon}_{ij} = \dot{\epsilon}^{el}_{ij} + \dot{\epsilon}^{vi}_{ij} + \dot{\epsilon}^{pl}_{ij} \tag{4.4}$$

$\dot{\epsilon}_{ij}$ denotes the total deviatoric strain rate tensor, while $\dot{\epsilon}^{el}_{ij}$, $\dot{\epsilon}^{vi}_{ij}$ and $\dot{\epsilon}^{pl}_{ij}$ represent the elastic, viscous and plastic strain rate components. A detailed discussion of this equation and all of its components is given by Kaus et al. (2016), but here we will focus on the material parameters which impact the three components.

The elastic component $\dot{\epsilon}^{el}_{ij}$ is inverse proportional to the shear modulus G:

$$\dot{\epsilon}^{el}_{ij} = \frac{1}{2G} \frac{D\tau_{ij}}{Dt}, \tag{4.5}$$

where $D\tau_{ij}/Dt$ corresponds to the objective derivative of the stress tensor.

The viscous strain rate component $\dot{\epsilon}_{ij}^{vi}$ is governed by the viscosity η, which follows the temperature- and strain rate-dependent powerlaw relationship of dislocation creep:

$$\eta = \frac{1}{2}(B_n)^{-\frac{1}{n}}(\dot{\epsilon}_{II})^{\frac{1}{n}-1}\exp\left(\frac{E_n}{nRT}\right), \tag{4.6}$$

where B_n is the creep constant, $\dot{\epsilon}_{II}$ the square root of the second invariant of the strain rate ($\dot{\epsilon}_{II} = (\frac{1}{2}\dot{\epsilon}_{ij}\dot{\epsilon}_{ij})^{1/2}$), E_n the activation energy, n the powerlaw exponent, R the universal gas constant and T the temperature.

The plastic component is characterized by the Drucker-Prager failure criterion (Drucker and Prager, 1952) which is a good approximation of Byerlee's law (Byerlee, 1978):

$$\tau_{II} \leq \sin(\phi)p + \cos(\phi)c_0 \tag{4.7}$$

τ_{II} is the square root of the second invariant of the stress tensor ($\tau_{II} = (\frac{1}{2}\tau_{ij}\tau_{ij})^{1/2}$), ϕ is the friction angle, p the pressure and c_0 the cohesion. Equation 4.7 describes how much stress can be accommodated with visco-elastic deformation.

As buoyancy is the driving force in our model, we need densities to be independent of temperature (i.e. no thermal expansion) and pressure (i.e. incompressible). For the volatile reservoir, we use the ideal gas law to estimate density (see supplementary text 4.C).

4.2.2 Model setup and parameter selection

Obtaining a quantitative understanding of ground deformation requires the use of 3D models, but as they are computationally expensive, we do initial testing in 2D which allows an efficient evaluation of the respective importance of various model parameters.

Our reference model (Figure 4.1a) uses a homogeneous crust, hosting a spherical, low-viscosity, non-buoyant magma reservoir with a radius of 1 km. As exsolved volatiles are expected to accumulate in the roof of the magmatic system, we approximate the volatile reservoir as a sphere (r = 250 m) of low density, viscosity and rigidity on top of the magma body. We use a non-buoyant magma body to focus on the volatiles' contribution to surface deformation. It still provides heat to the surrounding host rock and mechanically decouples the volatile reservoir from the underlying crust.

To approximate the release of the exsolved volatiles from the system during eruption, they are instantaneously replaced by non-buoyant magma after 20 years (the time of eruption in the model). This is accomplished by copying the material properties (density, viscosity and shear modulus) of the magma onto the volatile particles. The change in density induces a change in crustal stresses (see equation 4.1, supplementary Figure 4.F.1).

In reality, an eruption does not only remove the buoyancy forces of the volatile reservoir but also the volatiles themselves as well as part of the magma. As magma injection is a commonly suggested trigger for eruptions (Canon-Tapia, 2014), the erupted volume may be replaced by intruding magma from a deep source. If this is not or only partly the case, the loss of volume leads to a depressurization of the remaining magma reservoir. This likely triggers a combination of three processes. (i) The remaining magma exsolves more volatiles due to the drop in confining pressure which expand upon exsolution. (ii) The magma itself expands due to depressurization. (iii) The overburden subsides and contracts to close the space left behind. All of these processes influence surface deformation alongside the loss of buoyancy, but as the

contribution of each of the three aforementioned processes and magma injection is not understood, we focus on the change in buoyancy forces. This way, we can constrain the magnitude of this individual contributor to syn-eruptive subsidence and estimate whether it is significant.

Supplementary table 4.F.1 shows the parameters we use for the different model materials. The rheology of the crust follows the powerlaw relationship of dislocation creep of wet quartzite (Ranalli, 1995) while magma and volatile reservoir are linear visco-elasto-plastic. We use a shear modulus of 2 GPa, in line with upscaled values from laboratory experiments on volcanic rocks (Heap et al., 2020). Cohesion and friction angle of intact rocks are typically estimated in the range of a few MPa and 30° respectively (Hoek and Brown, 1997), so we use 5 MPa and 20° for the presumably pre-damaged crust of a magmatic system. The thermal conductivity is 3 $\mathrm{W\,(m\,K)^{-1}}$ and the heat capacity 1000 $\mathrm{J\,(mol\,K)^{-1}}$ for all materials. We employ a background thermal gradient of 30 $\mathrm{K\,km^{-1}}$ and set the initial temperature of volatiles and magma to 800 °C. Before we start the mechanical model (t = 0), we allow for 50 kyr of thermal diffusion to account for the heated crust around a magma body which we keep at a constant temperature during this heating phase.

4.2.3 Scaling law for deflation

Through initial testing, we identified four key parameters that influence the ground deformation (Figure 4.1b). The radius of the volatile reservoir (r_{vol}), the depth of the volatile reservoir (d_{vol}), the density contrast between volatiles and crust ($\Delta\rho$) and the shear modulus of the crust (G_{crust}). In both 2D and 3D, we run a set of systematic parameter combinations to derive a scaling law for the deflation at the surface due to the volatile removal. For each parameter, we test 5 (9 for d_{vol}) different values while keeping the others constant.

4.2.4 Calbuco

The Chilean stratovolcano Calbuco erupted on April 22, 2015 and interferometric analysis of synthetic aperture radar images (InSAR analysis) from the Sentinel-1 satellites revealed a co-eruptive subsidence of about 12 cm (Nikkhoo et al., 2016; Delgado et al., 2017). Using different analytical solutions, Nikkhoo et al. (2016) and Delgado et al. (2017) reproduce the surface deformation with deflating sources at a depth of around 8 km. Petrological estimates for the location of the magma storage zone range from 5.5 to 12 km depth (Morgado et al., 2019; Arzilli et al., 2019; Namur et al., 2020). Namur et al. (2020) also suggest that magma moved to shallower levels weeks or month prior to eruption.

Pardini et al. (2018) found that a pre-existing volatile phase must have been present to explain $1.5 \cdot 10^8$ kg of excess SO_2 produced by the Calbuco eruption. Assuming a typical arc-magma H_2O abundance of 3 wt% (100 times the SO_2 content (Pardini et al., 2018)), we expect that this pre-exsolved volatile phase would contain $1.5 \cdot 10^{10}$ kg of H_2O (Spilliaert et al., 2006). CO_2 is much less soluble than H_2O or SO_2 and therefore to calculate the pre-eruptive CO_2 content we conservatively estimate that the total mass of the magma reservoir was ten times (Annen et al., 2008) the erupted mass of $4.9 \cdot 10^{11}$ kg (Pardini et al., 2018). Assuming that 0.5–1.5 wt% of CO_2 (Blundy et al., 2010) was exsolved prior to eruption leads to pre-exsolved CO_2 masses of $2.5 \cdot 10^{10}$–$7.4 \cdot 10^{10}$ kg. We therefore estimate that the total pre-exsolved gas mass was $3.9 \cdot 10^{10}$–$8.8 \cdot 10^{10}$ kg. We consider two scenarios, with volatiles stored at

5.5 km and 8 km depth and use the ideal gas law and lithostatic pressure to estimate the density of the volatile reservoir (see supplementary text 4.C).

4.3 Results

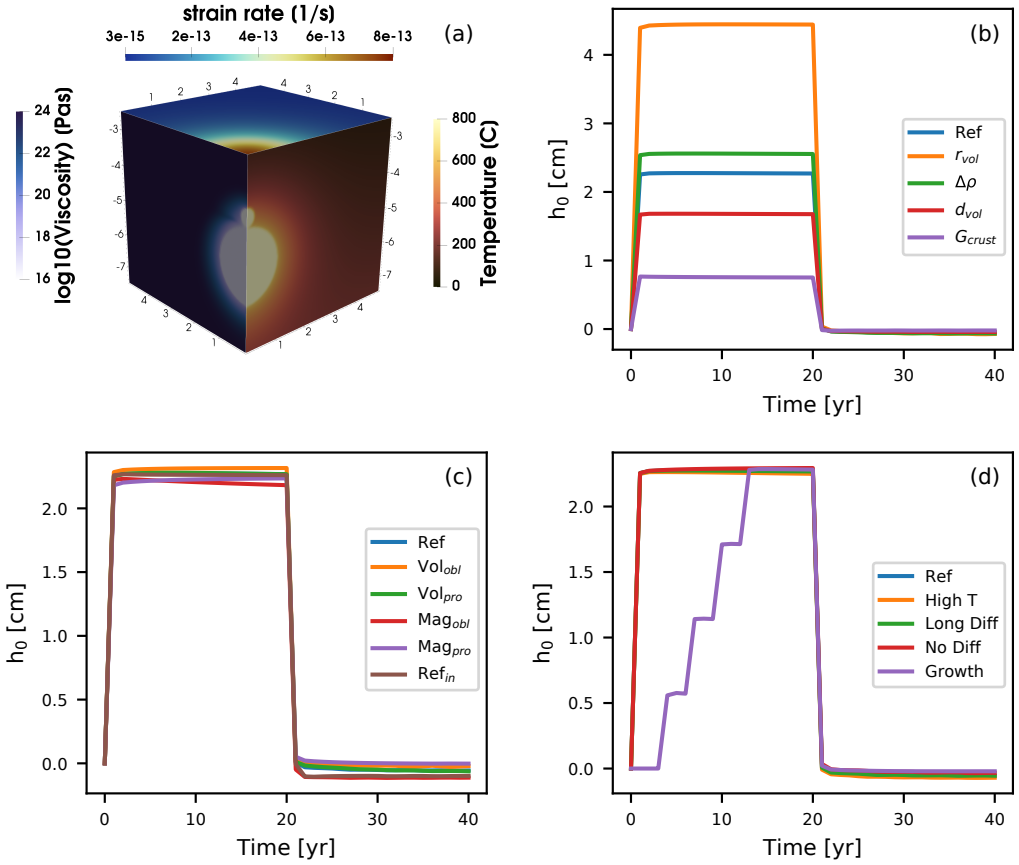

FIGURE 4.1: (a) Zoomed in part of 3D model setup showing the viscosity on the left panel, temperature on the right panel, and strain rate on the top panel before the release of the volatiles. The 2D setup is a slice along the boundary of the 3D model. 2D and 3D model both extend 50 km in lateral and 15 km in vertical direction but those parts of the figure were cut to enlarge the relevant features. Axes are in km. (b-d) Surface level directly above the sources calculated in 3D models. (b) Effect of perturbing one crucial material parameter compared to the reference model. (c) Effect of changing the shape of the magma and volatile reservoir in comparison to reference model. Subscript $_{obl}$ means oblate, subscript $_{pro}$ means prolate. The volume was preserved in all cases. $\mathrm{Ref_{in}}$ corresponds to a model where the volatile reservoir is placed inside the magma body. (d) Effect of changing the temperature structure in the crust through higher reservoir temperature or longer/no initial diffusion time. See section 4.3.2 for details. 'Growth' corresponds to a model where the volatile reservoir incrementally increases in size.

Section 4.3.1 describes the general behavior of the model and discusses dependencies on time stepping and size of the model domain. In section 4.3.2, we discuss the effects of changing the geometry of the magma body and volatile reservoir as well as the thermal structure of the crust. Section 4.3.3 describes the derivation of the scaling law in 3D. The 2D is scaling law is discussed in supplementary text 4.D and the

differences between 2D and 3D in supplementary text 4.E. In section 4.3.4 we apply the scaling law derived in section 4.3.3 to the case of the 2015 Calbuco eruption.

4.3.1 General behavior

At the start of each simulation, the surface above the buoyant volatile reservoir undergoes immediate uplift, and quickly (within 2 time steps) reaches a steady state. Upon, replacing the volatiles with non-buoyant magma (i.e. an eruption), the surface quickly (within 2 time steps) returns to the original level. Independently of the time step we employ (0.1 - 10 years), the surface reaches the same level after 2 steps with the first step being very close to it already (Figures 4.F.2c and 4.F.3d). We observe the same behavior after removing the volatile reservoir. We therefore conclude that the surface response is immediate and has no time dependence. The small adjustment, necessary in the second time step, is inferred to be of numerical origin. To minimize computational cost and enable us to observe any potential time dependencies, we use a time step of 1 year for all our models. In reality, the uplift or inflation phase may take place over a long time as the volatile reservoir grows gradually, but will reach the same magnitude as in our models. Volcano deflation, however happens on timescales of eruptions as all volatiles are expected to reach the surface, once a pathway has been established.

Supplementary figures 4.F.2d and 4.F.3c show that the surface displacement depends on the width of the model domain. The displacement increases with increasing model width but at 50 km width, the effect levels off. We therefore ran all models with a width of 50 km.

We do not observe plastic failure in any of our models. Even after reducing cohesion (c_0) by an order of magnitude to 0.5 MPa and friction angle (ϕ) to 10° while increasing r_{vol} to 500 meters and G_{crust} to 10 GPa to maximize crustal stresses, stresses due to changes in buoyancy never exceed a few MPa which is insufficient to exceed the Drucker-Prager failure criterion.

4.3.2 Influence of source geometry and thermal structure

In Figure 4.1c, we show the results of testing different shapes for the magma and volatile reservoirs. Both the oblate and prolate shapes have an aspect ratio of 2 while preserving the volume of the spherical version. None of the geometrical variations lead to a significant difference in vertical displacement. Immersing the lower half or the entire volatile reservoir in the top of the magma body does not have significant effects either (Figure 4.1c).

Figure 4.1d shows the effect of changing the thermal structure of the crust. In the 'No Diff' example, we omit the 50 ka of thermal diffusion and start with a crust that only has the background temperature gradient while in the 'Long Diff' example, we double the temperature diffusion time from 50 to 100 ka. For the 'High T' example, we set the magma and volatile temperature to 1000 °C instead of 800 °C. The surface response is almost identical with the reference model for all cases.

4.3.3 3D scaling law

Figure 4.1b shows the effect of varying four material parameters that have a considerable effect on the surface response. The radius and depth of the volatile reservoir (d), the density contrast between volatiles and crust ($\Delta\rho$) and the shear modulus of the crust (G). We performed a systematic parameter variation, testing 5 different values for each parameter (9 for d_{vol}) while keeping the other parameters constant.

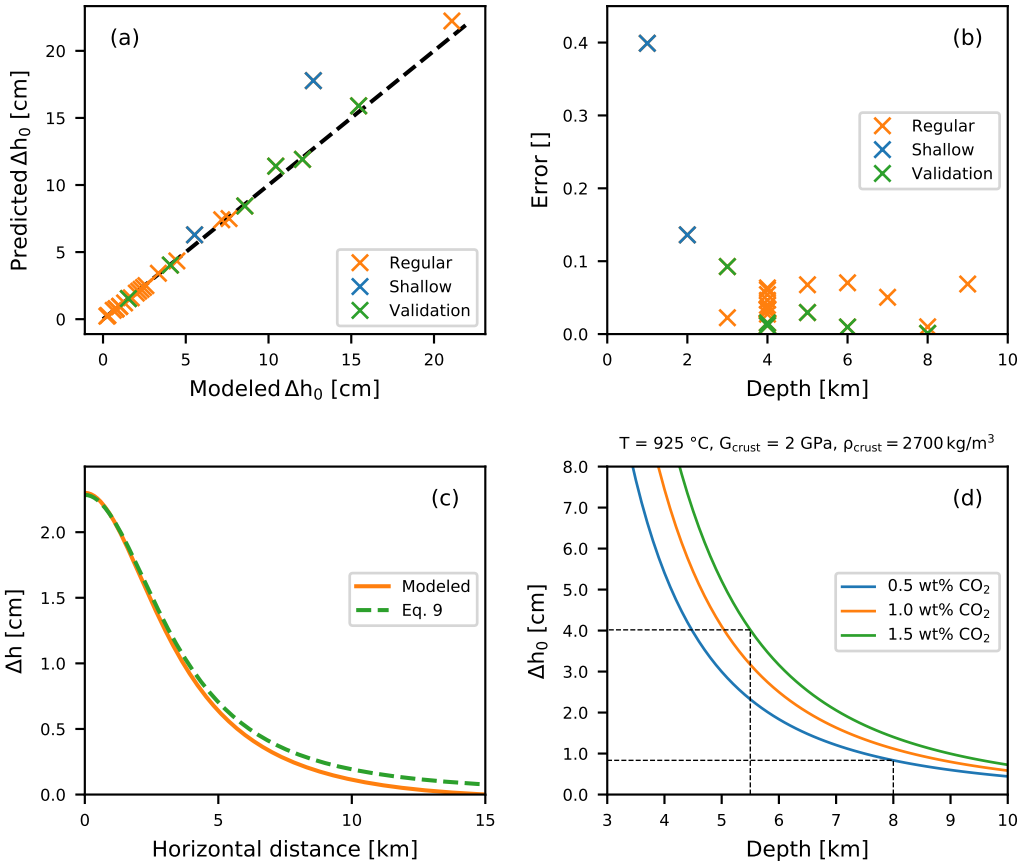

FIGURE 4.2: (a) Comparison between modeled subsidence and subsidence predicted by equation 4.8. Black dashed line shows 1:1 correlation. Orange crosses show models that were used to derive equation 4.8 and green crosses show models used to validate the scaling law. Blue crosses show models with a shallow (<= 2 km) volatile reservoir that were excluded. (b) Error between the modeled subsidence and the predicted subsidence as a function of depth. (c) Subsidence along a radial profile for the reference case in orange in comparison to the prediction made by equation 4.9. Offset at the edge is due to the boundary conditions of the model as the uplift in the center needs to be balanced by subsidence along the edges. (d) Coupling between the ideal gas law and equation 4.8 to show the full dependence of maximum subsidence Δh_0 on reservoir depth d. Solid lines denote different volatile mass estimates as discussed in section 4.2.4. Dashed black lines show how we determine the minimum and maximum of subsidence in section 4.3.4.

Supplementary figure 4.F.6 shows the results for individual parameters. From this, we are able to derive the following scaling relationship:

$$\Delta h_0 = A \frac{r^3 \, \Delta\rho \, g}{d^{3/2} \, G} \tag{4.8}$$

where Δh_0 is the vertical displacement at the surface above the source, g is the gravitational acceleration and A is a pre-factor of $12\,\pi$ with units of $\mathrm{m}^{0.5}$ to satisfy the equation. The scaling law is similar to the one derived for the 2D case with the only exception being the exponents of r and d (see equation 4.14). Fits for the individual parameters are shown in Figure 4.F.6.

Figure 4.2a shows how equation 4.8 predicts the results of the 3D models and Figure 4.2b shows the error which is generally smaller than 10%. Green crosses in Figures 4.2a and 4.2b show models where we changed multiple parameters to validate equation 4.8. Subsidence in models with a shallow ($d <= 2\,km$) volatile reservoir are overestimated. Analytical solutions for the gravity anomaly of buried cylinders or spheres have the same issue of only being applicable when the depth of the body is much larger than its radius (Turcotte and Schubert, 2002). The same is true for simple models relating the inflation of magma bodies to surface deformation (e.g., Mogi, 1958; Yang et al., 1988).

Equation 4.8 only describes the vertical displacement directly above the center of the volatile reservoir. Figure 4.2c shows a profile of the vertical change along the surface. Our numerical models show that we can modify equation 4.8 to:

$$\Delta h(x) = A \frac{r^3 \, \Delta\rho \, g}{G} \frac{d}{(d^2 + x^2)^{5/4}} \tag{4.9}$$

where x is the horizontal distance from the center of the volatile reservoir projected to the surface. Figure 4.2c shows that the modeled surface displacement is fit well by equation 4.9. In this form, our scaling law is very similar to the analytical solution of ground deformation due to a point source of pressure within an elastic halfspace, the "Mogi model" (Mogi, 1958). The most notable difference being the exponent of 5/4 instead of 3/2, which stems from the depth dependence of $\frac{1}{d^{3/2}}$ (see equation 4.8 and supplementary Figure 4.F.6c) while the "Mogi model" has a depth dependence of $\frac{1}{d^2}$.

4.3.4 Calbuco

For Calbuco, we use equation 4.8 with $\rho_{\mathrm{crust}} = 2700\,\mathrm{kg\,m^{-3}}$ and $\mathrm{G_{crust}} = 2\,\mathrm{GPa}$ to predict a maximum surface subsidence of 4 cm due to the loss of buoyancy from $8.8 \cdot 10^{10}$ kg of exsolved volatiles for the case of storage at 5.5 km depth. For the 8 km depth scenario, and a lower limit estimate of the erupted gas mass ($3.9 \cdot 10^{10}$ kg), we predict 1 cm. Equations 4.8 and 4.9 imply that the surface displacement depends on the reservoir depth to the power of 1.5. In reality, r and $\Delta\rho$ are also functions of the pressure in the volatile reservoir and thereby of the depth. Figure 4.2d illustrates this nonlinear dependence and shows how we arrive at our minimum and maximum estimates.

4.4 Discussion

4.4.1 Rheology

Given that, even for rocks with considerably lowered plastic strength, the stresses caused by the changes in buoyancy are not sufficient to exceed the failure criterion,

plasticity is not a relevant factor in our models. Figure 4.1d also suggests that on the timescales of an eruption, viscous components have no impact on the deformation, even with the weakening caused by heating of the crust. The process of surface subsidence caused by the loss of a buoyant volatile reservoir due to eruption can therefore be considered as quasi-elastic, and as a result it is possible to derive a scaling law for the problem.

4.4.2 Surface subsidence due to buoyancy loss

Instantly (on the timescale of an eruption) removing the buoyancy forces, exerted by a volatile reservoir, from the top of an upper crustal magma body leads to an instantaneous subsidence. The magnitude of subsidence decays with radial distance from the reservoir center, but is significant in a radius of several kilometers (Figure 4.2c). The surface response is insensitive to the temperature structure (Figure 4.2d) of the crust which allows us to derive a scaling law for the expected subsidence (equations 4.8 and 4.9). As the shape of the volatile reservoir appears to play a minor role (Figure 4.1c), we suggest this alternative form of equation 4.9:

$$\Delta h(x) = \frac{9\,V\,\Delta\rho\,g}{G}\frac{d}{(d^2+x^2)^{5/4}} \tag{4.10}$$

where V is the volume of the volatile reservoir. As other analytical solutions for the surface effects of buried bodies, the scaling law's accuracy decreases when the ratio between radius and depth of the body exceeds 0.1 (Figure 4.2b). The reduction to volume is in line with Archimedes' principle.

The inferred scaling law (equations 4.8, 4.9 and 4.10) has a similar structure to the Mogi model including a pre-factor, a cubic dependence on radius, an elastic property of the crust and a term describing the decay of the signal with distance. One difference is the term of the driving force of deformation. In the Mogi model, it is either a pressure or a volume change, while in our scaling law, it is buoyancy. The other notable difference is the exponent of the depth dependence (2 for Mogi and 1.5 in our model). This could be caused by the different mechanisms that are at work. The pressure point source of the Mogi model applies a pressure to the surrounding crust in all directions, while in our case, buoyancy is expected to exert a cummulative upwards force in line with Archimedes' principle (e.g., Sigmundsson et al., 2020).

Another difference to common scaling laws for volcano deformation (e.g., Mogi, 1958; McTigue, 1987) is the lack of compressibility in our models because of its complex interplay with densities. As vertical displacement is usually multiplied by the term $(1-\nu)$, our scaling law might provide a minimum estimate as a commonly used Poisson's ratio of $\nu = 0.25$ results in a larger factor than incompressibility ($\nu = 0.5$).

4.4.3 Calbuco

Applying our scaling law to the case of the 2015 Calbuco eruption, yields a subsidence of 1–4 cm (Figure 4.2d). With an incidence angle of 33° (Delgado et al., 2017), these vertical velocities can be projected into line-of-sight displacement (Fialko et al., 2001) and represent 7% to 28% of the observed surface deformation. This is an indication that the majority of co-eruptive subsidence was caused by the volumetric loss of material (volatiles and magma) but a significant part of the signal may originate from the loss of buoyancy provided by a body of exsolved volatiles.

In fact, the best-fit sphere and spheroid models of Delgado et al. (2017) have a residual of about 3 cm in the center of subsidence. The mechanism described in our work provides an additional source of uplift, large enough to cover this misfit entirely.

4.4.4 Implications for modeling volcanic deformation

The release of a buoyant body of exsolved volatiles from the top of an upper crustal magma reservoir can lead to significant (on the order of a few cm) syn-eruptive subsidence at the surface. This effect is likely smaller than the effect of volume change in volcanic roots during eruptions as magma moves to the surface. In the case of Calbuco, the contributions may have a ratio between 3:1 and 10:1 in favor of the volume loss. This ratio depends, however, on the quantity of pre-exsolved volatiles.

Adding equation 4.10 to existing models could be a simple way of achieving a better fit to the observed deformation while also providing an explanation for the excess gas that is detected for a number of eruptions.

As Figure 4.1 shows, the presence of a buoyant body of exsolved volatiles also causes surface uplift of the same magnitude as its removal causes subsidence. That means that inflation of a few centimeters over time, which is traditionally interpreted to be a sign of magma intrusion at depth, could also be caused by the formation of a body of exsolved volatiles at the top of the magma reservoir.

Furthermore, magma is usually buoyant at the depth where it intrudes. So even if the intruded magma does not form a significant volatile reservoir, it still exerts a buoyancy force on the crust that adds to the surface deformation caused by displacing host rock. Although the effect of magma buoyancy on surface deformation was not explicitly investigated here, it is likely that equation 4.10 also gives a good estimate of its effect and could be added to existing solutions for surface uplift.

4.5 Conclusions

We conducted a series of 3D visco-elasto-plastic models to investigate the surface deformation caused by the instantaneous removal of buoyancy forces, exerted by a reservoir of exsolved volatiles, from the top of a magma body, as would be the case during an eruption. Our results show that the removal causes subsidence at the surface which is mostly independent of the shape of the volatile and magma reservoirs as well as from the thermal state of the crust. Instead, the process is quasi-elastic, allowing us to derive an analytical solution for the surface subsidence including the volume and depth of the reservoir, the density contrast between volatiles and crust, as well as the shear modulus of the crust. This analytical solution predicts surface deformations on the order of up to a few centimeters.

We applied our scaling law to the case of the 2015 Calbuco eruption and, depending on the depth of the reservoir and volatile mass, predict subsidence of 1–4 cm, which is about 20% of the observed signal. We expect that most of the observed surface deformation is caused by the volume loss of volatiles and magma.

Adding our scaling law to existing models for volcano deformation would present a step forward, towards models that include all the relevant mechanisms that occur in volcanic roots.

4.6 Acknowledgments

The authors thank two anonymous reviewers for their help in improving the quality of the manuscript. This study was funded by the European Research Council through the

MAGMA project, ERC Consolidator Grant # 771143. We thank Fabio Arzilli for his contribution to our estimations of the volatile budget. We used perceptually uniform colormaps to prevent optical data distortion (Crameri, 2018). Parts of this research were conducted using the supercomputer Mogon II and/or advisory services offered by Johannes Gutenberg University Mainz (hpc.uni-mainz.de), which is a member of the AHRP (Alliance for High Performance Computing in Rhineland Palatinate, www.ahrp.info) and the Gauss Alliance e.V..

Supplementary

4.A Open research section

Software for this research is available on zenodo at:
LaMEM (Kaus et al., 2016): https://doi.org/10.5281/zenodo.6538313

4.B Resolution and Time Stepping

To maximize the resolution, we use only one quarter (half for 2D) of the perfectly symmetric domain. Figures 4.F.2a, 4.F.2b and 4.F.3a show that we do not introduce any effects through this simplification. Using 384 cells in each direction yields roughly 56.6 million cells and a vertical resolution of about 40 meters (Figure 4.1a). As the model extends 15 km in the vertical and 50 km in horizontal directions, the horizontal cell size is only 40 meters in the central 2.5 km and then increases towards the horizontal edges of the domain. Resolution tests confirm that this is sufficient (Figures 4.F.2a, 4.F.2b and 4.F.3b). We run the model for 40 years with a constant time step of 1 year. This domain width and time stepping allows the evaluation of reliable models (see section 4.3.1 and Figures 4.F.2c, 4.F.2d, 4.F.3c, 4.F.3d). Figure 4.1d shows that emplacing the full volatile reservoir at once or incrementally increasing its size results in the same surface response.

4.C Volatile volume and density

We use the ideal gas law to estimate the volume of the volatile reservoir:

$$V = \frac{nRT}{p} \tag{4.11}$$

V is the volume, n the amount of substance, R the universal gas constant, T the temperature and p the pressure. n is calculated by

$$n = \frac{m}{M}, \tag{4.12}$$

where m is the total volatile mass and M is the average molar mass of the volatile mixture. Finally, we calculate density ρ by:

$$\rho = \frac{m}{V}. \tag{4.13}$$

4.D 2D scaling law

Figure 4.F.4b shows four material parameters that have a considerable effect on the surface response. The radius of the volatile reservoir (r_{vol}), the depth of the volatile reservoir (d_{vol}), the density contrast between volatiles and crust ($\Delta\rho$) and the shear modulus of the crust (G_{crust}). We performed a systematic parameter variation, testing

5 different values for each parameter (9 for d_{vol}) while keeping the other parameters constant. Figure 4.F.5 shows the results for individual parameters. From this, we are able to derive the following scaling relationship:

$$\Delta h_0 = A\frac{r^2\,\Delta\rho\,g}{d\,G}, \tag{4.14}$$

where Δh_0 is the predicted subsidence upon volatile removal, A is a pre-factor with units of meters, r is the radius of the volatile reservoir, $\Delta\rho$ is the density contrast between volatiles and crust, g is the gravitational acceleration, d is the depth of the volatile reservoir and G the shear modulus of the crust. Figure 4.F.4c shows that the scaling law is able to predict the modeling results as well as 24 additional cases where multiple parameters were varied and that were not used in deriving the law. The error is on the order of 10% or lower for the majority of cases. Exceptions are models with a shallow volatile reservoir ($r\,/\,d > 0.1$, blue in Figure 4.F.4d). Analytical solutions for the gravity anomaly of buried cylinders or spheres have the same issue of only being applicable when the depth of the body is much larger than its radius (Turcotte and Schubert, 2002). The same is true for simple models relating the inflation of magma bodies to surface deformation (e.g., Mogi, 1958; Yang et al., 1988).

4.E 2D vs 3D

The surface displacement in our 2D models is larger than in the 3D models by a factor of about 30. This stems from the fact that modeling a sphere in 2D is equivalent to modeling an infinite horizontal cylinder/pipe in 3D. Our study highlights the importance of modeling magmatic systems in 3D. Yet, there are some relevant results that do not change when moving from 2D to 3D. The influence of material parameters $\Delta\rho$ and G as well as the independence of the surface deformation from the reservoir shapes and the temperature structure of the crust did not change when moving to 3D. Consequently, the scaling laws for 2D (equation 4.14) and 3D (equation 4.8) are similar. So 2D models can serve as a good tool for orientation as they are computationally much cheaper and allow to do extensive initial testing. To get quantitative results on finite bodies, it is however critical to use 3D models.

4.F Supplementary tables and figures

TABLE 4.F.1: Material parameters

Material	$\rho\,[\frac{\mathrm{kg}}{\mathrm{m}^3}]$	G [GPa]	$B_n\,[\mathrm{MPa}^{-\mathrm{n}}\,\mathrm{s}^{-1}]$	E_n [kJ]	n
Crust	2500	2.0	3.2 x 10^{-4}	154	2.3
Magma	2500	0.1	$\eta = 10^{18}$ Pas		
Volatiles	500	0.1	$\eta = 10^{16}$ Pas		

Creep parameters (B_n, E_n, n) are chosen after Ranalli (1995)

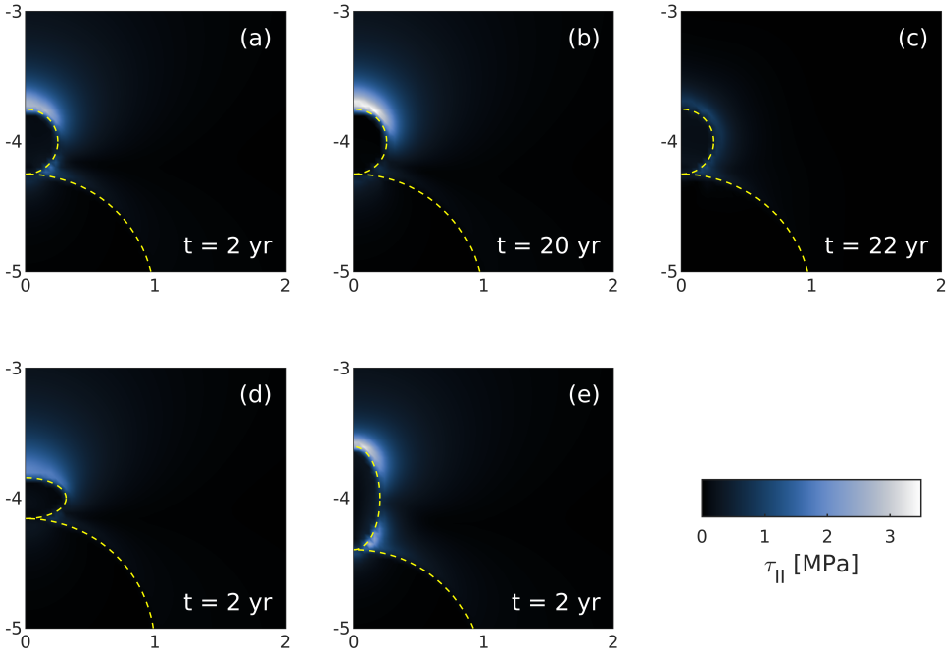

FIGURE 4.F.1: Magnitude of deviatoric stress (τ_{II}) around the volatile reservoir for different time steps and reservoir shapes. Dashed yellow lines follow boundaries of volatile and magma reservoir. (a) Reference model with volatiles emplaced. (b) Reference model right before the eruption. (c) Reference model after the volatiles have been released. (d) Oblate reservoir with volatiles emplaced. (e) Prolate reservoir with volatiles emplaced.

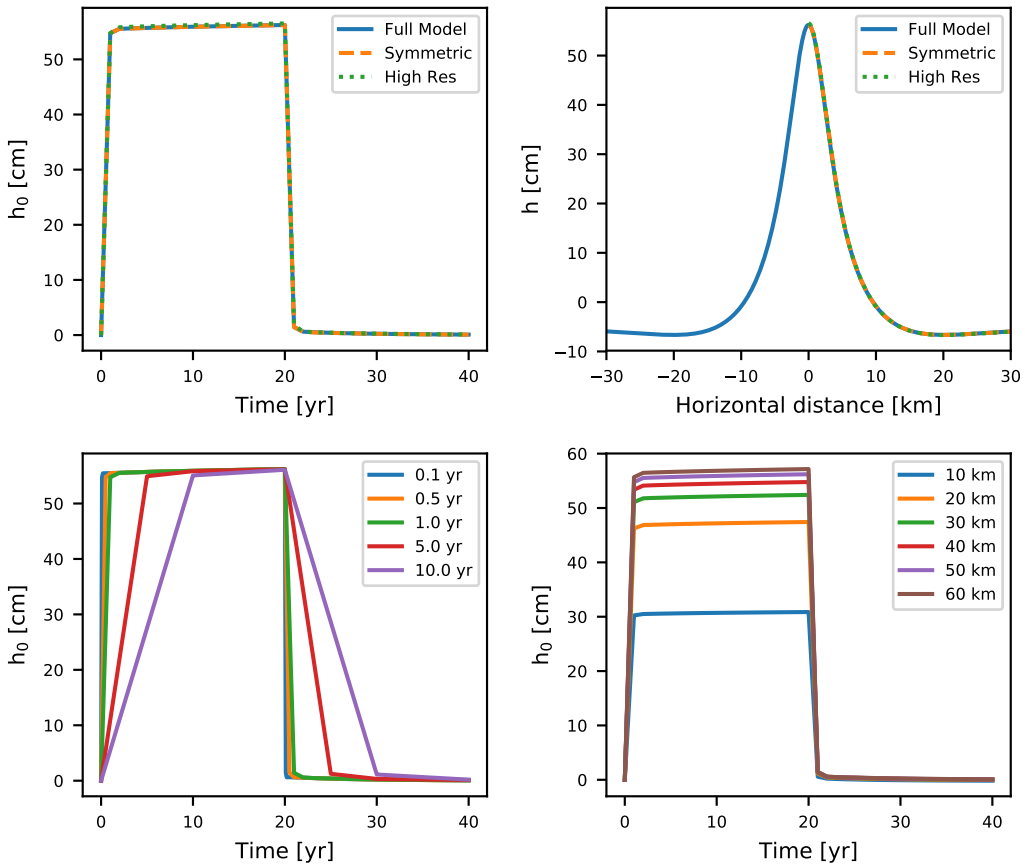

FIGURE 4.F.2: Results of 2D models. (a) Comparison of the maximum surface uplift through time between the full size model, the symmetric version and the symmetric version at doubled resolution. (b) Comparison of a surface profile at 20 years between the full size model, the symmetric version and the symmetric version at doubled resolution. (c) Maximum surface uplift through time in the reference model using different time steps. (d) Maximum surface uplift through time in the reference model using different model widths.

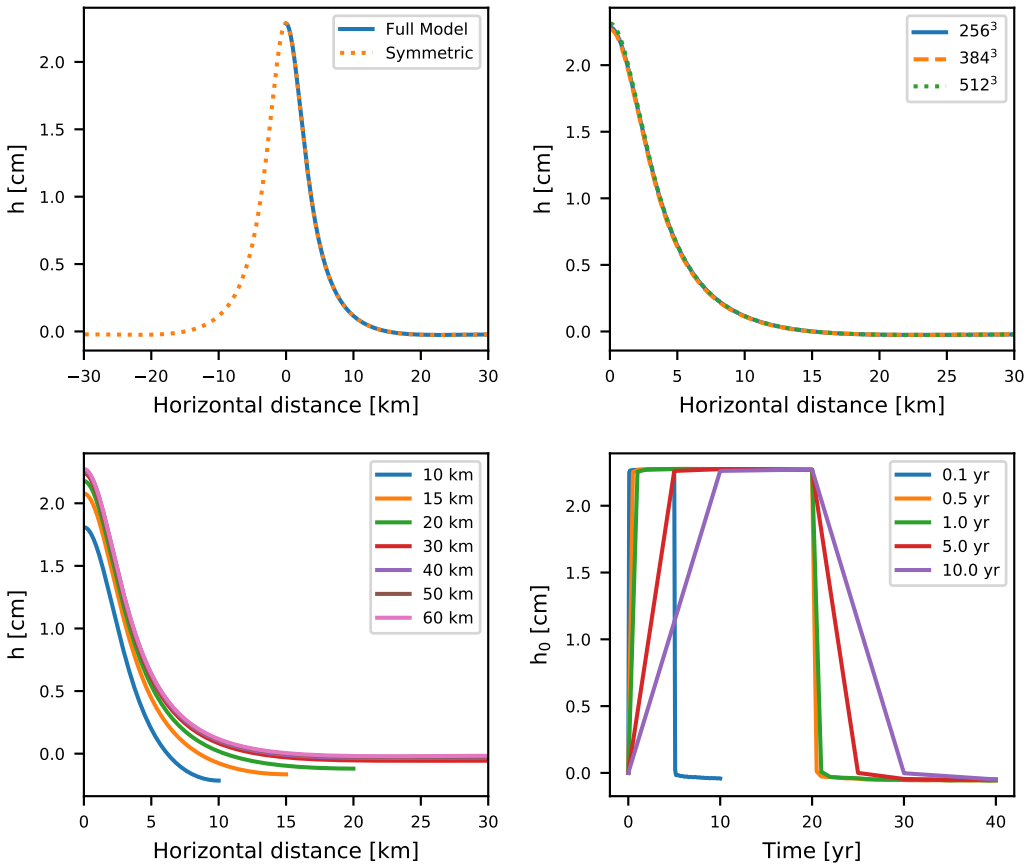

FIGURE 4.F.3: Results of 3D models. (a) Surface profile after 20 years (right before removal of the volatiles) for the full size model and the symmetric version (used in the study). (b) Surface profile after 20 years for different model resolutions. (c) Surface profile after 20 years for different model widths. (d) Maximum surface uplift through time in the reference model using different time steps.

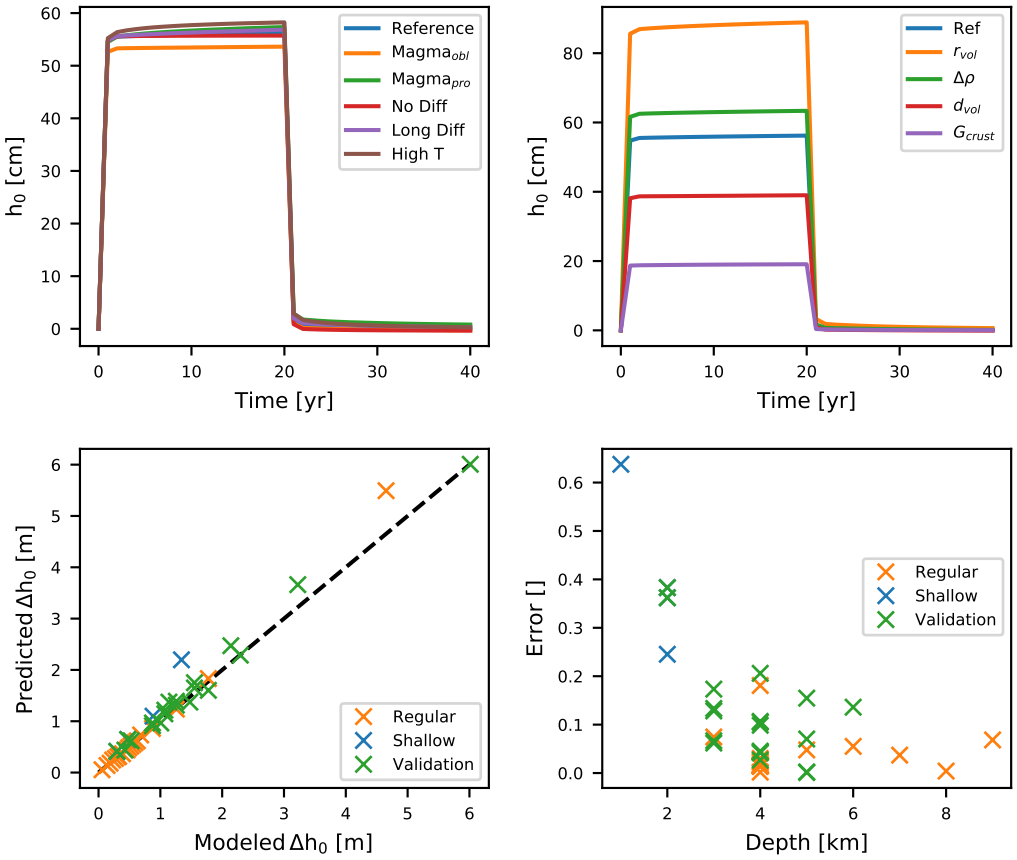

FIGURE 4.F.4: Results of 2D models. (a) Maximum surface uplift through time for different magma body shapes and temperature structures. All models show similar results. (b) Effect of perturbing one crucial material parameter compared to the reference model. (c) Comparison between modeled subsidence and subsidence predicted by equation 4.14. Black dashed line shows 1:1 correlation. Orange crosses show models that were used to derive equation 4.14, green crosses show models that were used to test it and blue crosses show models with a shallow (<= 2 km) volatile reservoir. (d) Error between the modeled subsidence and the predicted subsidence in dependence of reservoir depth. Error is only $> 20\%$ for the models with a shallow volatile reservoir.

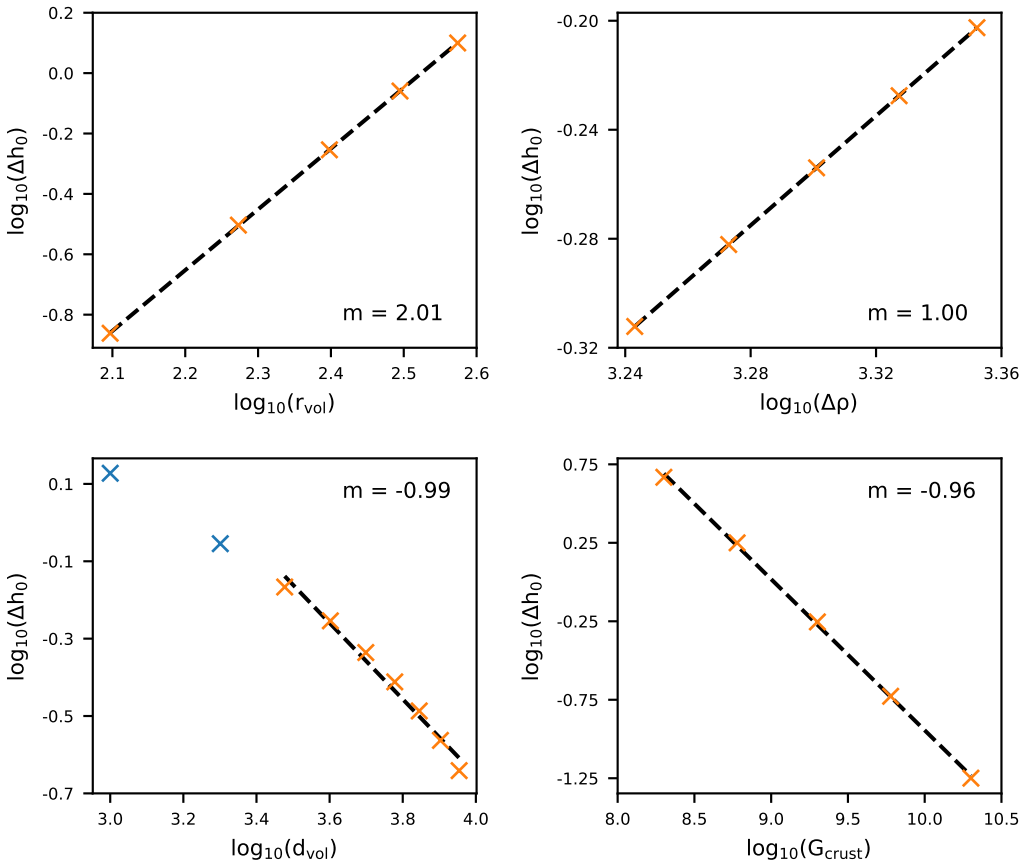

FIGURE 4.F.5: Results of scaling law analysis in 2D. Surface subsidence upon volatile removal (Δh_0) in dependence of the 4 material parameters, we found to be significant. m denotes the slope of the linear fits and equates to the exponent of the parameter in the scaling law (equation 4.14). Blue crosses in c denote two shallow models ($d <= 2\,km$) that were excluded to allow a linear fit.

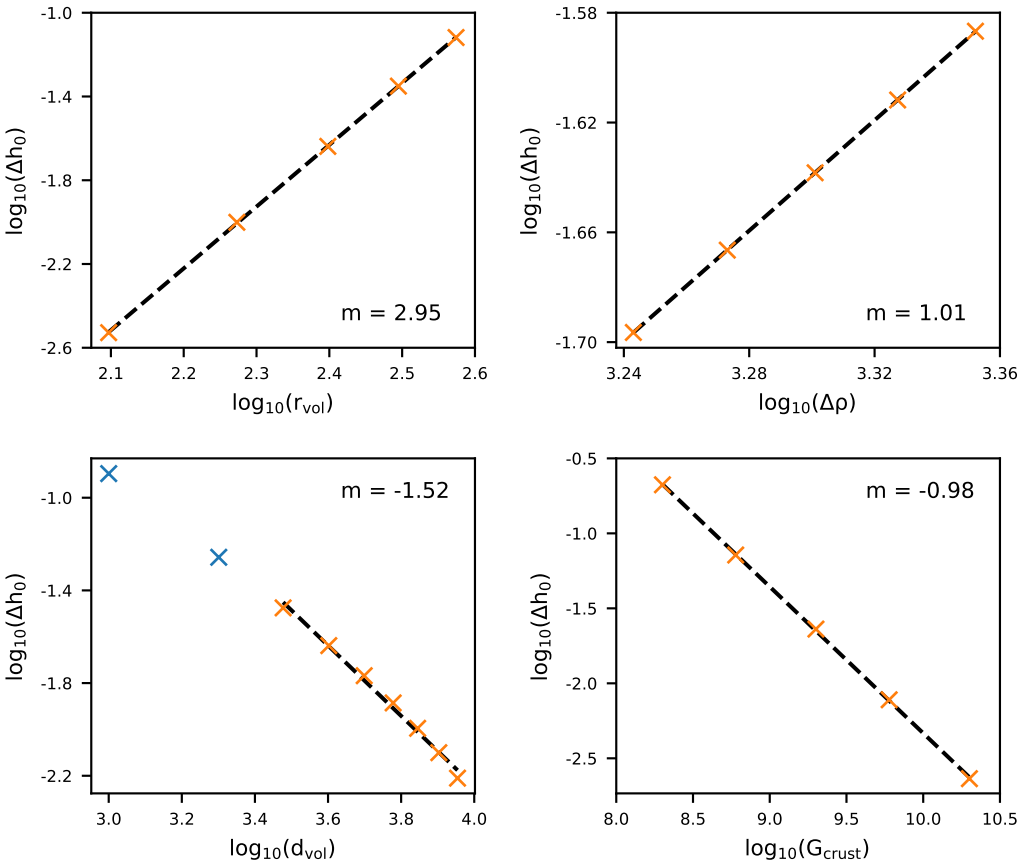

FIGURE 4.F.6: Results of scaling law analysis in 3D. Surface subsidence upon volatile removal (Δh_0) in dependence of the 4 material parameters, we found to be significant. m denotes the slope of the linear fits and equates to the exponent of the parameter in the scaling law (equation 4.8). Blue crosses in c denote two shallow models ($d <= 2\,km$) that were excluded to allow a linear fit.

Chapter 5

Summary & Conclusion

5.1 Geodynamic modeling with uncertain initial geometries

Chapter 2 presents a new and flexible parameterization for complex 3D shapes. The method is based on defining a reference geometry which may be any 3D volume and representing it as a collection of parallel 2D polygons. A subset of these polygons can then be chosen to be control polygons and for each, a pair of scaling parameters is defined which are used to alter the control polygon in its 2D plane. Scaling parameters for the other polygons are interpolated from the surrounding control polygons so that the entire body can be transformed with only a few parameters. One additional parameter can be used to change the spacing between the polygons so that the body can also be transformed in the third dimension. To make the methodology available to the community, we implemented it into the open-source software geomIO (https://bitbucket.org/geomio/geomio).

We apply this methodology to two different synthetic geological settings. A salt diapir in an extending regime and the density driven subduction of oceanic lithosphere underneath a continent. The shape and height of the salt diapir is parameterized by 5 scaling parameters and the subduction setup is parameterized by two parameters, the initial dip angle of the subducting slab and the width of the weak channel between the plates. In both cases, the model results change depending on the geometric parameters.

In the case of the salt, the different initial setups result in the development of distinctly different fault zones. Location, inclination and length of the faults change as a function of the diapir's height, head and neck width. For some geometries, the deformation is shared between two faults or systems of many smaller faults. With the help of the parameterization, it is possible to create links between geometric properties of the salt diapir and geometric properties of the faults. This means that, given faults can be identified by seismic imaging or other means, it is possible to constrain the geometry of the salt diapir and reduce the ambiguity of imaging studies by geodynamic modeling.

In the case of the subduction zone, the velocity of both plates change with changing initial dip angle. More importantly, for initial dip angles $> 65°$, the subducting plate undergoes a phase of strongly elevated velocities which lasts for a few Myr. Models with a lower initial dip angle never enter this regime. A wider weak channel generally results in higher plate velocities and a larger range of models enter the regime of strongly elevated velocities. Analogously to the salt diapir, a reconstructed velocity profile can be used to infer an initial subduction angle.

The flexible parameterization developed in this study provides the opportunity to conveniently test different initial model geometries. Both applications demonstrate that small variations in the initial geometry can lead to significant changes in the

model results and suggest to treat geometry as a flexible input parameter. The possibility to invert for an uncertain geometry changes the relationship between imaging studies and models. Whereas imaging studies used to always serve as constraints for model input, models can now be used to reduce uncertainty of imaging studies.

5.2 A multiphysics approach to constrain the dynamics of the Altiplano-Puna magmatic system

Chapter 3 focuses on the large scale geodynamics of the Altiplano-Puna magma body (APMB) in the central Andes. The APMB is a partially molten region of the Andean crust imaged by several studies and measures about 200 km in diameter and about 15 km in thickness. At the surface above it, InSAR satellites have observed a $\sim$ 150 km wide concentric surface deformation pattern consisting of a $\sim$ 70 km wide uplifting area (up to 1.2 $\mathrm{cm\,yr^{-1}}$) surrounded by a ring of subsidence (up to 0.3 $\mathrm{cm\,yr^{-1}}$) for more than 25 years. Gravity measurements reveal a Bouguer anomaly of about 100 mGal which coincides with the lateral extent of the APMB.

As no imaging study can resolve individual patches of higher or lower melt content within the APMB, we approximate the body as a homogeneous material with uniform melt content, density and mechanical properties. We use the parameterization of chapter 2 to generate an ensemble of magma bodies, forward model the Bouguer anomaly and compare it to the observations. This helps constrain the shape and extent of the lower half of the APMB while the gravity anomalies show little sensitivity to its upper part. Including a variable density contrast between APMB and crust in the inversion process allows us to constrain it to the range of 90–130 $\mathrm{kg\,m^{-3}}$ (2σ). With the help of sampled eruption products, crustal density estimates, mass balance and a petrological model for melt densities, we can use this information to infer the average melt content in the APMB to be 15–22 %.

Utilizing a 3D thermomechanical finite differences code, we model the dynamics of the magma body within the Andean lithosphere and compare the resulting surface deformation to the InSAR observations. In the model, the surface velocities are coupled to material transport from the edges of the APMB towards a central rise at its top. The crust above the central rise is pushed upwards while the drainage at the edges of the APMB leads to subsidence of the surrounding crust which results in the concentric surface deformation pattern.

Any parameter that influences the magnitude of the flow inside the magma body also controls the magnitude of the surface velocities. This includes the rheology of the upper crust and the magma body, the density difference between them and the geometry of the central rise. In fact, without the central rise the observed deformation pattern cannot be reproduced. So we can use use the surface velocities to constrain the geometry of the upper part of the APMB.

The joint interpretation of surface deformation and gravity anomalies in combination with the parameterization of chapter 2 allows us to invert for the location, geometry and density of the APMB. This demonstrates how different data sets are sensitive to different components of the model. We are also able to detect a coupling between the surface deformation and material transport within the crustal magma body. With the help of automated scaling law analysis, we identify the crucial material parameters which control the magnitude of the sub-surface flow and thereby the surface deformation.

The origin of the central rise of the APMB remains an open question as the model shows its necessity but cannot develop it self consistently from a flat topped APMB.

Reasonable explanations are that the central rise represents pathways of previous eruptions or the area where new batches of magma are emplaced from below.

5.3 Quantification of volcano deformation caused by volatile accumulation and release

Chapter 4 focuses on a specific component of magmatic systems. The buoyancy of reservoirs of exsolved volatile components such as CO_2, H_2O and SO_2 at the top of magma bodies. The existence of these reservoirs is inferred from the "excess gas" phenomenon where volcanoes emit much more SO_2 than could have been dissolved in the erupted magma. A reservoir containing exsolved volatiles from the entire magma body and not just the erupting part can provide an explanation for "excess gas" and is expected to exert a buoyancy force on the overlying crust because of its low density. In case of an eruption, this buoyancy force is removed instantly which results in syn-eruptive subsidence of the volcanic edifice.

We use the same thermomechanical code as in chapters 2 and 3 to model this process. Our model consists of a homogeneous crust, a spherical non-buoyant magma body and, on top of it, a small spherical body of low density, viscosity and rigidity to represent the volatile reservoir. To approximate an eruption, we instantly replace the low density reservoir with non-buoyant magma after 20 years which results in immediate subsidence at the surface.

The magnitude of subsidence is independent of the temperature structure, and therefore viscosity, of the crust as well as the shapes of magma and volatile reservoir. Instead, it depends on the volume and depth of the volatile reservoir, the density difference between volatiles and crust as well as the shear modulus of the crust. As the dependence on these parameters is stable over a range of reasonable values, we derive a scaling law that predicts the surface subsidence as function of them. It is able to predict the model results within 10% if the depth of the volatile reservoir is larger than 2 km.

The April 2015 eruption of the Chilean stratovolcano Calbuco emitted "excess gas" and InSAR observation identified syn-eruptive subsidence of up to 12 cm. We use our derived scaling law and, depending on the reservoir depth and the amount of CO_2, estimate between 1 and 4 cm of this subsidence to be caused by the release of a buoyant reservoir of pre-exsolved volatiles. This is a significant contribution and because of the simplicity of the scaling law, it could routinely be added to existing models for volcano deformation. The majority of the subsidence is most likely caused by the loss of volume in the magma body.

Another implication of our study is that uplift of few centimeters over time does not necessarily imply intrusion of magma in the crust but could also be the result of the growth of a reservoir of exsolved volatiles. Furthermore, our study suggests that magma that intrudes at levels where it is still buoyant, does not just contribute to surface deformation through displacement of country rock but also through buoyancy.

5.4 General implications for modeling

The studies presented in this thesis address a number of issues that are critical to not only magmatic systems but geodynamic modeling in general. The role of the initial model geometry, the non-uniqueness of the model solution and parameter sensitivity.

5.4.1 The role of initial geometry

Chapters 2 and 3 both demonstrate how significant the initial geometry of the model is. While this finding is not necessarily new, the issue often remains unaddressed because of a lack of appropriate parameterizations. Chapter 2 describes a parameterization for geometry which is applicable to many geological settings, providing a tool for future studies to include initial geometry as a flexible input parameter. In case an imaging study provides their results in the form of uncertainties, they can be directly used by creating an ensemble of initial geometries using random numbers whose distributions represent the uncertainties.

The surface subsidence in chapter 4 is independent of the shape of the volatile reservoir which seems counter-intuitive given the findings of chapters 2 and 3. The most likely explanation for this is the fact that in the small and compact volatile reservoir, the buoyancy forces are oriented strictly upwards whereas in the complex shaped 200 km wide APMB there is lot of lateral transport towards the central rise. It is possible that the geometry of the volatile reservoir starts to play a role for more complex shapes than the simple oblates and prolates that we investigated but for such a small object, model resolution quickly becomes a limiting factor.

Another difference are the dominant deformation mechanisms. Chapter 4 is characterized by immediate elastic effects whereas the study of chapter 3 deals with larger timescales where viscous deformation plays an important role. Both studies in chapter 2 are dominated by plastic deformation which is very sensitive to geometric features that help localize stresses.

5.4.2 Dealing with non-unique solutions

In any system that has more parameters than observables there is no unique solution. A simple example is the interpretation of gravity anomalies, where there is a trade-off between the density contrast of a body and its volume. In mechanical models, this interplay can be much more complex as parameters can be co-dependent (e.g. temperature and density) or there are run-away feedback loops like shear thinning rheologies. In practice, this means that no collection of surface observables will allow for a unique inversion result. Instead, there is always an infinite number of parameter combinations that can explain the observations.

This issue can, however, be mitigated by systematically varying parameters and analyzing their influence on the observables as demonstrated in sections 2.4.1.1 and 3.3.2. Such analyses can identify which parameters are crucial and which parameters have little influence and can be kept constant for further investigations. To get an even better understanding of the key parameters, resampling techniques as shown in chapter 3 can provide probability density functions for single parameters or parameter combinations.

So instead of producing only a single model that can reproduce observations, inversions can provide uncertainty ranges and facilitate an understanding of the interplay between parameters. If new studies or observations then add new constraints on one parameter, the uncertainty on all other parameters will also be reduced as a result.

5.4.3 Joint interpretation of observations

In chapter 3 we use gravity anomalies and surface deformation to constrain the geometry of the APMB. This was crucial as the gravity anomalies proved to not be sensitive to the upper part of the magma body while the surface deformation showed little dependence on the lower half of the magma body (see section 3.4.3.1). Only

by combining both datasets, the geometry of the entire body can be constrained. Even if an additional data set can only help constrain a single parameter, this can indirectly help constrain other parameters as explained in the previous section. Being aware of the different sensitivities of an observation to different parameters and adding observations if necessary can greatly improve the findings of modeling studies.

5.5 Implications for magmatic system modeling

This thesis outlines how a thermomechanical code can be utilized to investigate both the large scale geodynamics (chapter 3) and individual processes (chapter 4) of magmatic systems. In comparison to the majority of existing studies, the driving force for surface deformation is not displacement of host rock by an expanding cavity, but the buoyancy of partial melts (chapter 3) or volatile-rich foams (chapter 4). Buoyancy induced transport or forces can reproduce surface deformation that has traditionally been interpreted to be solely caused by intrusion or eruption of crustal-stored magma.

The continuum modeling approach which includes partial melt or magma as part of the model and not just as an internal boundary condition also allows for much greater insight into the properties and dynamics of the magma. Whereas the established "Mogi-model" and related models (section 1.3.1) can only make estimates of intrusion, location and volume change, the approach presented here includes the full size, location and geometry of the magma body as well as its rheology and density. Constraining these properties will facilitate a much more complete understanding of magmatic systems and is the first step towards models that have predictive power when it comes to onset, duration and magnitude of volcanic eruptions.

To conduct more studies like the one presented in chapter 3, extensive monitoring of the magmatic system and its setting is indispensable. This includes gravity anomalies, seismic imaging and surface deformation as a minimum requirement. Analysis of eruption products and gas emissions, magnetotelluric surveys and studies of the lithospheric setting and temperature structure provide useful additional constraints.

5.6 Outlook

While the studies presented in this thesis introduced numerous new components and approaches to modeling magmatic systems, there are still many aspects that remained unaddressed. Some of them are discussed in the following.

5.6.1 Intrusion and volume change

Chapters 3 and 4 have investigated the contribution of buoyancy to surface deformation. To do that, the effect of host rock displacement by intrusion was neglected. So a logical next step is the combination of both effects in one model. One possible way to achieve that is to add an internal pressure boundary condition inside of a visco-elasto-plastic, buoyant magma body. A different method is adding a feeding system to the magma body and prescribing an inflow of material from below. This section presents a first attempt at the latter approach in LaMEM (see section 1.6 for details on the code).

5.6.1.1 Setup

The 3D model consists of a homogeneous block of crust with 40 km diameter and 14 km depth which hosts an ellipsoidal magma body with horizontal semi-axes of 2.5

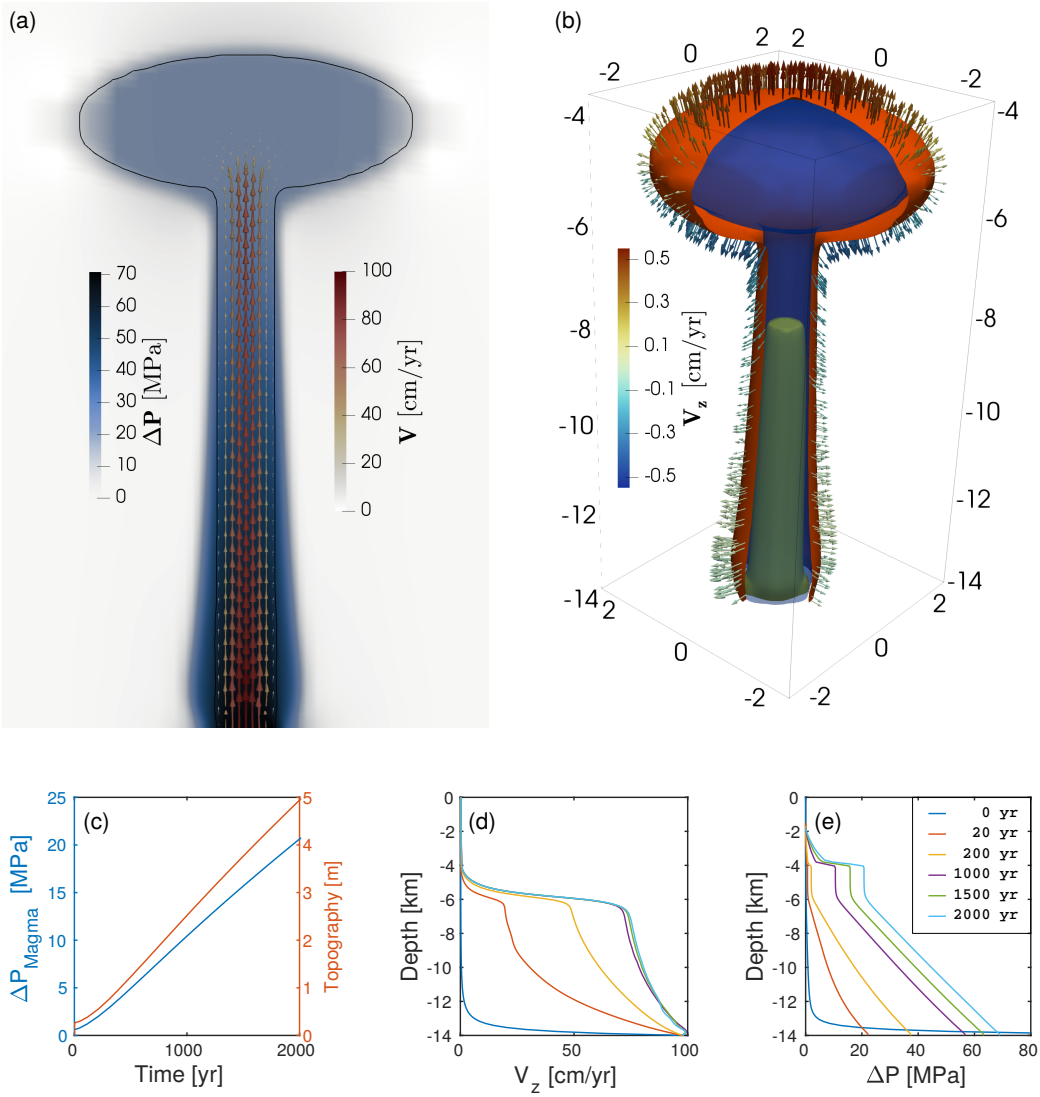

FIGURE 5.1: Results of magma intrusion from the model bottom. (a) 2D slice through the model after 2000 years. Magma body and feeder zone are outlined in black, arrows indicate established flow field with a parabolic velocity distribution. Background shows overpressure which decays along the feeding system and is homogeneous within the magma body. (b) 10 MPa overpressure contours after 200 years (yellow), 1000 years (blue) and 2000 years (orange). Arrows along the orange contour show velocities that are induced in the crust by the influx of magma. Arrow length shows velocity magnitude and colors indicate vertical component. Axes are in km. (c) Overpressure in the center of the magma body (blue) and surface topography (orange) at the surface above the system as a function of time. (d, e) Vertical profiles through the center of the model show the evolution of vertical velocity and overpressure in the magmatic system. Different colors represent different snapshots, see (e) for legend.

km and a vertical semi-axis of 1 km, centered at 5 km depth. A vertical channel of 450 m radius connects the magma body to the bottom of the model. 1 km of sticky air is placed above the internal free surface and free slip conditions are set along all domain boundaries. Where the vertical channel intersects the bottom of the model, a parabolic velocity profile with a maximum of 1 $\mathrm{m\,yr^{-1}}$ is prescribed (Figure 5.1a). The influx of magma is compensated by slow outflow of crustal material across the rest of the model bottom. To minimize buoyancy effects and focus on the effects of pressure change, crust and magma have the same reference density and no thermal expansion. The rheology is visco-elastic and table 5.1 summarizes all material parameters. The grid is refined in the center of the model to maximize the resolution of the vertical channel.

TABLE 5.1: Material parameters for intrusion example

Parameter		Crust	Magma	Air
G	[Pa]	2e9	1e8	1e8
ν		0.25	0.499	0.25
η_{lin}	[Pa s]	-	1e16	1e16
B_{dis}	$[\mathrm{Pa^{-n}\,s^{-1}}]$	1.55e-17	-	-
n		2.3	-	-
E_{dis}	$[\mathrm{J\,mol^{-1}}]$	154e3	-	-
T	[K]	273-573	1273	273
ρ	$[\mathrm{kg\,m^{-3}}]$	2500	2500	100

5.6.1.2 Results

The magma flux prescribed at the bottom leads to the development of velocity gradient along the vertical channel. The system approaches a steady state after about 1000 years (Figure 5.1d) with 1 $\mathrm{m\,yr^{-1}}$ at the bottom and 0.75 $\mathrm{m\,yr^{-1}}$ at the top of the channel. Within the magma body, the velocities quickly decay as the material spreads out. The influx of material leads to a pressurization of the feeder channel and the magma body. We define overpressure ΔP as follows:

$$\Delta P = P - P_{\mathrm{lith}}, \tag{5.1}$$

where P is full pressure and P_{lith} is lithostatic pressure. Figure 5.1e shows that a ΔP-profile develops alongside the velocity profile with a linear decay along the channel and homogeneous ΔP within the magma body. Once the velocity profile reaches a steady state, the overpressure in the system continues to grow linearly. The increase in pressure is accompanied by a constant surface uplift of 0.23 $\mathrm{cm\,yr^{-1}}$ (Figure 5.1c). Figure 5.1b illustrates the development of overpressure in the system by showing the $\Delta P = 10\,\mathrm{MPa}$ isocontour after 200, 1000 and 2000 years. It grows along the channel (yellow in Figure 5.1b) before it fills the entire magma body (blue) and then slowly advances into the surrounding crust (orange). The pressurized magma body causes radial displacement in the surrounding crust and so does the vertical channel (Figure 5.1b).

5.6.1.3 Implications

The model presented in this section shows a linear relationship between overpressure and surface displacement (Figure 5.1c) which is in agreement with the analytical solutions for expanding cavities (see section 1.3.1). This suggests that connecting a

magma body to an inflow boundary condition with a vertical channel is a good approximation of magma intrusion. With this approach, the surface response to both intrusion and buoyancy could be investigated, possibly facilitating a distinction between surface deformation caused by buoyancy and caused by a new pulse of magma. The compressibility of magma, especially in the presence of volatiles is likely going to be a critical parameter in such a study. A similar study to the presented model was performed by Alshembari et al. (2022), using an elastic crust and incompressible magma. It produces a similar dependence between magma flux and surface deformation.

5.6.2 Thermodynamics

In this thesis, magma or magmatic mush was approximated as a material of low, constant viscosity that was independent of temperature. However, in reality magma rheology is strongly dependent on pressure and temperature conditions as well as volatile content. Therefore, coupling magma properties to the conditions with the help of thermodynamic equilibrium models would be another step towards more realistic models. Ideally, the thermodynamic computations would be performed for every particle or node in the model at every time step which is unfeasible with established tools. One way around this issue is pre-computing many configurations and then using look-up tables during the thermomechanical modeling (Rummel et al., 2020). Recent advances (Riel et al., in press) might provide the stability and computational efficiency necessary to make full coupling possible in the future. This is also relevant for the host rock that is heated by intruding magma.

5.6.3 Tensile failure

One advantage of using LaMEM is the ability to include the mechanism of plastic failure in the models. This is, however, limited to shear failure or mode II and III fractures (Irwin, 1957) where units slide along a plane (i.e. normal, thrust and strike-slip faults). For models to develop magmatic dikes self consistently, it is necessary to develop a code that allows for tensile or Mode I failure where a unit splits along a plane to open up a fracture. This occurs under low compressive stress, extension and/or high pore fluid pressure.

5.6.4 Multi-phase models

Magmatic systems consist of host rock (solid), melt (liquid), crystals (solid) and exsolved volatiles (hypercritical fluid or gas). As most continuum models are single-phase, host rock and partially molten rock/magma have to be treated similarly. This is usually achieved by assigning a low viscosity and shear modulus to the partially molten rock or implementing a parameterization that lowers viscosity and rigidity as a function of melt content. In both cases, volatiles are neglected entirely. In more advanced two-phase models, the melt can be treated separately from the host rock and effects of volatiles and crystals on liquid viscosity could be included through parameterizations. Moving from single-phase models with parameterizations for melt to 2-phase models with parameterizations for volatiles and crystals.

Eidesstattliche Erklärung

Ich versichere hiermit gemäß §10 Abs. 3d der Promotionsordnung des Fachbereichs 09 (Chemie, Pharmazie und Geowissenschaften) der Johannes Gutenberg-Universität Mainz vom 24.07.2007, die als Dissertation vorgelegte Arbeit selbständig und nur unter Verwendung der in der Arbeit angegebenen Hilfsmittel verfasst zu haben. Ich habe oder hatte die hier als Dissertation vorgelegte Arbeit nicht als Prüfungsarbeit für eine staatliche oder andere wissenschaftliche Prüfung eingereicht. Ich hatte weder die jetzt als Dissertation vorgelegte Arbeit noch Teile davon bei einer anderen Fakultät bzw. einem anderen Fachbereich als Dissertation eingereicht.

Arne Spang
Mainz, 2022

Bibliography

Ajtai, Nicolae, Horaţiu I Ştefănie, Laurenţiu C Stoian, and Marius G Oprea (2010). "The volcanic ash and its impact on European air transport industry. A case study on the detection and impact of the the Eyjafjallajökull volcanic ash plume over North-Western Europe between 14th and 21st April 2010". In: *Advances in Environmental Sciences* 2.1, pp. 57–68.

Alisic, Laura, Michael Gurnis, Georg Stadler, Carsten Burstedde, Lucas C Wilcox, and Omar Ghattas (2010). "Slab stress and strain rate as constraints on global mantle flow". In: *Geophysical Research Letters* 37.22.

Alshembari, Rami, James Hickey, Ben J Williamson, and Katharine Cashman (2022). "Exploring the role of fluid-solid interactions for modelling volcano deformation". In: *Journal of Volcanology and Geothermal Research* 426, p. 107535.

Anderson, Ernest Masson (1937). "IX.—the dynamics of the formation of cone-sheets, ring-dykes, and caldron-subsidences". In: *Proceedings of the Royal Society of Edinburgh* 56, pp. 128–157.

Anderson, Kyle and Paul Segall (2011). "Physics-based models of ground deformation and extrusion rate at effusively erupting volcanoes". In: *Journal of Geophysical Research: Solid Earth* 116.B7.

Annen, Catherine, Michel Pichavant, Olivier Bachmann, and Alain Burgisser (2008). "Conditions for the growth of a long-lived shallow crustal magma chamber below Mount Pelee volcano (Martinique, Lesser Antilles Arc)". In: *Journal of Geophysical Research: Solid Earth* 113.B7.

Arzilli, Fabio et al. (2019). "The unexpected explosive sub-Plinian eruption of Calbuco volcano (22–23 April 2015; Southern Chile): triggering mechanism implications". In: *Journal of Volcanology and Geothermal Research* 378, pp. 35–50.

Bachmann, Olivier and George W Bergantz (2004). "On the origin of crystal-poor rhyolites: extracted from batholithic crystal mushes". In: *Journal of Petrology* 45.8, pp. 1565–1582.

Barthelmes, F. and W. Köhler (2016). "International Centre for Global Earth Models (ICGEM), in: The Geodesists Handbook 2016". In: *Journal of Geodesy (2016)* 90.10, pp. 907–1205.

Baumann, Tobias S and Boris J P Kaus (2015). "Geodynamic inversion to constrain the non-linear rheology of the lithosphere". In: *Geophysical Journal International* 202.2, pp. 1289–1316.

Baumann, Tobias S, Boris J P Kaus, and Anton A Popov (2014). "Constraining effective rheology through parallel joint geodynamic inversion". In: *Tectonophysics* 631, pp. 197–211. DOI: https://doi.org/10.1016/j.tecto.2014.04.037.

Baumann, Tobias S, Boris J P Kaus, and Anton A Popov (2018). "Deformation and stresses related to the gorleben salt structure: insights from 3d numerical models". In: *Mechanical Behavior of Salt, Saltmech IX*, pp. 15–27.

Bauville, Arthur and Tobias S Baumann (2019). "geomIO: an open-source MATLAB toolbox to create the initial configuration of 2-D/3-D thermo-mechanical simulations from 2-D vector drawings". In: *Geochemistry, Geophysics, Geosystems* 20.3, pp. 1665–1675. DOI: https://doi.org/10.1029/2018GC008057.

Beucher, Romain, Louis Moresi, Julian Giordani, John Mansour, Dan Sandiford, Rebecca Farrington, Luke Mondy, Claire Mallard, Patrice Rey, Guillaume Duclaux, et al. (2019). "UWGeodynamics: A teaching and research tool for numerical geodynamic modelling". In: *Journal of Open Source Software* 4.36, p. 1136.

Billen, Magali I and Greg Hirth (2007). "Rheologic controls on slab dynamics". In: *Geochemistry, Geophysics, Geosystems* 8.8.

Blundy, Jonathan, Katharine V Cashman, Alison Rust, and Fred Witham (2010). "A case for CO2-rich arc magmas". In: *Earth and Planetary Science Letters* 290.3-4, pp. 289–301.

Bosch, Miguel, Tapan Mukerji, and Ezequiel F Gonzalez (2010). "Seismic inversion for reservoir properties combining statistical rock physics and geostatistics: A review". In: *Geophysics* 75.5, 75A165–75A176.

Boschetti, Fabio, Chris Wijns, and Louis Moresi (2003). "Effective exploration and visualization of geological parameter space". In: *Geochemistry, Geophysics, Geosystems* 4.10.

Brasse, Heinrich, Pamela Lezaeta, Volker Rath, Katrin Schwalenberg, Wolfgang Soyer, and Volker Haak (2002). "The Bolivian altiplano conductivity anomaly". In: *Journal of Geophysical Research: Solid Earth* 107.B5. DOI: 10.1029/2001JB000391.

Breitkreuz, C and W Zeil (1984). "Geodynamic and magmatic stages on a traverse through the Andes between 20 and 24 S (N Chile, S Bolivia, NW Argentina)". In: *Journal of the Geological Society* 141.5, pp. 861–868.

Byerlee, James (1978). "Friction of rocks". In: *Rock friction and earthquake prediction*. Birkhäuser, Basel, pp. 615–626.

Canon-Tapia, Edgardo (2014). "Volcanic eruption triggers: A hierarchical classification". In: *Earth-Science Reviews* 129, pp. 100–119.

Castruccio, Angelo, Jorge Clavero, Andrea Segura, Pablo Samaniego, Olivier Roche, Jean-Luc Le Pennec, and Bárbara Droguett (2016). "Eruptive parameters and dynamics of the April 2015 sub-Plinian eruptions of Calbuco volcano (southern Chile)". In: *Bulletin of Volcanology* 78.9, pp. 1–19.

Caumon, Guillaume, PLCD Collon-Drouaillet, C Le Carlier de Veslud, Sophie Viseur, and J Sausse (2009). "Surface-based 3D modeling of geological structures". In: *Mathematical Geosciences* 41.8, pp. 927–945.

Charco, María and Pedro Galán del Sastre (2014). "Efficient inversion of three-dimensional finite element models of volcano deformation". In: *Geophysical Journal International* 196.3, pp. 1441–1454.

Chmielowski, Josef, George Zandt, and Christian Haberland (1999). "The central Andean Altiplano-Puna magma body". In: *Geophysical Research Letters* 26.6, pp. 783–786.

Čížková, Hana and Craig R Bina (2015). "Geodynamics of trench advance: Insights from a Philippine-Sea-style geometry". In: *Earth and Planetary Science Letters* 430, pp. 408–415.

Comeau, Matthew J, Martyn J Unsworth, Faustino Ticona, and Mayel Sunagua (2015). "Magnetotelluric images of magma distribution beneath Volcán Uturuncu, Bolivia: Implications for magma dynamics". In: *Geology* 43.3, pp. 243–246. DOI: 10.1130/G36258.1.

Comeau, Matthew J, Martyn J Unsworth, and Darcy Cordell (2016). "New constraints on the magma distribution and composition beneath Volcán Uturuncu and the southern Bolivian Altiplano from magnetotelluric data". In: *Geosphere* 12.5, pp. 1391–1421. DOI: 10.1130/GES01277.1.

Crameri, F, H Schmeling, G J Golabek, T Duretz, R Orendt, SJH Buiter, DA May, BJP Kaus, TV Gerya, and PJ Tackley (2012). "A comparison of numerical surface

topography calculations in geodynamic modelling: an evaluation of the 'sticky air'method". In: *Geophysical Journal International* 189.1, pp. 38–54.

Crameri, Fabio (2018). "Scientific colour-maps". In: *Zenodo* 10. DOI: 10.5281/zenodo.1243862.

De Silva, SL (1989). "Altiplano-Puna volcanic complex of the central Andes". In: *Geology* 17.12, pp. 1102–1106.

Del Negro, Ciro, Gilda Currenti, and Danila Scandura (2009). "Temperature-dependent viscoelastic modeling of ground deformation: Application to Etna volcano during the 1993–1997 inflation period". In: *Physics of the Earth and Planetary Interiors* 172.3-4, pp. 299–309.

Delgado, Francisco, Matthew E Pritchard, Susanna Ebmeier, Pablo González, and Luis Lara (2017). "Recent unrest (2002–2015) imaged by space geodesy at the highest risk Chilean volcanoes: Villarrica, Llaima, and Calbuco (Southern Andes)". In: *Journal of Volcanology and Geothermal Research* 344, pp. 270–288.

DeNosaquo, Katrina R, Robert B Smith, and Anthony R Lowry (2009). "Density and lithospheric strength models of the Yellowstone–Snake River Plain volcanic system from gravity and heat flow data". In: *Journal of Volcanology and Geothermal Research* 188.1-3, pp. 108–127.

Dieterich, James H and Robert W Decker (1975). "Finite element modeling of surface deformation associated with volcanism". In: *Journal of Geophysical Research* 80.29, pp. 4094–4102.

Drucker, Daniel Charles and William Prager (1952). "Soil mechanics and plastic analysis or limit design". In: *Quarterly of applied mathematics* 10.2, pp. 157–165.

Duretz, Thibault, David Alexander May, TV Gerya, and PJ Tackley (2011). "Discretization errors and free surface stabilization in the finite difference and marker-in-cell method for applied geodynamics: A numerical study". In: *Geochemistry, Geophysics, Geosystems* 12.7. DOI: 10.1029/2011GC003567.

Duretz, Thibault, Riccardo Asti, Yves Lagabrielle, Jean-Pierre Brun, Anthony Jourdon, Camille Clerc, and Benjamin Corre (2020). "Numerical modelling of Cretaceous Pyrenean Rifting: The interaction between mantle exhumation and syn-rift salt tectonics". In: *Basin Research* 32.4, pp. 652–667.

Fialko, Yuri and Jill Pearse (2012). "Sombrero uplift above the Altiplano-Puna magma body: Evidence of a ballooning mid-crustal diapir". In: *Science* 338.6104, pp. 250–252. DOI: 10.1126/science.1226358.

Fialko, Yuri, Mark Simons, and Duncan Agnew (2001). "The complete (3-D) surface displacement field in the epicentral area of the 1999 Mw7.1 Hector Mine earthquake, California, from space geodetic observations". In: *Geophysical research letters* 28.16, pp. 3063–3066.

Fialko, Yuri, Yakov Khazan, and Mark Simons (2001a). "Deformation due to a pressurized horizontal circular crack in an elastic half-space, with applications to volcano geodesy". In: *Geophysical Journal International* 146.1, pp. 181–190.

Frank, Tobias, Anne-Laure Tertois, and Jean-Laurent Mallet (2007). "3D-reconstruction of complex geological interfaces from irregularly distributed and noisy point data". In: *Computers & Geosciences* 33.7, pp. 932–943.

Fraters, Menno, Cedric Thieulot, Arie Van Den Berg, and Wim Spakman (2019). "The Geodynamic World Builder: a solution for complex initial conditions in numerical modeling". In: *Solid Earth* 10.5, pp. 1785–1807.

Freire, Sergio, Aneta J Florczyk, Martino Pesaresi, and Richard Sliuzas (2019). "An improved global analysis of population distribution in proximity to active volcanoes, 1975–2015". In: *ISPRS international journal of geo-information* 8.8, p. 341. DOI: https://doi.org/10.3390/ijgi8080341.

Fullagar, Peter K, Neil A Hughes, and John Paine (2000). "Drilling-constrained 3D gravity interpretation". In: *Exploration Geophysics* 31.2, pp. 17–23.

Galley, Christopher G, Peter G Lelièvre, and Colin G Farquharson (2020). "Geophysical inversion for 3D contact surface geometry". In: *Geophysics* 85.6, K27–K45.

Gercek, H (2007). "Poisson's ratio values for rocks". In: *International Journal of Rock Mechanics and Mining Sciences* 44.1, pp. 1–13. DOI: 10.1016/j.ijrmms.2006.04.011.

Gíslason, Sigurður R, Helgi A Alfredsson, Eydís S Eiríksdóttir, Tue Hassenkam, and Susan LS Stipp (2011). "Volcanic ash from the 2010 Eyjafjallajökull eruption". In: *Applied Geochemistry* 26, S188–S190.

Godoy, Benigno, Gerhard Wörner, Shoji Kojima, Felipe Aguilera, Klaus Simon, and Gerald Hartmann (2014). "Low-pressure evolution of arc magmas in thickened crust: The San Pedro–Linzor volcanic chain, Central Andes, northern Chile". In: *Journal of south american earth sciences* 52, pp. 24–42.

Godoy, Benigno, Gerhard Wörner, Petrus Le Roux, Shanaka de Silva, Miguel Ángel Parada, Shoji Kojima, Osvaldo González-Maurel, Diego Morata, Edmundo Polanco, and Paula Martínez (2017). "Sr-and Nd-isotope variations along the Pleistocene San Pedro–Linzor volcanic chain, N. Chile: Tracking the influence of the upper crustal Altiplano-Puna Magma Body". In: *Journal of Volcanology and Geothermal Research* 341, pp. 172–186. DOI: 10.1016/j.jvolgeores.2017.05.030.

Gottsmann, J, J Blundy, Scott T Henderson, Matthew E Pritchard, and RSJ Sparks (2017). "Thermomechanical modeling of the Altiplano-Puna deformation anomaly: Multiparameter insights into magma mush reorganization". In: *Geosphere* 13.4, pp. 1042–1065. DOI: 10.1130/GES01420.1.

Gottsmann, Joachim, Rodrigo del Potro, and Cyril Muller (2018). "50 years of steady ground deformation in the Altiplano-Puna region of southern Bolivia". In: *Geosphere* 14.1, pp. 65–73. DOI: 10.1130âĂŃ/GES01570.1.

Götze, H-J and S Krause (2002). "The Central Andean gravity high, a relic of an old subduction complex?" In: *Journal of South American Earth Sciences* 14.8, pp. 799–811.

Götze, Hans-Jürgen and Andreas Kirchner (1997). "Interpretation of gravity and geoid in the Central Andes between 20 and 29 S". In: *Journal of South American Earth Sciences* 10.2, pp. 179–188.

Gudmundsson, Magnús T, Thorvaldur Thordarson, Ármann Höskuldsson, Gudrún Larsen, Halldór Björnsson, Fred J Prata, Björn Oddsson, Eyjólfur Magnússon, Thórdís Högnadóttir, Guðrún Nína Petersen, et al. (2012). "Ash generation and distribution from the April-May 2010 eruption of Eyjafjallajökull, Iceland". In: *Scientific reports* 2.1, pp. 1–12.

Guillen, Antonio, Gabriel Courrioux, Ph Calcagno, Richard Lane, Terry Lees, and Philip McInerney (2004). "Constrained gravity 3D litho-inversion applied to Broken Hill". In: *ASEG Extended Abstracts* 2004.1, pp. 1–6.

Harlow, Francis H and J Eddie Welch (1965). "Numerical calculation of time-dependent viscous incompressible flow of fluid with free surface". In: *The physics of fluids* 8.12, pp. 2182–2189.

Heap, Michael J, Marlène Villeneuve, Fabien Albino, Jamie I Farquharson, Elodie Brothelande, Falk Amelung, Jean-Luc Got, and Patrick Baud (2020). "Towards more realistic values of elastic moduli for volcano modelling". In: *Journal of volcanology and geothermal research* 390, p. 106684.

Hedenquist, Jeffrey W and Jacob B Lowenstern (1994). "The role of magmas in the formation of hydrothermal ore deposits". In: *Nature* 370.6490, pp. 519–527.

Heit, Benjamin, I Koulakov, Günter Asch, Xiaohui Yuan, Rainer Kind, I Alcocer-Rodriguez, S Tawackoli, and H Wilke (2008). "More constraints to determine the seismic structure beneath the Central Andes at 21 S using teleseismic tomography analysis". In: *Journal of South American Earth Sciences* 25.1, pp. 22–36.

Henderson, Scott T and Matthew E Pritchard (2013). "Decadal volcanic deformation in the Central Andes Volcanic Zone revealed by InSAR time series". In: *Geochemistry, Geophysics, Geosystems* 14.5, pp. 1358–1374. DOI: 10.1002/ggge.20074.

Henderson, Scott T and Matthew E Pritchard (2017). "Time-dependent deformation of Uturuncu volcano, Bolivia, constrained by GPS and InSAR measurements and implications for source models". In: *Geosphere* 13.6, pp. 1834–1854. DOI: 10.1130/GES01203.1.

Hickey, James and Joachim Gottsmann (2014). "Benchmarking and developing numerical Finite Element models of volcanic deformation". In: *Journal of Volcanology and Geothermal Research* 280, pp. 126–130.

Hickey, James, Joachim Gottsmann, and Rodrigo del Potro (2013). "The large-scale surface uplift in the Altiplano-Puna region of Bolivia: A parametric study of source characteristics and crustal rheology using finite element analysis". In: *Geochemistry, Geophysics, Geosystems* 14.3, pp. 540–555.

Hickey, James, Joachim Gottsmann, Haruhisa Nakamichi, and Masato Iguchi (2016). "Thermomechanical controls on magma supply and volcanic deformation: application to Aira caldera, Japan". In: *Scientific reports* 6.1, pp. 1–10.

Hoek, Evert and Edwin T Brown (1997). "Practical estimates of rock mass strength". In: *International journal of rock mechanics and mining sciences* 34.8, pp. 1165–1186.

Ibarra, Federico, S Liu, Christian Meeßen, CB Prezzi, J Bott, M Scheck-Wenderoth, S Sobolev, and MR Strecker (2019). "3D data-derived lithospheric structure of the Central Andes and its implications for deformation: Insights from gravity and geodynamic modelling". In: *Tectonophysics* 766, pp. 453–468.

Ingraham, Mathew Duffy, Scott Thomas Broome, Stephen J Bauer, Perry Carl Barrow, and Gregory Mark Flint (2015). "Behavior of salt from the Bayou Choctaw salt dome". In: *49th US Rock Mechanics/Geomechanics Symposium*. OnePetro.

Irwin, George R (1957). "Analysis of stresses and strains near the end of a crack traversing a plate". In:

Jackson, Christopher A-L and Matthew M Lewis (2012). "Origin of an anhydrite sheath encircling a salt diapir and implications for the seismic imaging of steep-sided salt structures, Egersund Basin, Northern North Sea". In: *Journal of the Geological Society* 169.5, pp. 593–599. DOI: 10.1144/0016-76492011-126.

Jackson, MD, J Blundy, and RSJ Sparks (2018). "Chemical differentiation, cold storage and remobilization of magma in the Earth's crust". In: *Nature* 564.7736, pp. 405–409.

Jadamec, Margarete A, Magali I Billen, and Sarah M Roeske (2013). "Three-dimensional numerical models of flat slab subduction and the Denali fault driving deformation in south-central Alaska". In: *Earth and Planetary Science Letters* 376, pp. 29–42.

Jang, Hyun-Sic, Qing-Zhao Zhang, Seong-Seung Kang, and Bo-An Jang (2018). "Determination of the basic friction angle of rock surfaces by tilt tests". In: *Rock Mechanics and Rock Engineering* 51.4, pp. 989–1004.

Jay, Jennifer A, Matthew E Pritchard, Michael E West, Douglas Christensen, Matthew Haney, Estela Minaya, Mayel Sunagua, Stephen R McNutt, and Mario Zabala (2012). "Shallow seismicity, triggered seismicity, and ambient noise tomography at the long-dormant Uturuncu Volcano, Bolivia". In: *Bulletin of Volcanology* 74.4, pp. 817–837.

Jessell, Mark (2001). "Three-dimensional geological modelling of potential-field data". In: *Computers & Geosciences* 27.4, pp. 455–465.

Jones, Ian F and Ian Davison (2014). "Seismic imaging in and around salt bodies". In: *Interpretation* 2.4, SL1–SL20. DOI: 10.1190/INT-2014-0033.1.

Juhlin, Christopher, Mahdieh Dehghannejad, Björn Lund, Alireza Malehmir, and Gerhard Pratt (2010). "Reflection seismic imaging of the end-glacial Pärvie Fault system, northern Sweden". In: *Journal of Applied Geophysics* 70.4, pp. 307–316.

Kaus, Boris J P, Hans Mühlhaus, and Dave A May (2010). "A stabilization algorithm for geodynamic numerical simulations with a free surface". In: *Physics of the Earth and Planetary Interiors* 181.1-2, pp. 12–20.

Kaus, Boris J P, Anton A Popov, T Baumann, A Pusok, Arthur Bauville, Naiara Fernandez, and Marine Collignon (2016). "Forward and inverse modelling of lithospheric deformation on geological timescales". In: *Proceedings of NIC Symposium*.

Kay, Suzanne Mahlburg, Beatriz L Coira, Pablo J Caffe, and Chang-Hwa Chen (2010). "Regional chemical diversity, crustal and mantle sources and evolution of central Andean Puna plateau ignimbrites". In: *Journal of Volcanology and Geothermal Research* 198.1-2, pp. 81–111.

Kress, Victor C and Ian SE Carmichael (1991). "The compressibility of silicate liquids containing Fe 2 O 3 and the effect of composition, temperature, oxygen fugacity and pressure on their redox states". In: *Contributions to Mineralogy and Petrology* 108.1-2, pp. 82–92.

Kühn, Christine, Heinrich Brasse, and Gerhard Schwarz (2018). "Three-dimensional electrical resistivity image of the volcanic arc in Northern Chile—an appraisal of early magnetotelluric data". In: *Pure and Applied Geophysics* 175.6, pp. 2153–2165.

Kukarina, Ekaterina, Michael West, Laura Hutchinson Keyson, Ivan Koulakov, Leonid Tsibizov, and Sergey Smirnov (2017). "Focused magmatism beneath Uturuncu volcano, Bolivia: Insights from seismic tomography and deformation modeling". In: *Geosphere* 13.6, pp. 1855–1866. DOI: 10.1130/GES01403.1.

Lallemand, Serge, Arnauld Heuret, and David Boutelier (2005). "On the relationships between slab dip, back-arc stress, upper plate absolute motion, and crustal nature in subduction zones". In: *Geochemistry, Geophysics, Geosystems* 6.9.

Lange, Rebecca A and Ian SE Carmichael (1987). "Densities of Na2O-K2O-CaO-MgO-FeO-Fe2O3-Al2O3-TiO2-SiO2 liquids: new measurements and derived partial molar properties". In: *Geochimica et Cosmochimica Acta* 51.11, pp. 2931–2946.

Laske, Gabi, Guy Masters, Zhitu Ma, and Mike Pasyanos (2013). "Update on CRUST1. 0–A 1-degree global model of Earth's crust". In: *Geophys. Res. Abstr.* Vol. 15. EGU General Assembly Vienna, Austria, p. 2658.

Lau, Nicholas, Ekaterina Tymofyeyeva, and Yuri Fialko (2018). "Variations in the long-term uplift rate due to the Altiplano–Puna magma body observed with Sentinel-1 interferometry". In: *Earth and Planetary Science Letters* 491, pp. 43–47.

Laumonier, Mickael, Fabrice Gaillard, Duncan Muir, Jon Blundy, and Martyn Unsworth (2017). "Giant magmatic water reservoirs at mid-crustal depth inferred from electrical conductivity and the growth of the continental crust". In: *Earth and Planetary Science Letters* 457, pp. 173–180.

Le Pourhiet, Laetitia, Evgenii Burov, and Isabelle Moretti (2003). "Initial crustal thickness geometry controls on the extension in a back arc domain: Case of the Gulf of Corinth". In: *Tectonics* 22.4.

Liao, Jie, Taras Gerya, Marcel Thielmann, A Alexander G Webb, Sofia-Katerina Kufner, and An Yin (2017). "3D geodynamic models for the development of opposing continental subduction zones: The Hindu Kush–Pamir example". In: *Earth and Planetary Science Letters* 480, pp. 133–146.

Maccaferri, Francesco, Maurizio Bonafede, and Eleonora Rivalta (2011). "A quantitative study of the mechanisms governing dike propagation, dike arrest and sill formation". In: *Journal of Volcanology and Geothermal Research* 208.1-2, pp. 39–50.

Mackwell, SJ, ME Zimmerman, and DL Kohlstedt (1998). "High-temperature deformation of dry diabase with application to tectonics on Venus". In: *Journal of Geophysical Research: Solid Earth* 103.B1, pp. 975–984.

Martinod, Joseph, Laurent Husson, Pierrick Roperch, Benjamin Guillaume, and Nicolas Espurt (2010). "Horizontal subduction zones, convergence velocity and the building of the Andes". In: *Earth and Planetary Science Letters* 299.3-4, pp. 299–309.

Mason, Ben G, David M Pyle, and Clive Oppenheimer (2004). "The size and frequency of the largest explosive eruptions on Earth". In: *Bulletin of Volcanology* 66.8, pp. 735–748.

McFarlin, Heather, Douglas Christensen, Stephen R McNutt, Kevin M Ward, Jamie Ryan, George Zandt, and Glenn Thompson (2018). "Receiver function analyses of Uturuncu volcano, Bolivia and vicinity". In: *Geosphere* 14.1, pp. 50–64.

McTigue, DF (1987). "Elastic stress and deformation near a finite spherical magma body: resolution of the point source paradox". In: *Journal of Geophysical Research: Solid Earth* 92.B12, pp. 12931–12940.

Michelfelder, Gary S, Todd C Feeley, and Alicia D Wilder (2014). "The volcanic evolution of Cerro Uturuncu: A high-K, composite volcano in the back-arc of the central Andes of SW Bolivia". In: *International Journal of Geosciences* 5.11, pp. 1263–1281.

Mogi, Kiyoo. (1958). "Relations between the eruptions of various volcanoes and the deformations of the ground surfaces around them". In: *Earthq Res Inst* 36, pp. 99–134.

Moresi, Louis, Frédéric Dufour, and H-B Mühlhaus (2002). "Mantle convection modeling with viscoelastic/brittle lithosphere: Numerical methodology and plate tectonic modeling". In: *Pure and applied Geophysics* 159.10, pp. 2335–2356.

Morgado, Eduardo, Daniel J Morgan, Jason Harvey, Miguel-Ángel Parada, Angelo Castruccio, Raimundo Brahm, Francisco Gutiérrez, Bogomil Georgiev, and Samantha J Hammond (2019). "Localised heating and intensive magmatic conditions prior to the 22–23 April 2015 Calbuco volcano eruption (Southern Chile)". In: *Bulletin of Volcanology* 81.4, pp. 1–21.

Muir, Duncan D, Jon D Blundy, Michael C Hutchinson, and Alison C Rust (2014a). "Petrological imaging of an active pluton beneath Cerro Uturuncu, Bolivia". In: *Contributions to Mineralogy and Petrology* 167.3, p. 980.

Muir, Duncan D, Jon D Blundy, Alison C Rust, and James Hickey (2014b). "Experimental constraints on dacite pre-eruptive magma storage conditions beneath Uturuncu volcano". In: *Journal of Petrology* 55.4, pp. 749–767.

Namur, Olivier, Salvatrice Montalbano, Olivier Bolle, and Jacqueline Vander Auwera (2020). "Petrology of the April 2015 eruption of Calbuco volcano, southern Chile". In: *Journal of Petrology* 61.8, egaa084.

Naranjo, JL, Haraldur Sigurdsson, SN Carey, and W Fritz (1986). "Eruption of the Nevado del Ruiz volcano, Colombia, on 13 November 1985: tephra fall and lahars". In: *Science* 233.4767, pp. 961–963.

Newman, Sally and Jacob B Lowenstern (2002). "VolatileCalc: a silicate melt–H2O–CO2 solution model written in Visual Basic for excel". In: *Computers & Geosciences* 28.5, pp. 597–604.

Nikkhoo, Mehdi, Thomas R Walter, Paul R Lundgren, and Pau Prats-Iraola (2016). "Compound dislocation models (CDMs) for volcano deformation analyses". In: *Geophysical Journal International*, ggw427.

NOAA (2001). *National Geophysical Data Center / World Data Service (NGDC/WDS): NCEI/WDS Global Significant Volcanic Eruptions Database. NOAA National Centers for Environmental Information.* Accessed: 2022-02-03. DOI: 10.7289/V5JW8BSH.

NOAA (2002). *NCEI Volcano Location Database. NOAA National Centers for Environmental Information.* Accessed: 2022-02-03.

Ochs, Frederick A and Rebecca A Lange (1999). "The density of hydrous magmatic liquids". In: *Science* 283.5406, pp. 1314–1317.

Okada, Yoshimitsu (1985). "Surface deformation due to shear and tensile faults in a half-space". In: *Bulletin of the seismological society of America* 75.4, pp. 1135–1154.

Oldenburg, DW and DA Pratt (2007). "Geophysical inversion for mineral exploration: A decade of progress in theory and practice". In: *Proceedings of exploration.* Vol. 7. 5, pp. 61–95.

Oncken, O et al. (2003). "Seismic imaging of a convergent continental margin and plateau in the central Andes (Andean Continental Research Project 1996 (ANCORP'96))". In: *Journal of Geophysical Research: Solid Earth* 108.B7.

Pardini, Federica, Mike Burton, Fabio Arzilli, Giuseppe La Spina, and Margherita Polacci (2018). "SO2 emissions, plume heights and magmatic processes inferred from satellite data: The 2015 Calbuco eruptions". In: *Journal of Volcanology and Geothermal Research* 361, pp. 12–24.

Pearse, J and Y Fialko (2010). "Mechanics of active magmatic intraplating in the Rio Grande Rift near Socorro, New Mexico". In: *Journal of Geophysical Research: Solid Earth* 115.B7.

Pereyra, V (1996). "Modeling, ray tracing, and block nonlinear travel-time inversion in 3D". In: *Pure and Applied Geophysics* 148.3, pp. 345–386.

Perkins, Jonathan P, Kevin M Ward, Shanaka L De Silva, George Zandt, Susan L Beck, and Noah J Finnegan (2016). "Surface uplift in the Central Andes driven by growth of the Altiplano Puna Magma Body". In: *Nature Communications* 7.1, pp. 1–10.

Piccolo, Andrea, Boris J Kaus, Richard W White, Richard M Palin, and Georg S Reuber (2020). "Plume—Lid interactions during the Archean and implications for the generation of early continental terranes". In: *Gondwana Research* 88, pp. 150–168.

Potro, Rodrigo, Mikel Díez, Jon Blundy, Antonio G Camacho, and Joachim Gottsmann (2013). "Diapiric ascent of silicic magma beneath the Bolivian Altiplano". In: *Geophysical Research Letters* 40.10, pp. 2044–2048.

Prezzi, Claudia B, Hans-Jürgen Götze, and Sabine Schmidt (2009). "3D density model of the Central Andes". In: *Physics of the Earth and Planetary Interiors* 177.3-4, pp. 217–234.

Pritchard, Matthew E and Patricia M Gregg (2016). "Geophysical evidence for silicic crustal melt in the continents: where, what kind, and how much?" In: *Elements* 12.2, pp. 121–127.

Pritchard, Matthew E and Mark Simons (2002). "A satellite geodetic survey of large-scale deformation of volcanic centres in the central Andes". In: *Nature* 418.6894, pp. 167–171.

Pritchard, Matthew E and Mark Simons (2004). "An InSAR-based survey of volcanic deformation in the central Andes". In: *Geochemistry, Geophysics, Geosystems* 5.2. DOI: 10.1029/2003GC000610.

Pritchard, Matthew E et al. (2018). "Synthesis: PLUTONS: Investigating the relationship between pluton growth and volcanism in the Central Andes". In: *Geosphere* 14.3, pp. 954–982.

Ranalli, Giorgio (1995). *Rheology of the Earth*. Springer Science & Business Media.

Ratnaswamy, Vishagan, Georg Stadler, and Michael Gurnis (2015). "Adjoint-based estimation of plate coupling in a non-linear mantle flow model: theory and examples". In: *Geophysical Journal International* 202.2, pp. 768–786.

Reuber, Georg S, Boris J P Kaus, Anton A Popov, and T S Baumann (2018). "Unraveling the physics of the Yellowstone magmatic system using geodynamic simulations". In: *Frontiers in Earth Science* 6, p. 117. DOI: 10.3389/feart.2018.00117.

Reuber, Georg S, Anton A Popov, and Boris J P Kaus (2018a). "Deriving scaling laws in geodynamics using adjoint gradients". In: *Tectonophysics* 746, pp. 352–363.

Riel, Nicolas, Boris J P Kaus, Eleanor Green, and Nicolas Berlie (in press). "MAGEMin, a new and efficient Gibbs free energy minimizer: application to igneous systems". In: *Geochemistry, Geophysics, Geosystems*.

Romero, JE et al. (2016). "Eruption dynamics of the 22–23 April 2015 Calbuco Volcano (Southern Chile): Analyses of tephra fall deposits". In: *Journal of Volcanology and Geothermal Research* 317, pp. 15–29.

Rummel, Lisa, Boris JP Kaus, Tobias S Baumann, Richard W White, and Nicolas Riel (2020). "Insights into the compositional evolution of crustal magmatic systems from coupled petrological-geodynamical models". In: *Journal of Petrology* 61.2, egaa029.

Sambridge, Malcolm (1999a). "Geophysical inversion with a neighbourhood algorithm–I. Searching a parameter space". In: *Geophysical Journal International* 138.2, pp. 479–494.

Sambridge, Malcolm (1999b). "Geophysical inversion with a neighbourhood algorithm–II. Appraising the ensemble". In: *Geophysical Journal International* 138.3, pp. 727–746.

Schaaf, Alexander, Miguel de la Varga, Florian Wellmann, and Clare E Bond (2021). "Constraining stochastic 3-D structural geological models with topology information using approximate Bayesian computation in GemPy 2.1". In: *Geoscientific Model Development* 14.6, pp. 3899–3913.

Schilling, Frank R et al. (2006). "Partial melting in the Central Andean crust: a review of geophysical, petrophysical, and petrologic evidence". In: *The Andes*. Springer, pp. 459–474.

Schwarz, Gerhard and Detlef Krüger (1997). "Resistivity cross section through the southern central Andes as inferred from magnetotelluric and geomagnetic deep soundings". In: *Journal of Geophysical Research: Solid Earth* 102.B6, pp. 11957–11978.

Schwarz, Gis, V Haak, E Martinez, and J Bannister (1984). "The electrical conductivity of the Andean crust in northern Chile and southern Bolivia as inferred from magnetotelluric measurements". In: *Journal of Geophysics* 55.1, pp. 169–178.

Sdrolias, Maria and R Dietmar Müller (2006). "Controls on back-arc basin formation". In: *Geochemistry, Geophysics, Geosystems* 7.4.

Segall, Paul (2010). *Earthquake and volcano deformation*. Princeton University Press.

Segall, Paul (2013). "Volcano deformation and eruption forecasting". In: *Geological Society, London, Special Publications* 380.1, pp. 85–106. DOI: https://doi.org/10.1144/SP380.4.

Sevilla, Ruben, Sergio Zlotnik, and Antonio Huerta (2020). "Solution of geometrically parametrised problems within a CAD environment via model order reduction". In: *Computer methods in applied mechanics and engineering* 358, p. 112631.

Sezawa, Katsutada (1931). "The plastico-elastic deformation of a semi-infinite solid body due to an internal force". In: *Bulletin of the Earthquake Research Institute, Tokyo Imperial University* 9.4, pp. 398–406.

Sigmundsson, Freysteinn et al. (2020). "Unexpected large eruptions from buoyant magma bodies within viscoelastic crust". In: *Nature communications* 11.1, pp. 1–11.

Spang, Arne, Tobias S Baumann, and Boris J P Kaus (2021). "A Multiphysics approach to constrain the dynamics of the Altiplano-Puna magmatic system". In: *Journal of Geophysical Research: Solid Earth* 126, e2021JB021725.

Sparks, R Stephen J, Chris B Folkes, Madeleine CS Humphreys, Daniel N Barfod, Jorge Clavero, Mayel C Sunagua, Stephen R McNutt, and Matthew E Pritchard (2008). "Uturuncu volcano, Bolivia: Volcanic unrest due to mid-crustal magma intrusion". In: *American Journal of Science* 308.6, pp. 727–769.

Spilliaert, N, P Allard, N Métrich, and AV Sobolev (2006). "Melt inclusion record of the conditions of ascent, degassing, and extrusion of volatile-rich alkali basalt during the powerful 2002 flank eruption of Mount Etna (Italy)". In: *Journal of Geophysical Research: Solid Earth* 111.B4.

Stadler, Georg, Michael Gurnis, Carsten Burstedde, Lucas C Wilcox, Laura Alisic, and Omar Ghattas (2010). "The dynamics of plate tectonics and mantle flow: From local to global scales". In: *science* 329.5995, pp. 1033–1038.

Syracuse, Ellen M and Geoffrey A Abers (2006). "Global compilation of variations in slab depth beneath arc volcanoes and implications". In: *Geochemistry, Geophysics, Geosystems* 7.5.

Talwani, Manik, J Lamar Worzel, and Mark Landisman (1959). "Rapid gravity computations for two-dimensional bodies with application to the Mendocino submarine fracture zone". In: *Journal of geophysical research* 64.1, pp. 49–59.

Tassara, Andrés and Andrés Echaurren (2012). "Anatomy of the Andean subduction zone: three-dimensional density model upgraded and compared against global-scale models". In: *Geophysical Journal International* 189.1, pp. 161–168.

Tassara, Andres, Hans-Jürgen Götze, Sabine Schmidt, and Ron Hackney (2006). "Three-dimensional density model of the Nazca plate and the Andean continental margin". In: *Journal of Geophysical Research: Solid Earth* 111.B9. DOI: 10.1029/2005JB003976.

Taylor, Nicola C, Jessica H Johnson, and Richard A Herd (2021). "Making the most of the Mogi model: Size matters". In: *Journal of Volcanology and Geothermal Research* 419, p. 107380.

Tetreault, J áL and SJH Buiter (2012). "Geodynamic models of terrane accretion: Testing the fate of island arcs, oceanic plateaus, and continental fragments in subduction zones". In: *Journal of Geophysical Research: Solid Earth* 117.B8.

Turcotte, Donald L and Gerald Schubert (2002). *Geodynamics*. Cambridge university press.

Varga, Miguel De La, Alexander Schaaf, and Florian Wellmann (2019). "GemPy 1.0: open-source stochastic geological modeling and inversion". In: *Geoscientific Model Development* 12.1, pp. 1–32.

Vigneresse, J A and J D Clemens (2000). "Granitic magma ascent and emplacement: neither diapirism nor neutral buoyancy". In: *Geological Society, London, Special Publications* 174.1, pp. 1–19.

Wallace, Paul J and Terrence M Gerlach (1994). "Magmatic vapor source for sulfur dioxide released during volcanic eruptions: evidence from Mount Pinatubo". In: *Science* 265.5171, pp. 497–499.

Walter, Thomas R and Mahdi Motagh (2014). "Deflation and inflation of a large magma body beneath Uturuncu volcano, Bolivia? Insights from InSAR data, surface lineaments and stress modelling". In: *Geophysical Journal International* 198.1, pp. 462–473.

Ward, Kevin M, George Zandt, Susan L Beck, Douglas H Christensen, and Heather McFarlin (2014). "Seismic imaging of the magmatic underpinnings beneath the Altiplano-Puna volcanic complex from the joint inversion of surface wave dispersion and receiver functions". In: *Earth and Planetary Science Letters* 404, pp. 43–53.

Ward, Kevin M, Jonathan R Delph, George Zandt, Susan L Beck, and Mihai N Ducea (2017). "Magmatic evolution of a Cordilleran flare-up and its role in the creation of silicic crust". In: *Scientific reports* 7.1, pp. 1–8. DOI: 10.1038/s41598-017-09015-5.

Wellmann, Florian and Guillaume Caumon (2018). "3-D Structural geological models: Concepts, methods, and uncertainties". In: *Advances in Geophysics*. Vol. 59. Elsevier, pp. 1–121.

Wessel, Paul, Walter HF Smith, Remko Scharroo, Joaquim Luis, and Florian Wobbe (2013). "Generic mapping tools: improved version released". In: *Eos, Transactions American Geophysical Union* 94.45, pp. 409–410.

Wigger, Peter J (1988). "Seismicity and crustal structure of the Central Andes". In: *The southern central Andes*. Springer, Berlin, Heidelberg, pp. 209–229.

Wijns, Chris, Fabio Boschetti, and Louis Moresi (2003). "Inverse modelling in geology by interactive evolutionary computation". In: *Journal of Structural Geology* 25.10, pp. 1615–1621.

Williams, Charles A and Geoff Wadge (2000). "An accurate and efficient method for including the effects of topography in three-dimensional elastic models of ground deformation with applications to radar interferometry". In: *Journal of Geophysical Research: Solid Earth* 105.B4, pp. 8103–8120.

Wörner, Gerhard, Mirian Mamani, and Magdalena Blum-Oeste (2018). "Magmatism in the Central Andes". In: *Elements: An International Magazine of Mineralogy, Geochemistry, and Petrology* 14.4, pp. 237–244.

Yamakawa, Norio (1955). "On the strain produced in a semi-infinite elastic solid by an interior source of stress". In: *J. Seismol. Soc. Japan, Ser. 2* 8.2, pp. 84–98.

Yang, Xue Min, Paul M Davis, and James H Dieterich (1988). "Deformation from inflation of a dipping finite prolate spheroid in an elastic half-space as a model for volcanic stressing". In: *Journal of Geophysical Research: Solid Earth* 93.B5, pp. 4249–4257.

Yuan, Xichun et al. (2000). "Subduction and collision processes in the Central Andes constrained by converted seismic phases". In: *Nature* 408.6815, pp. 958–961.

Zandt, George, Mark Leidig, Josef Chmielowski, David Baumont, and Xiaohui Yuan (2003). "Seismic detection and characterization of the Altiplano-Puna magma body, central Andes". In: *Pure and Applied Geophysics* 160.3-4, pp. 789–807.

Zelst, Iris van, Fabio Crameri, Adina E Pusok, Anne Glerum, Juliane Dannberg, and Cedric Thieulot (2021). "101 Geodynamic modelling: How to design, carry out, and interpret numerical studies". In: *Solid Earth Discussions*, pp. 1–80.

Zong, Jingjing, Robert R Stewart, Nikolay Dyaur, and Michael T Myers (2017). "Elastic properties of rock salt: Laboratory measurements and Gulf of Mexico well-log analysis". In: *Geophysics* 82.5, pp. D303–D317.